A MEASUREMENT OF THE PROCESS P+D → He^3 + PHOTON AT INTERMEDIATE ENERGIES

Thesis by

Robert V. Kline

In Partial Fulfillment of the Requirements

For the Degree of

Doctor of Philosophy

California Institute of Technology

Pasadena, California

1973

(Submitted October 10, 1973)

ACKNOWLEDGEMENTS

A large experiment necessarily draws upon the talents and resources of many people, and often does so for an extended period of time. The help, cooperation, and material support received during the course of this experiment are gratefully acknowledged. Special thanks are extended to the following people for their contributions to this project.

First of all, my thanks to my advisor, Clemens A. Heusch. In addition to conceiving the experiment, he was active in all phases of its execution, and in general insured that the project was a valuable and rewarding experience.

My thanks to Kirk McDonald for many contributions to all aspects of the experiment, and for an active interest in its progress.

Construction and testing of one of the photon detectors owes much to the help and suggestions of Charles Prescott and Steve Yellin, and to the ingenuity and skill of Walter Nilsson.

My thanks to Abe Seiden for encouragement, and for many valuable discussions.

To Jim Carroll, Don Fredrickson, Mike Goitein, Burns MacDonald, and Al Stetz go my thanks for a great deal of effort in bringing the experiment through the data collecting phase, and for many helpful suggestions during the subsequent analysis of the data.

To Barry Lieberman and Karl Stein for many hours donated to the task of collecting data.

I am grateful to Victor Perez-Mendez for making available the resources of the Lawrence Berkeley Laboratory, and for a continued interest in the progress of the experiment. Also to James Vale and the crew of the 184-inch cyclotron for keeping the machine running smoothly throughout the several months of data taking.

My thanks to Robert Walker and to Caltech for providing continued financial support during the long course of this project.

Finally, I would like to thank Jeanne Elliott, Patti Fox, and Judi Laurence for contributing generously of their time and skill toward the production of this document.

ABSTRACT

We have measured the process $pd \rightarrow He^3\gamma$ in the energy region of $\Delta(1236)$ nucleon isobar excitation. At an incident proton energy of 462 MeV, data were assembled for center of mass angles of 45^o, 60^o, 75^o, 90^o, 105^o, 120^o, and 135^o. We also measured the energy dependence of the 90^o cross-section in the center of mass, for incident proton energies of 377, 462 and 576 MeV. We discuss implications for T-invariance in the electromagnetic interaction by a detailed balance comparison with the inverse reaction. In addition, we present an angular distribution for the process $pd \rightarrow He^3\pi^o$ at an incident proton energy of 462, as well as limited angular distributions at 377 and 576 MeV.

TABLE OF CONTENTS

PART	TITLE	PAGE
I.	INTRODUCTION	1
II.	EXPERIMENTAL METHOD	11
III.	DATA TAKING	21
	1. Hourly Checks	23
	2. 4-Hourly and 8-Hourly Checks	25
	3. Preliminary Analysis	27
	4. Calibrations	29
	5. Information Collected	33
IV.	DATA ANALYSIS	35
	1. Constants	36
	2. Data Summary Program	36
	A. Spark Chamber Efficiencies - Helium	38
	B. Spark Chamber Efficiencies - Photon	39
	3. Geometry-Kinematics	39
	4. Cuts	44
	5. Efficiencies	51
	A. Geometric Solid Angle Acceptance	52
	B. Electronic Efficiencies	55
	6. Cross Section Calculation	56
	7. Background Subtraction	57
	8. Systematic Errors	58

PART	TITLE	PAGE
V.	RESULTS	63
VI.	DISCUSSION	72
VII.	APPENDICES	
	A. The Beam	78
	B. Target Monitor	91
	C. Beam Energy and Stability	98
	D. Photon Counters	104
	E. Vertex Location - Photon Chambers	117
	F. Helium Detector	128
	G. Helium Chamber Local Coordinates	146
	H. Geokin	150
	I. Data Summary Program Structure	154
	J. Efficiency Program	157
	K. Chi-Square Fitting	159
	L. Pi-Zero Analysis	168
	M. Targets	178
	N. Beam Integrators	181
	O. Current Experimental Status of Symmetries	183
VIII.	REFERENCES	185

LIST OF FIGURES

FIGURE	TITLE	PAGE
2.1	Experimental Setup	13
2.2	Helium Lab Angle Versus Helium Center-of-Mass Angle	16
2.3	Simplified Schematic of the Electronics	19
3.1	Hourly Check	22
3.2	4-Hourly Check	26
3.3	8-Hourly Check	28
3.4	Run Sheet	31
4.1	Definition of θ and ϕ Angles	41
4.2	Reconstructed Event Origins	47
4.3	Differential Pulse Height Counter Spectrum	49
4.4	Time-of-Flight ADC Versus Helium Detector ADC	48
4.5	Typical Solid Angle Acceptance	59
4.6	Typical Chi-Square Distribution	59
5.1	Angular Distribution for pd $\rightarrow He^3\gamma$ at 462 MeV.	65
5.2	Energy Dependence of the 90-Degree cm Data	66
5.3	Angular Distribution for pd $\rightarrow He^3\pi^\circ$ at 462 MeV.	69
5.4	Energy Dependence of the Pi-Zero Data	70
6.1	Structure of the Proton Beam	80
6.2	Ray Trace for on Momentum Protons - Horizontal View	84

FIGURE	TITLE	PAGE
6.3	Ray Trace for on Momentum Protons - Vertical View	85
6.4	Ray Trace for off Momentum Protons - Horizontal View	86
6.5	Kinematic Position of the Target Monitor Telescopes	92
6.6	Schematic View of the Target Monitor Telescopes	93
6.7	Target Monitor Logic Electronics	96
6.8	Typical Bragg Peak Obtained from a Range Measure	99
6.9	Numerical Integration Results	101
6.10	Range Measuring Apparatus	102
6.11	Relative Ionization Versus Range with Mean Range Noted	103
6.12	Basic Components of the Photon Detector	105
6.13A	Liquid Light Pipe	107
6.13B	Details of Photon Counter Construction	107
6.14	Tagged Photon Beam Experimental Setup	108
6.15	Photon Detector Logic Electronics	109
6.16	Pulse Height Versus Energy	111
6.17	Energy Resolution Versus Photon Energy	113
6.18	Individual Component Pulseheight Spectra	114
6.19	Conversion Efficiency Versus Energy for a $2X^{\circ}$ Lead Glass Converter	116

FIGURE	TITLE	PAGE
6.20	Typical Electron Pair Shower	118
6.21	Relative Positions of Lead Glass Converter and Wire Spark Chambers	119
6.22	Resolution for a Single Track	122
6.23	Assignment of a Vertex Error - Pairs of Tracks	124
6.24	Assignment of a Vertex Error When Both Tracks Have the Same Slope	125
6.25	Assignment of a Vertex Error - Three Tracks	127
6.26	Exploded View of the Helium Detector	130
6.27	Helium Detector Construction Details	131
6.28	Helium Detector Logic Electronics	133
6.29	Americium-241 Energy Spectrum	134
6.30	Typical He^3 Spectrum - 114.6 MeV Heliums	142
6.31	Typical He^3 Spectrum - 114.6 MeV Heliums - Log Plot	143
6.32	Response of He^3 Detector to p, d, He^3, He^4 Versus Energy	154
6.33	Definition of Wire Spark Chamber Coordinates	147
6.34	Construction of the Angles	151
6.35	Logical Structure of the Program Geokin	152
6.36	Logical Structure of the Data Summary Program	155
6.37	Logical Structure of the Efficiency Program	158
6.38	Definition of the Angles θ and ϕ	160

FIGURE	TITLE	PAGE
6.39	Differential Pulse Height Counter Spectrum	171
6.40	Reconstructed Event Origins	172
6.41	Differential Cross Section for pd → $He^3\pi^\circ$ at 462 MeV	174
6.42	Differential Cross Section for pd → $He^3\pi^\circ$ at 377 and 571 MeV	175
6.43	Target Construction Details	179

LIST OF TABLES

TABLE	TITLE	PAGE
3.1	Alpha-63 Output	30
3.2	Kinds of Data Collected	32
3.3	Kinematic Settings for Which Data Were Collected	33
4.1	Background Subtraction Ratios	61
5.1	Angular Distribution for $pd \rightarrow He^3\gamma$ at 462 MeV	64
5.2	He^3 Photodisintegration Data	68
5.3	Angular Distribution for $pd \rightarrow He^3\pi^o$	71
5.4	Comparison of 462 MeV Data	76
5.5	Comparison of 90^o CM Points	77
6.1	Amount of Degrader Used in the Proton Beam	79
6.2	Elements of the Proton Beam - Horizontal	82
6.3	Elements of the Proton Beam - Vertical	83
6.4	Beam Energy and Beam Width	89
6.5	Degrader Thickness - gm/cm^2	95
6.6	Angular Distribution for $pd \rightarrow He^3\pi^o$	176

To My Parents

INTRODUCTION

We report on a measurement of the process

$$pd \rightarrow He^3\gamma \quad . \tag{1}$$

At an incident proton energy of 462 meV, we have measured process (1) for seven center-of-mass angles: 45^o, 60^o, 75^o, 90^o, 105^o, 120^o, and 135^o. We also assembled data at a center-of-mass angle of 90^o for incident proton energies of 377 MeV and 576 MeV. The angles were chosen to overlap as much as possible with existing He^3 photodisintegration data. The energy region was selected so as to be able to probe the effect of the excitation of a $\Delta(1236)$ nucleon isobar.

We also report on a measurement of the process

$$pd \rightarrow He^3\pi^o. \tag{2}$$

Data were collected over a center-of-mass angle region from 45^o to 135^o, at an incident proton energy of 462 MeV. Limited angular distributions were obtained in the region of 90^o center-of-mass angle for incident proton energies of 377 MeV and 576 MeV. The interest here again was to see whether nucleon isobar excitation is important in this process.

We were motivated to measure process (1) by the observations of earlier investigations showing that nucleon isobar excitation plays an important part in the reaction

$$\gamma d \rightarrow np. \tag{3}$$

A prominent enhancement, attributed to the $\Delta(1236)$ isobar, appears in the energy dependent cross section of reaction (3) in the energy region of k_γ = 290 MeV. Are such excitations important in other light nuclei? We set out to study this question in He^3.

A second motivation for measuring process (1) was the suggestion of several investigators that the $\gamma N\Delta$ vertex, important in process (3), might be used in experiments investigating T-invariance in the electromagnetic interaction of hadrons. Berstein , et al.[26], after reviewing the experimental evidence, had concluded that existing data were consistent with rather large violations of C and T. Subsequently, Barshay[45] and Christ and Lee[27] selected a set of experiments involving the $\gamma N\Delta$ vertex to test this conclusion.

Our interest in time-reversal invariance (TRI) in the electromagnetic interaction of hadrons has its origin in the now well confirmed CP violation, observed in the weak decay of K_L^o into two pions. This decay mode occurs about .2% of the time, a possibly meaningful fractional strength of about α/π. This, in turn, led to the suggestion, mentioned above, that the observed CP violation may be the result of an electromagnetic correction to the weak Hamiltonian. Since existing experimental evidence did not preclude a rather large violation in the electromagnetic interactions of hadrons, it was clear that this might be a fruitful area in which to search.

Two techniques exist for investigating T-invariance in the electromagnetic interaction of hadrons: 1) measurements of expectation values of T-odd operators; 2) detailed balance measurements. The results reported in this thesis employ the second technique. A third technique has been used for systems with zero additive quantum numbers: assuming (with good reason) that P is a good symmetry of the electromagnetic interaction, the decay of C-eigenstates (π^o, η^o,...) must conserve C if T is good.

We review here briefly some results obtained in earlier measurements, including, for completeness, some made employing weak and strong interactions. An excellent review of the experimental status of time-reversal invariance through 1969 has been made by Henley[21].

The principle of detailed balance is embodied in the following reciprocity relation, which, with $\Delta = 0$, is valid in the center-of-mass system if the process $ab \leftrightarrow cd$ is invariant under time reversal:

$$1 + \Delta = (2S_a + 1)(2S_b + 1) P_a^2 d\sigma/d\Omega|_{ab} / (2S_d + 1) P_c^2 d\sigma/d\Omega|_{cd}.$$

P_a and P_c are momenta, S_a, S_b, S_c, and S_d are spins, and $d\sigma/d\Omega$ is the differential cross section. Δ is a T violation parameter. This relationship assumes an unpolarized beam and target; one must be careful to insure that these conditions are met when performing experiments in order to avoid confusing effects. If possible, measurements are made near 0^o or 180^o in order to minimize contributing spin channels.

McDonald[5] has made a survey of possible reciprocity tests for the electromagnetic interaction of hadrons of the form $\gamma A \leftrightarrow BC$, where excited states for A, B, and C can be excluded from consideration. Possible targets include p, n, d, He^3, H^3, He^4, and Li^6. The possibilities for B and C include all of those for A, plus charged pions. Selection of a pair of reactions for use in a detailed balance test of time-reversal invariance from these possibilities involves such experimental considerations as the number of neutral particles involved, kinetic energies and angles of final states, radioactivity of targets or beams (e.g. H^3), any existing data suggesting nucleon isobar excitation, among others.

no violation, with error bars as small as 1.5% (Ref. 66).

Lower energy measurements look for interferences between competing multipoles to measure the relative phase. Usually only M1 and E2 multipoles are involved. Some of the most accurate measurements have been made using the Mössbauer effect. Using a polarized target, and linearly polarized photons, one looks for a term of the form $(\vec{k}\cdot\vec{j} \times \vec{\varepsilon})\ (\vec{k}\cdot\vec{j})(\vec{\varepsilon}\cdot\vec{j})$, where $\vec{k}$ is the photon vector, $\vec{\varepsilon}$ is its polarization vector, and $\vec{j}$ is the polarization of the absorber. This term is proportional to $Y_3^2\ (\phi,\theta)$ sin ϕ. The most accurate result, using a M1 - E2 transition in Ru^{99}, gives sin $\phi = (1.0 +/- 1.7) \times 10^{-3}$ (Ref. 67).

Measurements involving two photon final states have placed limits of comparable magnitude on the relative phase between M1 and E2 multipoles. One recent measurement using the capture of polarized neutrons on ^{36}Cl looks for a correlation of the form $(\vec{k}_1\cdot\vec{k}_2 \times \vec{j})(\vec{k}_1\cdot\vec{k}_2)$, where $\vec{k}_1$ and $\vec{k}_2$ are photon momenta, $\vec{j}$ is the polarization vector of the nucleus. Bulgakov[68] reports a value for ϕ of $(-1.8 \pm 2.2) \times 10^{-3}$.

A weak interaction measurement has been made using the reaction $\Lambda^o \rightarrow \pi^+ p$. A violation would be indicated by a term of the form $<\sigma_p>\cdot<\sigma_\Lambda>\times \vec{k}_p$. The resulting time reversal phase is given as $\phi = 18^o +/- 1.6^o$ (Ref. 70).

A strong interaction measurement using pp elastic scattering looks for a term of the form $(\vec{\sigma}_1\cdot q\ \vec{\sigma}_2\cdot\vec{K} + \vec{\sigma}_1\cdot\vec{K}\ \vec{\sigma}_2\cdot\vec{q})\ F(\vec{k}_i,\vec{k}_f)$ with $\vec{q} = \vec{k}_i - \vec{k}_f$, $\vec{K} = \vec{k}_i \times \vec{k}_f$ places sin $\phi = .06 +/- .09$ (Ref. 71).

Finally, we consider measurements of static electric moments, especially the static electric dipole moment of the neutron. Here one looks for an

time-reversal invariance. Upon redoing one of these experiments on (reaction 4), and improving the statistical accuracy of the other, the evidence disappeared. The most recent results measure a phase of $4^{o} \pm 10^{o}$. The need to use a neutron beam in reaction (4), as well as the presence of two neutral particles in both reactions (3) and (4), make these experiments very difficult to perform. The statistical accuracy is about 7%.

A similar reciprocity test has been performed on the reactions $\pi^{-}p \leftrightarrow n\gamma$. Again one faces formidable experimental difficulties, owing to a completely neutral final state in one direction, and the necessity of using a deuterium target in the other. Early measurements again claimed a departure from time-reversal invariance,[53] although more recent measurements are compatible with no effect.[54]

Some of the most accurate measurements, especially at low energies, have come from experiments testing the strong interaction. The most accurate experiment to date, employing the reaction $Mg^{24}d \leftrightarrow Mg^{25}p$, gives $1 + \Delta = 0.999 \pm .003$ (Ref. 65), implying that time-reversal is good to at least the .3% level in this strong interaction reaction.

As the second basic method to search for T-violation effects, we mention the investigation of correlations among measureable quantities, which would indicate the presence of T-odd amplitudes. Time-reversal invariance requires the relative phase of contributing amplitudes to be either 0^{o} or 180^{o}. The results of these experiments are usually expressed as a phase, ϕ, where a phase of 90^{o} represents maximal interference between

(H^3), any existing data suggesting nucleon isobar excitation, etc.

Barshay suggested that one measure reaction (3), and the reaction

$$np \rightarrow d\gamma \tag{4}$$

arguing that since the $\Delta(1236)$ isobar is such a dominant feature of these processes, perhaps they might exhibit a large T-violation. He first assumes that one can associate a phase with $\gamma N\Delta$ vertex, and suggests that the following diagram dominates the resonant amplitude:

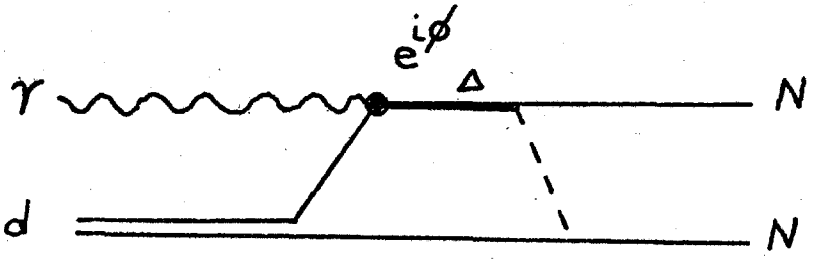

Using a partial wave analysis in which only S,P and D wave transitions are considered, Barshay argues that the resonant amplitude for the transition $M(1) \rightarrow {}^1D_2$ contributes about 36% to the cross section. The most likely background amplitudes are taken to correspond to $E(1) \rightarrow {}^3P_0$ and $M(1) \rightarrow {}^1S_0$ transitions which Barshay estimates contribute about 60% and 4%, respectively, to the cross section.

Parameterizing the resulting angular distribution as $A_0 + A_2 \cos^2\theta$, the phase ϕ is represented by

$$3 \sin \phi = \left(\frac{A_2}{A_0}\right| \text{ forward} - \left.\frac{A_2}{A_0}\right| \text{ backward)}$$

For maximal T-violation, $\phi = 90^\circ$, and one might expect a violation on the order of 30%.

measurement[68] of the capture of polarized neutrons on Cl^{36}, followed by double photon emission, looks for a correlation of the form $(\vec{k}_1 \cdot \vec{k}_2 \times \vec{j})(\vec{k}_1 \cdot \vec{k}_2)$, where $\vec{k}_1$ and $\vec{k}_2$ are photon momentum vectors, and $\vec{j}$ is the polarization vector of the nucleus. P. A. Bulgakov[68] reports a value of $(1.8 \pm 2.2) \times 10^{-3}$ for the relative phase, again consistent with no interference of competing multipoles.

A weak interaction measurement has been made[69] using the reaction $\Lambda^o \rightarrow \pi^- p$. A violation would be indicated by the presence of a term proportional to $\vec{\sigma}_p \cdot \vec{\sigma}_\Lambda \times \vec{k}_p$, where $\vec{\sigma}_p$ and $\vec{\sigma}_\Lambda$ are the polarization of the final state proton, and the initial Λ^o, respectively, and $\vec{k}_p$ is the momentum vector of the final state proton. The resulting phase is given as $2.6^o \pm 4.2^o$, again consistent with 0^o or 180^o relative phase of the dominant competing S and P partial wave amplitudes.

In 1969, when poorly confirmed indications of T-violation effects in the electromagnetic interaction abounded, our group decided to perform a measurement of a pair of reactions as a test of time-reversal invariance. Rather than repeat measurements of reactions already measured or in progress, we decided to measure reaction (1), and its inverse reaction

$$\gamma He^3 \rightarrow pd. \qquad (5)$$

Reaction (5) was measured in the last experiment performed on the now defunct Cal Tech 1.5 GeV electron synchrotron. The results of the measurement has already been reported[5,56] elsewhere.

Although reactions (1) and (5) have cross sections typically one order of magnitude lower than those for $np \leftrightarrow \gamma d$, they have the advantage of

an additional charged particle. This allows for better constraint on the kinematical definition of the initial and final states.

One difficulty with reaction (1) is the presence of a large background $pd \to He^3\pi^o$ ($\pi^o \to \bar{\gamma}\bar{\gamma}$), which is on the order of 20-30 times larger than reaction (1). A corresponding background was the most serious contamination for the reaction $np \to \gamma d$.

Another difficulty was due to the low helium kinetic energy encountered for backward helium center-of-mas angles. The double charge makes energy loss and multiple scattering potentially serious. On the other hand, the double charge enhances the definition of this particle in any Coulomb interaction.

Another problem could result from processes such as $pd \to He^{3*}\gamma$, since our experiment would not resolve excited states of the 3 nucleon system. Although there is no consensus on this point, it is generally believed that no excited states of He^3 exist, either bound or virtual.[57]

Results on reaction (5)[5,56] do not indicate the presence of a bump in the total cross section due to the contribution of a $\Delta(1236)$, as is so prominent in the reaction $np \leftrightarrow \gamma d$. One possible explanation for this is that the contribution of a resonant amplitude is small. But why? Consider isospin: indicated below is a possible diagram for a resonant amplitude.

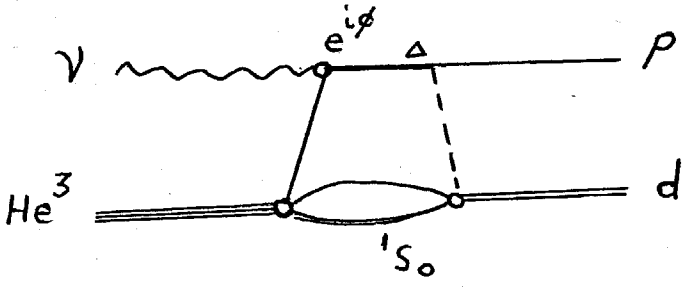

Isospin keeps the lower intermediate nucleons from forming a deuteron. Partial wave analysis[61] suggests that the most likely state is $^1S_0$. The two nucleons can possess relative kinetic energy which serves, in part, to obscure the observation of Δ production by smearing out the kinematics.

In the photodisintegration of the deuteron, we note that the deuteron is a very loosely bound system. The breakup process is described very well by considering one nucleon to be a spectator. The photon then interacts with a nucleon on the mass shell. The resultant energy dependent cross section can easily show a dominant influence from Δ production; the width of the resonant behavior is due largely to the natural width of the Δ excitation.

No analogy to the deuteron breakup process can be made for He^3 photodisintegration, since isospin forbids the breakup of He^3 into an exchanged nucleon and a spectator deuteron. Instead, the vertex of helium breakup contains a $^1S_0$ intermediate dinucleon state and a virtual nucleon. It is the interaction of this virtual nucleon with the incident photon combined with the relative kinetic energy of the two nucleons in the $^1S_0$ intermediate state that serve to obscure any influence of Δ production in the process $\gamma He^3 \rightarrow pd$.

The absence of a dramatic s channel effect obviously does not affect the value of reactions (1) and (5) as a test of time-reversal invariance. It does, however, serve to indicate the complications for interpretation of the results in terms of individual resonant and non-resonant ampli-

particularly promising probe of time reversal invariance independent because it can provide a wholly new set of amplitudes for interference effects; it may exhibit features unobservable in the published work of other reactions.

The measurement of process (1) was performed at the Lawrence Berkeley Laboratory* 184" synchrocyclotron. The data will be compared with a measurement of the photodisintegration of He^3 already completed and reported elsewhere.[5,56]

*Formerly the Lawrence Radiation Laboratory.

Experimental Method

Two major points entered into the decision as to what kind of apparatus to use for the detection of the reaction $pd \rightarrow He^3\pi^0$. First, $pd \rightarrow He^3\pi^0$ will contribute a very large background, on the order of 30 times larger than the reaction of primary interest. Second, the absolute cross section for the process $pd \rightarrow He^3\gamma$ is a very small one, on the order of 10^{-32} cm^2.

The apparatus was chosen so as to optimize geometric detection efficiency in order to offset the small cross section. Good resolution of all particle trajectories was the essential feature that helped towards efficient background subtraction.

References are made to the more detailed discussions of the apparatus found in the appendices. The basic features of the experimental setup are as follows:

- A proton spectrometer providing about 10^8 protons/sec with .5% momentum resolution, and a set of ion chambers and integrators for beam monitoring.
- Liquid deuterium targets with two flasks of different thickness and a target monitoring system.
- A thick plastic total absorption scintillation detector for energy determination of the He^3's, and a set of wire spark chambers for trajectory delineation.
- Two total absorption lead glass photon hodoscopes/spectrometers, and associated wire spark chambers for determining photon vertices.

- A special purpose computer for recording information on magnetic tape.[20]

An overall view of the apparatus can be seen in Fig. 2.1.

The experiment was performed using the LBL 184-inch synchrocyclotron, which operates at a fixed energy of 735 ± 20 MeV[1]. Based on some Monte Carlo studies made to determine the quality of the proton beam needed to enable us to effectively separate the forward and background reactions, the following requirements resulted:

- A momentum bite of < 1% for energies between 300 and 600 MeV;
- An angular divergence of < .5 degrees, at the same energies.

In order to obtain useful counting rates we needed a flux of no less than 10^8 protons/sec at the liquid deuterium target. The resulting beam design is shown schematically in Fig. 6.1.

The main features of the beam are as follows. First the 735 MeV cyclotron beam passes through a copper degrade in order to produce a beam with the desired mean energy. The position where the beam exits from the copper serves as the beam source. The angular acceptance of the beam is determined by slit 1. The momentum acceptance is determined by slit 3. Finally a quadrapole double t images slit 3 on the target with a magnification of about 1.8. Steering of the beam is done with the final bending magnet, Atlas. Details of the beam design, and the acceleration of particles other than protons, can be found in Appendix A.

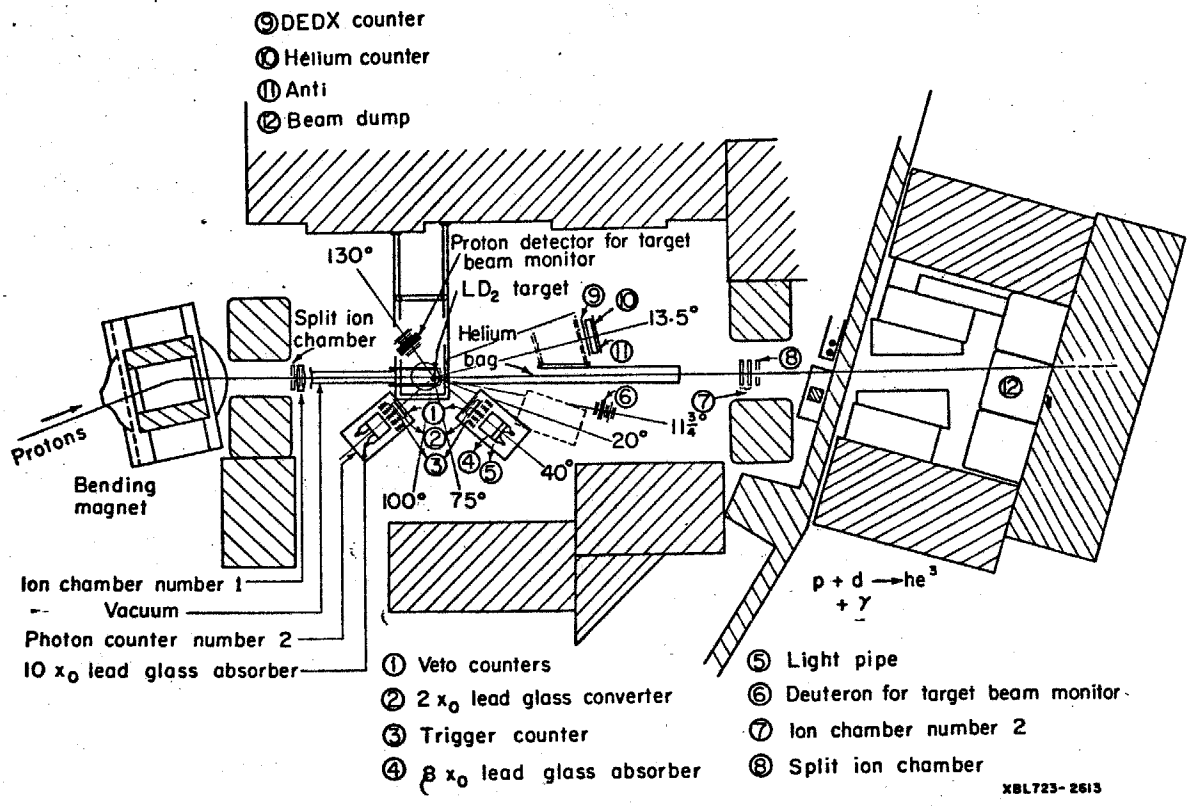

Figure 2.1 experimental Setup

The beam intensity was measured with a set of ion chambers and current integrators. Three integrator systems were employed to provide for relative consistency checks. The current integrators were kept inside of a box constructed of styrofoam in order to thermally insulate them. The local barometric pressure was recorded; from this, corrections to the integrator thickness were made.

In order to minimize the effects of multiple scattering of the He^3, our liquid deuterium targets were as thin as permissible by data rate requirements. For those settings in which the kinetic energy of the He^3 was greater than 100 MeV, a half-inch target was used, for $T(He^3) < 100$ MeV, a sixth-inch target. Use of the thinner target was somewhat compensated for by the higher cross-section for those settings in which the He^3 energy was low. The target, was about four inches high and wide (for construction details, see Appendix M.)

The liquid was obtained by condensing gaseous deuterium. Liquid hydrogen was circulated around the target flask, and served as the cooling agent for the liquid deuterium. The liquid hydrogen container was in turn surrounded with liquid nitrogen.

Bubbling in such thin targets was a potential problem. In order to monitor the condition of the target, a set of range telescopes were placed so as to measure the proton-deuteron elastic scattering rate. The telescopes were placed at a setting kinematically unavailable to proton-proton elastic scattering. Careful adjustment of the ranging material made random triggers negligible, as measured by the full-to-empty ratio of the monitors (cf. Appendix N).

We now turn to the detection apparatus for the final state particles. A total absorption plastic scintillation detector, with an energy resolution of about 3% HWHM, was used to detect the He^3 particles. Since the velocity of the helium particle is less than that of the velocity of the center of mass, the lab angle has a maximum (see figure 2.2). The helium detector was made large enough to intercept the lab He^3's from all center of mass angles of interest. Data were in fact collected from two center of mass angles simultaneously defined by two photon detectors. This helped compensate for the low cross section for $pd \rightarrow He^3\gamma$.

The detector was just thick enough (4 inches) to absorb the highest energy He^3's encountered in this experiment (430 MeV). This thickness provided a unique pulse height for maximum He^3 energy. For lesser pulse heights, there is less uniqueness of interpretation, as discussed in Appendix F. Additional discrimination was achieved against non-stopping particles by placing a veto counter behind the detector. See Appendix F for construction details.

Since the range counter could be "fooled" by protons or deuterons, we built an additional safeguard into the system: a 1/8-inch scintillation counter covered the entire face of the range counter. We demanded that a He^3 candidate deposit considerably more energy in this counter than a fast proton or other singly charged particle. A clean separation was possible notwithstanding the larger counter size.

Helium-3 trajectories were determined with two sets of wire spark chambers. Multiple scattering effects, as well as ionization losses,

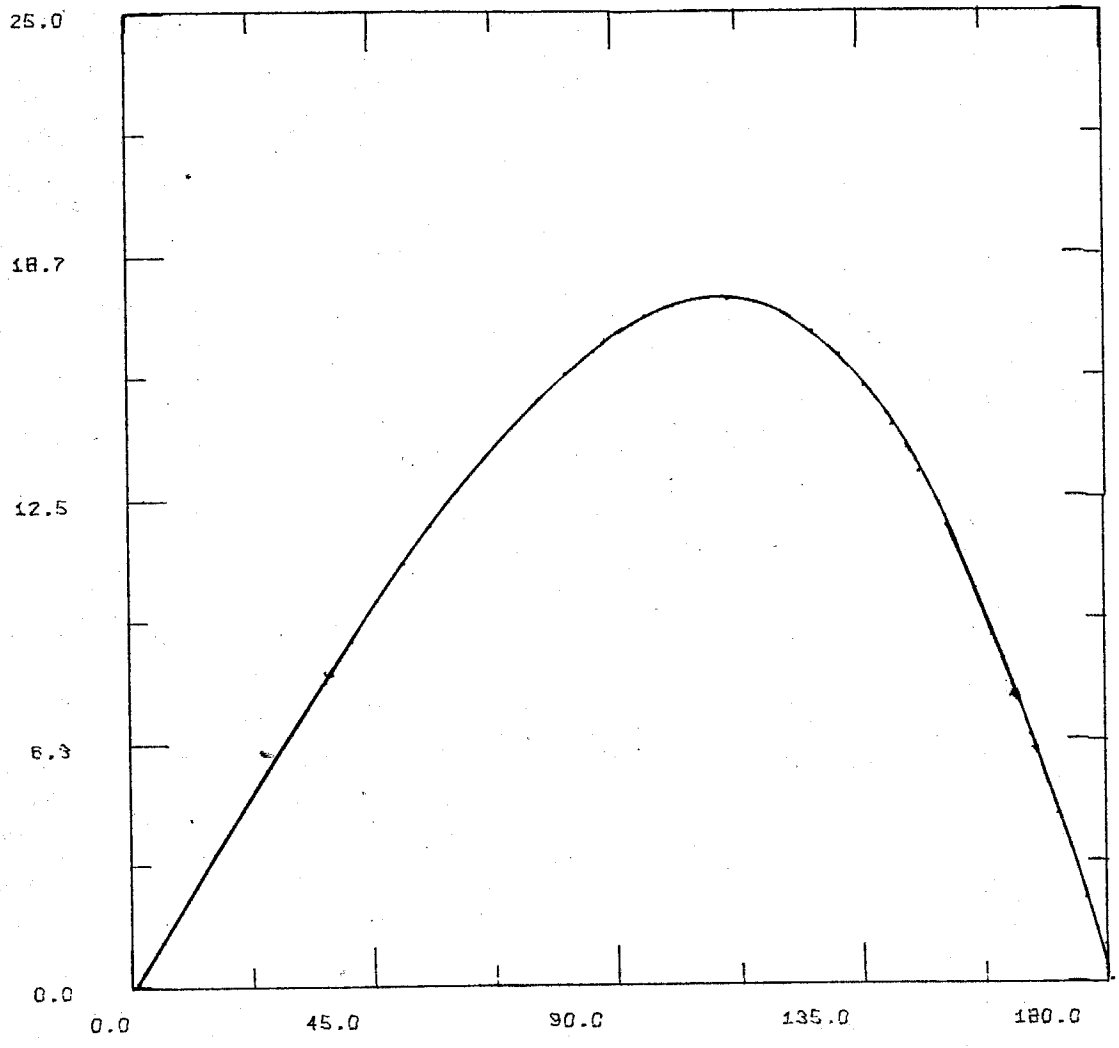

Figure 2. 2 Helium Lab Angle Versus Helium Center-of-mass Angle

were minimized by placing helium filled bags between the target and the wire chambers, and between the two sets of wire chambers. The same bags also enclosed the proton beam for about 10 feet downstream of the target. The feature reduced the counting rate in the helium detector by minimizing air-induced spray.

For photon detection, we used two independent telescope systems. Each shower counter was designed to provide both position and energy information on incident photons. They consisted basically of a $2X^{o}$ lead glass converter, a set of wire spark chambers, and lead glass absorber, at least $8X^{o}$ thick (refer to Fig. 6.12). A veto counter was placed before the $2X^{o}$ converter to allow only passing neutrals. A counter was placed directly behind the $2X^{o}$ converter to detect charged products. This counter was part of the event trigger. The output signals from the converter and the absorber were added to give a signal proportional to the photon energy. The energy resolution is important in helping to separate the background, primarily photons, from the decay of π^{o}'s in the process $pd \rightarrow He^{3}\pi^{o}$, $\pi^{o} \rightarrow \gamma\gamma$. One of the counters was an updated version of one designed and built about fifteen years ago[6]. The glass composing the absorber was quite yellow, and non-uniform, raising the energy resolution to about 10% at 500 MeV. The other counter was designed specifically to detect photons in the energy region .1 to .6 GeV[7]. It employed high quantum efficiency photomultiplier tubes, very clear and uniform lead glass, and a liquid-filled light pipe between the absorber and the photomultiplier tubes. The energy resolution of this counter is on the order of 7% at 500 MeV. With the 7% to 10% energy resolution, much of the background can be

eliminated using energy alone. Construction details appear in Appendix D.

The information from the spark chambers which were located between the converter and total absorber, is used to construct a conversion vertex, to make the angle of photon emission measurable. The counters were mounted on moveable three-legged tables, each leg of which could be independently adjusted in height. These tables were in turn attached to adjustable radius arms. The whole apparatus could then be moved in circular trajectories, and adjusted between about 28° and 119° with respect to the beam line. Data were taken about every 15° in the e center of mass system (see Fig. 2.1).

A special purpose computer[20] was employed to gather information for each event trigger, and to store the information prior to writing it onto magnetic tape. The device consisted of a 512 twelve-bit-word data buffer, capable of storing enough information for two event triggers, a data bus system used to access information from the experimental apparatus, and a tape unit.

Digital information was obtained from event scalers, wire spark chamber word scalers, and six analog to digital converters. In addition, selected data buffer words were hard wired to specific values. These were later used to check the fidelity of data transmission to magnetic tape. In practice only two runs had to be rejected for errors of this type.

A simplified schematic of the electronics is shown in Figure 2.3.

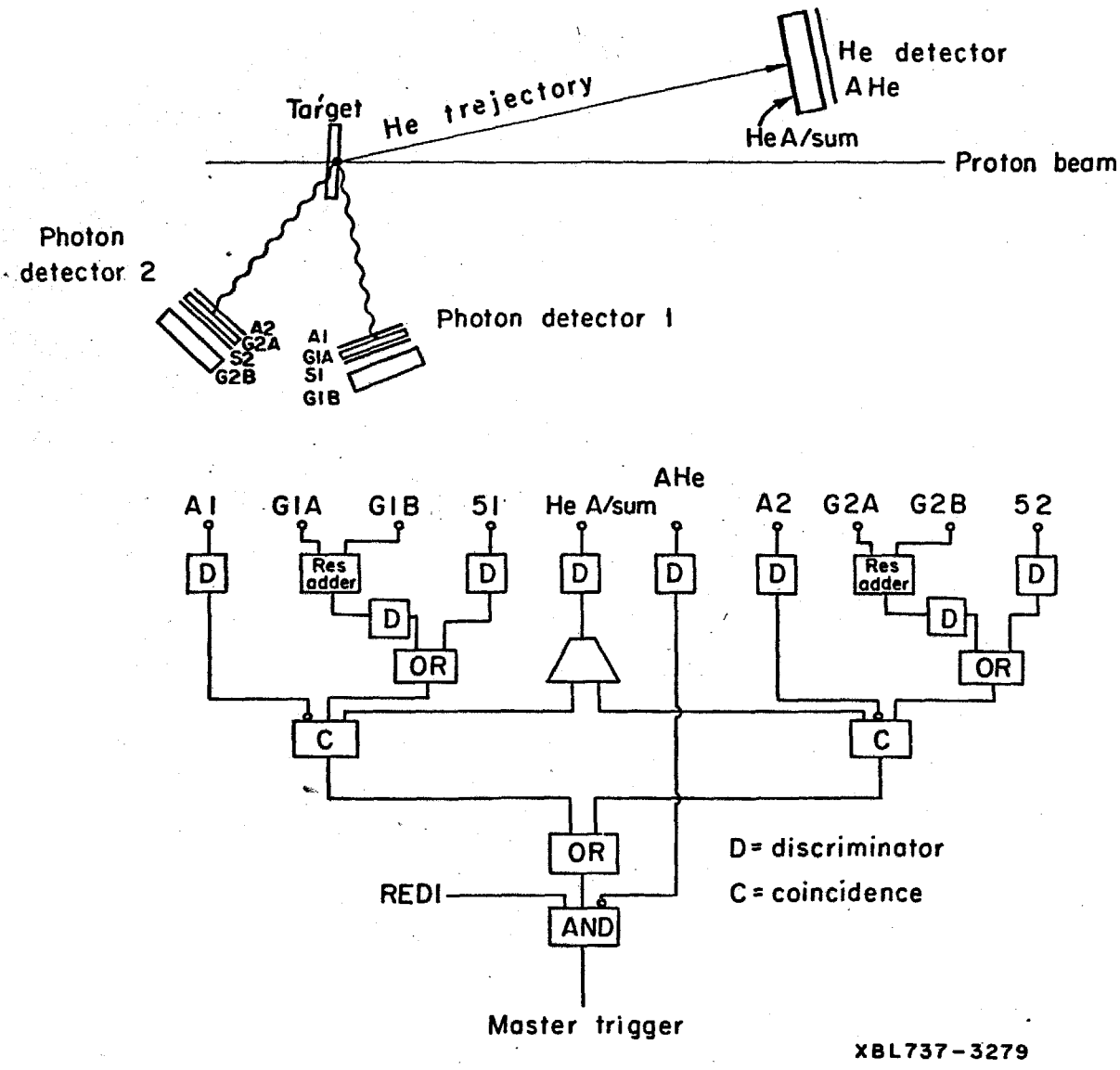

Figure 2.3 Simplified Schematic of the Electronics

Consider either photon detector. An event trigger consisted of no signal from the photon detector veto, a signal from either the lead glass converter or the lead block absorber, a "conversion" counter, located behind the converter; a signal from the helium detector, appropriate pulse height from the $\frac{dE}{dx}$ counter, and no signal from the helium veto; a ready signal from the data recording apparatus. Signals from the two photon detectors were orred, making the logic sensitive to the three body process $pd \rightarrow He^3\pi^o$, $(\pi^o \rightarrow \gamma\gamma)$.

Not shown are the analog to digital converters (ADC's) used in recording pulse heights from the converter and block of each photon detector, and the helium detector. Time of flight was recorded as the difference between the helium flight time and that of the photon. Finally, the amplitude of the differential pulse height counter was recorded.

DATA TAKING

Run Procedure - General

Data collecting for the experiment was a fairly dynamic process for the experimenters. Formal equipment checks were made every hour. On every fourth such hourly check, a more extensive equipment check was made, and on every eighth hourly check, all tube voltages were also measured. At all times the experimenters were expected to keep one eye on such things as spark chamber wand performance, the target liquid level (including periodical visual checks of the target flask for any bubbling), beam steering, beam intensity, amount of magnetic tape remaining, shape of beam spill, and other things prone to rather sudden failure or depletion. Between hourly checks, various calculations were performed, and the results tabulated so that any serious drift or equipment malfunction could be detected. At the end of each run and at every hourly check, hard copy was obtained of all scalers, and of the helium detector pulse height analyzer.

1. Hourly Checks

Figure 3.1 is one of the hourly check sheets from the experiment, and illustrates the kinds of information of interest. Most of the information is directed at trying to detect equipment malfunctions, and involved someone looking at a gauge, liquid level, or oscilloscope, and recording the information. Using scaler information, consistency checks were made by correlating the performance of various pieces of apparatus. If any of the checks were found to be outside of acceptable limits, corrective action was taken. Three separate beam integrators were simultaneously

"HOURLY" CHECKS

DATE: 6/2
TIME: 0015
OBSERVER: KTM
RUN: 338

RESET TIMER TO 90 MINUTES. DON'T RELAX.

PRINT OUT 3 EVENTS. A) MIDDUS TYPE CONTROL SWITCH TO 'ACTIVE'
B) STOP RUN AS SOON AS EVENT STARTS PRINTING
C) SWITCH TO 'INACTIVE' AND THEN START RUN.
MAKE SURE THAT YOU GET ONE EVENT FROM EACH GAMMA TRIGGER.

BEAM OFF. REZERO SPLIT I.C. ELECTROMETERS IF NECESSARY. WAS IT NO

HE BAG FLOW O.K. _____
CU. FT. REMAINING IN HE BOTTLE 450

HYDROGEN RESERVOIR LEVEL 10
DEUTERIUM RESERVOIR LEVEL 1
FLASK LEVEL PINNED
DEUT. RES. PRESSURE (OUTSIDE GUAGE) 16

SPARK CHAMBER HIGH VOLTAGE. GAMMAS 12.5 HELIUM 12.5
NEON FLOW TO SPK CH 9.5, FROM SPK CH 11: ALCOHOL ~~1~~
TRAP LAST CHANGED 3 HOURS (AEONS) AGO.

SNOUT READING (ASK CONTROL) 1.1X10^-8

ARE THE STABILISERS STABILISING _____
DO THE PULSER AND PEDESTAL OCCUR OUTSIDE THE SPILL GATE _____
IS THE SPIKE JUST OUTSIDE THE SPILL GATE _____
IS THE SPIKE ADEQUATELY MODEST IN MAGNITUDE _____

AMOUNT OF MAGNETIC TAPE REMAINING 1600 FEET

IS THE FILE PROTECT LIGHT OFF _____
<- 63 LIGHTS BEAMING? IS BIDL OF WORD 1 SENSIBLE _____
ARE BITS 5, 12, 24 SET REGULARLY _____ (BAD IF SO)
EVENT SCALER INCREMENTING O.K. _____

WHAT IS 'N' FOR TEL/N (DECADE OUT OF 26) 1

ARE ALL JACKSON SCALERS SWITCHED TO 'GATE' ALL ON 20MS
ARE ALL THRESHOLDS ON JACKSONS AT THEIR BLACK DOT VALUES _____

CHECKS DERIVED FROM 3-EVENT PRINT OUT.

ARE FIDUCIALS PRESENT AND CORRECT ON ALL WANDS _____
ANY DOUBLE-COUNTING OF SPARKS/FIDUCIALS _____
ANYTHING ODD ABOUT THE TRACKS NO

ANY 'ØØØØØ' ENTRIES IN AMONGST THE JACKSON SCALERS NO
IF SO, TRACK THE PROBLEM DOWN RELENTLESSLY.
(24)+(1)-(23)-(22) = 43

COMPUTE (ON STANDARD SHEET) CERTAIN CRITICALIA AS OBSERVED BETWEEN THIS CHECK AND THE LAST.

IS THIS THE FOURTH CHECK SINCE THE LAST 4-HOUR CHECK 1

RELAX.

Figure 3.1 Hourly Check

used in the experiment. Every hour ratios for every pair of integrator outputs were computed and recorded. Changes in any of these ratios indicated a drift in one of the integrator systems. A large drift might indicate an anomalously high leakage current for example.

The consistency of the triggers per beam integrator unit was a useful check on the general condition of the logic electronics and the liquid level of the target. A change in this quantity outside statistics might indicate some kind of failure in a logic unit, cable, etc. It might also indicate that the target liquid level had changed, or that noticeable boiling of the liquid led to bubbling. By observing the ratio of integrators, mentioned above, one could insure that the integrator used as a reference was itself stable.

The line time of the apparatus is the fraction of time it is able to detect the presence of an event. During the period in which information about an event is being recorded the apparatus gated off, and is unavailable for further event detection. If another event trigger occurs during this period, it will not be recorded. In order to correct for the number of event triggers lost in this way, a scaler measured the output of the fast logic at all times. Another recorded the output only when the event recording apparatus was gated on. The ratio of these scalers is a measure of the live time.

A small live time might indicate that the beam intensity is too high, producing a large number of spurious triggers, or accidentals. It might also indicate some kind of failure in a counter. Examples include light

leaks, or a failing veto counter. We collected data at the highest beam rate consistent with a live time of at least 95%.

There is a natural tendency for the cyclotron beam to form bunches due to the stability criteria of the frequency modulated mode of operation. As the beam exist from the machine, it is in the form of narrow high intensity pulses, perhaps 7 nanoseconds wide. In order to perform coincidence experiments it is necessary to have a beam with less intensity and greater duration in order to minimize the effects of accidental triggers. In order to achieve this condition, the beam exits the machine a little at a time. With care, the machine operators are able to release about 95% of the beam. The resulting beam spill still contains a spike due to inefficiencies in slow extraction. This spike, containing 5% of the beam, can be gated out.

We had two ways of monitoring the ratio of spike to spill, which we attempted to maintain at a level of 1/20 or less. One was to use the beam structure display on an oscilloscope; from this a crude measure of the ratio was made. More accurately, a separate beam integrator system measured both components of the beam, spike and spill. Comparing this with one of the other integrator systems, which were gated so as to measure on the spill, enabled us to monitor the fraction contained in the spike.

In summary, during each hourly check we derived and tabulated the:

1. relative ion chamber performance;
2. triggers per unit of ion chamber output;
3. live time of the apparatus;
4. relative amount of spike and spill in the beam.

2. 4-Hourly and 8-Hourly Checks

Figure 3.2 is a typical 4-hourly check sheet. Four kinds of information are of interest here:

1. checks to insure that equipment settings are at their nominal values;
2. qualitative checks on counter performance;
3. checks on spark chamber performance.

Item one entailed a quick check of the logic electronics for misset switches, loose cables, etc. At this time the magnet settings were checked, and also the steering of the beam, which was monitored by split ion chambers. Finally, readings of the high voltage power supplies were made and compared to nominal values for consistency.

Each counter in the experiment contained a light emitting diode. In addition to its use as a timing aid, the diode served as a crude reference against which the performance of the phototubes was checked. Every four hours, the diodes, driven by a pulse generator set to a standard voltage, were turned on and the output pulses of specific phototubes were photographed. Typical pulses are shown in Figure 3.2. The pulses were checked against previous photographs for consistency. Substandard pulses were a clue to either power supply drift, phototube fatigue, or perhaps physical damage to the counter.

The last item served to monitor the condition of the wire spark chambers. We ran visual checks of the output signals from the spark chamber wands on an oscilloscope.

4-HOURLY CHECK LIST

DATE: 6/1
TIME: 2300
WHO YOU: KTM
RUN: 338

BENDING MAGNET SETTINGS
BEAM OFF. NULL THE SPLIT I.C. ELECTROMETERS AFTER NOTING OFFSETS. Zero potentiometer on standard cell.
FRONT -.1
BACK -.1
ADJUST ATLAS TO CENTER BEAM ON BACK SIC.

NESTOR 26.73
ADONIS 29.68
ACHILLES 27.28
ATLAS 29.045

SPLIT ION CHAMBERS

SCALE SETTINGS: FRONT 25, BACK 250 4.29
MOVE FRONT S.I.C. TILL A NULL IS OBTAINED. ITS POSN. _____
MARK DATE AND TIME ON STRIP CHARTS.

VOLTAGES

METER READINGS OF H.V. SUPPLIES 1.2740
2.3003
3.2056

EVERY OTHER 4-HOUR CHECK, DO A COMPLETE H.V. CHECK.
WAS THE COMPARISON SATISFACTORY.
WHAT WAS THE GREATEST DEVIATION FROM THE PROTOTYPE VOLTAGES. -4V
WHICH COUNTER WAS IT S2

ARE ALL LINEAR GATES, AND IS THE 'TAC', AT BLACK-DOT SETTINGS

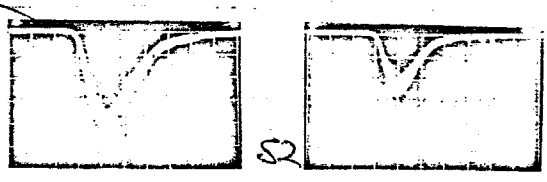

SCINTILLATORS

STOP THE RUN. TURN ON THE DIODE PULSER. TAKE POLAROID PHOTOS (TRIGGERED ON THE DIODE PULSER) OF COUNTERS: S1, S2, A1, A2, HE-ANTI AND DE/DX. ALL PHOTOS TAKEN AT THE INPUTS TO THE DISCRIMINATORS.
STANDARD 'SCOPE SETTINGS:
Ø.2 VOLT, 1Ø NS. / CM
EXCEPT FOR DE/DX WHICH IS
Ø.1 VOLT, 1Ø NS. / CM.

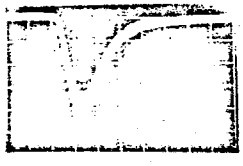

HAVE YOU NOW TURNED OFF THE DIODE PULSER _____

RECORD THE SETTINGS (INPUT ATTEN X OUTPUT GAIN) OF ALL NANOAMPLIFIERS.

BIN 11

G2C AMP		G1 NA1	G2 NA2.5	G2 NA3	G2 NA1 ONE KNOB	G2 ADDER
.2X10		.5X10	1	.1X10	5	
A/CUP		G1 NA2	G1 NA2.5	G1 NA3	G2 NA2 ONE KNOB	
.5		.2X10		.1X5	5	

BIN 2/2

A/SUM
1X10
G1C AMP
.2 X 10

Figure 3.2 4-Hourly Check

On the order of ten pulses were observed for each 24 wands. Of interest were missing fiducials, weak or missing signals, and double pulsing. This information, plus a mentally averaged pulse height for each wand, was recorded, and appropriate action taken for troublesome wands. If many wands were weak this indicated that the gas purifying system needed attention. Multiple pulsing suggested either a defect in the wand causing reflections, a missteered beam, or a large beam halo from an overintense beam.

The 8-hourly checks were performed at every other 4-hourly check, and added a check of all power supply voltages to the above. Figure 3.3 shows a typical 8-hourly check list. We would be remiss if we did not report that, unaccountably, this procedure did not catch the only power supply failure of the experiment. It occurred during one of the weekend cyclotron shutdowns, a six hour period during which most of the apparatus was left running, with one somewhat sleepy experimenter left to keep watch. The power supply self-annihilated, burning part of the experimental shack, and was observed only accidently, while in flames, by one of the experimenters making one last check before retiring.

3. Preliminary Analysis

After each run, a rough analysis of the data tape generated was made to determine the general quality of the data, and aid in decision making for future data collection. This was especially helpful during the initial phases of the experiment. Quantitative information was obtained for spark chamber efficiencies, and general information about the data, for example, whether any signal was present.

PHOTOTUBE VOLTAGES

DATE 2 JUNE

OBS. DF

ZENER	ORANGE = 1	GRAY = 2	MISC.
T1 = 2215	1 = 2164	1 = 458.5	A2 = 2364
T2 = 2215	2 = 2487	2 = 458.9	S2 = 2343
T3 = 2598	3 = 2384	3 = 512.8	SLAB 2 = 2105
DM1 = 2496	4 = 2529	4 = 494.8	A1 = 2224
DM2 = 2496	5 = 2467	5 = 445.0	S1 = 2404
DM3 = 2740	6 = 2323	6 = 438.3	SLAB 1 = 2404
DM4 = 2435	7 = 2344	7 = 446.3	
DM5 = 2598			dE/dx = 0
DM6 = 2699			
PM1 = 2296			
PM2 = 2216		HE COUNTER STUFF	
PM3 = 2216		-HV1 582.34	
PM4 = 2216		2 585.16	
PM5 = 2296		3 587.85	
ANTI 1 = 2801		4 564.46	
ANTI 2 = 2801		+HV 92.98	
ANTI 3 = 2699		LP 559.76	
EXT 1 =		8575 791.06	
EXT 2 =			
EXT 3 =			

Figure 3.3 8-Hourly Check

During production running this was not done for every run, but served only as a periodic check on overall system performance.

4. Calibrations

During normal shutdowns, accelerator maintenance for example, calibrations were made of the integrators and the helium counter. The integrators were checked using a standard current source (see Appendix N). The helium counter was checked against an Americium-241 source (see Appendix F), which served as an absolute standard. Making a straight line fit to a linear portion of the energy spectrum, one could extrapolate this line to a specific channel in a pulse height analyzer. The gain of the system now fixed to a known value, one could adjust the pulse height of the argon glow lamp if necessary.

5. Information Collected

Table 3.1 summarizes the information collected for each event. A data buffer, locally known as Alpha-63,[20] was used to store an event. The buffer stored two events, a total of 512 twelve-bit words, which were subsequently recorded on magnetic tape.

Some bits in the system were hard wired at various levels to fixed values. During the analysis, these hard wired bits could be used to monitor the efficiency with which data was transmitted to magnetic tape.

The time-of-flight, photon converter and absorber pulse heights, and differential pulse height counter information was obtained from 9-bit digitizers. The helium counter pulse height was obtained from the output of a 400 channel pulse height analyzer.

Alpha-63 Word (12 bits)	Contents
1 - 2	Event number, Ridl
3	Latches
4 - 66	Photon counter spark chamber wands
67 - 130	Helium detector spark chamber wands
131 - 136	Six ADC's
137	Run number
139 - 255	Scalers

Table 3.1 Alpha-63 Output

Figure 3.4 is a typical run sheet used while taking data. Counter positions, times, and the electronics configuration were recorded before the run, and the nominal beam level noted.

At the end of a run, the following items were gathered:

1. Time, at the end of a run.
2. A paper copy of the helium counter pulse height spectrum, as well as a photograph.
3. Certain scalers were recorded by hand.
4. A fake event was accumulated, and all of the scalers printed out on a typewriter, subsequently fastened to the data sheet.
5. Barometric and atmospheric conditions.

For various checking purposes, we studied larger cross section reactions with our equipment. Table 3.2 mentions them and gives the number of triggers gathered for each type. Table 3.3 shows the center of mass angles at which data were taken, for each beam energy. In particular 90^{o} points were taken at each energy so the energy dependence of the cross-section could be studied; this angle also was easiest to compare with other data.

Reaction	Energy	Run Interval 130-259	260-367	Sum
$pd \rightarrow He^3\gamma$	383		31,416	31,416
" "	462	592,143	887,542	1,479,685
" "	558		115,872	115,872
$pp \rightarrow pp$	462	34,406	1,500	35,906
$pd \rightarrow He^3\pi^o$	383		26,009	26,009
" "	462	1,230		1,230
$\alpha p \rightarrow He^3 d$	324	9,976	53,070	63,046
$dp \rightarrow He^3\gamma$	420		27,723	27,723
$pp \rightarrow d\pi^+$	558	44,005		44,005
			TOTAL	1,824,408

Table 3.2 Kinds of Data Collected

HELIUM CENTER OF MASS ANGLE							
Beam Energy	45	60	75	90	105	120	135
462	X	X	X	X	X	X	X
571		X		X			
377				X			

TABLE 3.3 - Kinematic settings for which data were collected.

REACTION pd → he x

RUN# 298 TAPE# 109 LIB# 24809 DATE 22 MAY TIME: START 07.35 STOP _____

SNOUT IC 2.8 x10⁻⁸

IC	INTEGOR	SCALER	SCALE
			x10
			x10
			x10

TGT LD_2 BEAM ENERGY 57± MEV

G1 THETA (71) ° R (26) "

G2 THETA (103) ° R (41 ½) "

He POSITION: HGT (5.0) HOR (35) "

TAC: START _____ ns STOP _____ ns

6xHe _____ ns

2xHe _____ ns

DELAY BOX SWITCHES

A1 ___ A2 ___

S1 ___ S2 ___

G1 ___ G2 ___

G1C ___ G2C ___

	U3=GAM$_2$	U7=GAM$_1$
He db		
He E		
He ΔE		
DX db		

A/SUM RANGAMP _____

U21: G1 (S1) U3: A2 He G2 DX U0: S1 S2 U11: 1 2 (C) U14: (3 C7 C3/A

U22: G2 (S2) U7: A1 He G1 DX U20: G1 G2 812 U24: (A_{he}) TT EG U16: (TEL/N) LCOS3

BEFORE RUN U4: (A/HE U3) TT DX U8: (A/HE U7) TT DX T=1/ 2

AFTER RUN

EVENT # 47441 24/ 34499 25/ 20257 29/ 49032

40 2361804 41 7401211 48 887321 49 6803145 50 87683 51 5701841 52 1881323

TSI-1/ _____ TSI-2/ 120584 TSI-3/ 188570 TSI-4/ 17723

298

Ø1 ØØ11578	Ø2 ØØ62146	Ø3 ØØØ2371	Ø4 ØØØ172Ø	Ø5 Ø225622	Ø6 Ø27Ø843
Ø7 ØØ38815	Ø8 ØØ32Ø98	Ø9 Ø733824	1Ø 1714652	11 ØØØØØØ7	12 ØØ41152
21 ØØ23764	22 ØØ337Ø1	23 ØØ19459	24 ØØ34499	25 ØØ2Ø257	26 Ø1Ø438Ø
27 1284ØØ8	28 1576281Ø	29 ØØ49Ø32	3Ø Ø222877	31 4864114	32 Ø1689Ø7
41 ØØ18876	42 ØØØ3325	43 ØØ1Ø943	44 ØØØ8497	45 ØØØ2849	

COMMENTS: End run - tape full

Figure 3.4 Run Sheet

DATA ANALYSIS

In this section the procedure is described by which the total of about a million triggers were reduced to a set of angular cross section values. It was convenient, for economic reasons, to separate this process into three categories:

1. Data formatting, photon vertex reconstruction, helium track reconstruction, spark chamber efficiency determination.
2. Geometrical reconstruction, kinematic fitting.
3. Cross section extraction.

We divide this discussion into eight parts:

In Part 1 we discuss the method of storing various constants useful in the analysis of a run. Part 2 outlines the structure of the data summary program, which reformats the raw data, calculates chamber efficiencies, and uses chamber dimensions to construct coordinates relative to the chamber plane.

Part 3 explains the construction of various kinematic and geometric quantities, and the procedure for generating a χ^2 for each event combination. In Part 4 various cuts are examined.

In Part 5 we describe the calculation of various efficiencies, and Part 6 outlines the calculation of cross sections. Part 7 gives details on the various background subtraction procedures. Finally, in Part 8 we discuss the errors incurred in the calculation of cross sections.

More detailed discussions of various aspects of the analysis can be found in the Appendices.

1. Constants

Approximately 70 constants (where by constant we mean a function of run number, but hopefully not of time) were collected for each of about 300 runs. Included were quantities like target thickness, distances from the target to each photon detector, presence or absence of the differential pulse height counter, reaction type, etc. It was decided that this information would be gathered in one place and stored in the computer during the data analysis. During the data analysis one needed only to specify a run number, and all of the information pertaining to the run was automatically retrieved. By reducing the amount of information one had to handle manually for each run, it was hoped the number of errors resulting would be reduced correspondingly.

2. Data Summary Program

The first of three stages of analysis performed four functions:

1. The raw data were unpacked from 12 bit computer words and reformatted into 60 bit computer words.
2. Spark chamber wand scaler values and survey information were combined to produce coordinates in the spark chamber frame of reference.
3. Photon vertices were derived from shower tracks in the photon counter spark chambers.
4. Spark chamber efficiencies were calculated.

The raw data came in the form of 12 bit computer words. The first operation performed by the data summary program (DSP) was to unpack these 12 bit words and from them construct 60 bit words, representing scaler values, ADC's, etc. This was primarily format conversion.

The spark chamber wand scaler values and the physical dimensions of the spark chambers themselves, were then combined to produce coordinates relative to the spark chambers. Appendix G describes the procedure for the helium chambers. Appendix E describes the determination of the shower origin in the photon chambers, and the assignment of errors on these positions.

The following information was produced event by event, and summarized in tables and graphs for the whole run:

1. Histograms of the number of sparks on each wand, excluding fiducials.
2. A histogram displaying the number of times a specific set of chambers contained sparks, as a percentage of the total number of triggers.
3. Histograms of the distance from any spark to a fitted point or lines in the helium and photon chambers. This was taken as a measure of the goodness of fit.
4. A table of individual wand efficiencies for all wands, based on suitably defined "probe" events for each set of chambers.
5. Histograms of the spark locations for each wand, and of the number lacking fiducials.
6. Plots of scaler ratios, performed every N events, where the user specifies N. Refer to the section on data collection for details of these quantities.
7. A grid showing correlations between various fast logics bits.

Finally, some of the hard-wired bits were checked. Some bits in the special purpose computer were fixed to be specific values. These were

later used as a check of the fidelity of transmission of the data to magnetic tape. A run was abandoned if too many data transmission errors were found, indicating hardware problems in the data recording systems. In practice only about two runs were lost in this way. Appendix I gives some details of the structure of the data summary program, and a table of its output.

Spark Chamber Efficiencies

A. Helium Chambers.

The procedure for calculating chamber efficiencies involved first obtaining a subset of events called probe events which were used to investigate the efficiencies of individual gaps and wands. A probe event is defined as an event for which at least three of four gaps have sparks, and a track constructed from the sparks extrapolates to the active area of the target. The latter constraint is to ensure that the probe events are in fact due to particle tracks, and not to spurious sparks.

Given a probe event, one makes the following test on an individual gap:

1. If there are sparks in all four gaps, the probe is a probe of any gap. Increment a scaler for each gap.
2. If one, and only one, gap has no spark, the probe is probe of that gap. Increment two scalers, one a scaler indicating a probe event, one indicating a failure for a particular gap.

The efficiencies of the individual wands are measured by noting the presence or not of a count of each wand for probe events.

The inefficiency for a wand is then:

$$e = \frac{\text{Number of test probes with no count of a wand}}{\text{Number of test probes}}$$

The wand efficiencies are then used to construct the helium chamber efficiencies.

B. Photon Chambers.

The procedure for establishing the wand and gap inefficiency for the photon chambers is identical to that for the helium chambers in all but one respect. The constraint that a track constructed from the sparks project back to the active area of the target can no longer be imposed. Here individual tracks from the photon shower are used to form probes, and these in general do not project back through the target. Other than that, the procedure is the same as for the helium chambers.

The assumptions made for the efficiency calculations are:

1. The efficiency calculated is independent of the kind of particle being used to make the probe, and in the region of interest here, independent of the energy of the particles.
2. For small numbers of sparks, on the order of three or four, the efficiency is independent of the number of sparks.

3. Geometry-Kinematics

Construction of kinematic quantities, using survey information and equipment calibrations, was performed in the second stage of the analysis, GEOKIN. Appendix H outlines the program flow of GEOKIN.

In order to calculate the azimuthal and polar angles for each of the final state particles, a trajectory is first constructed using a coordinate from each helium chamber. The intersection of the trajectory with the target midplane is taken to be the event origin. A beam direction is constructed through the origin. All coordinates are now corrected for any systematic beam variations.

Definitions of the angles are illustrated in Figure 4.1. The helium polar angle is the angle between the trajectory and the corrected beam direction. The azimuthal angle is the angle between the projection of the trajectory on the target midplane and the horizontal plane.

The azimuthal and polar angles for the photon are similarly constructed, using the event origin and a coordinate from one of the photon detectors.

The observed helium energy was calculated using an expression of the form:

$$T_c = A_o e^{A_1 x} + \sum_{i=2}^{6} A_i x^{i-2}$$

where x is the helium detector pulse height, corrected for any positional dependence. T_c is the helium kinetic energy at the surface of the detector. The kinetic energy at the target origin was obtained by correcting T_c for ionization losses incurred in passing from the target to the detector. The expression used for this was of the form:

$$T_t = c_o + c_1 T_c = c_2 e^{-c_3 T_c}$$

where T_t is the helium kinetic energy at the target origin. Two sets of c 's were used, one set for those runs using, and one set for those

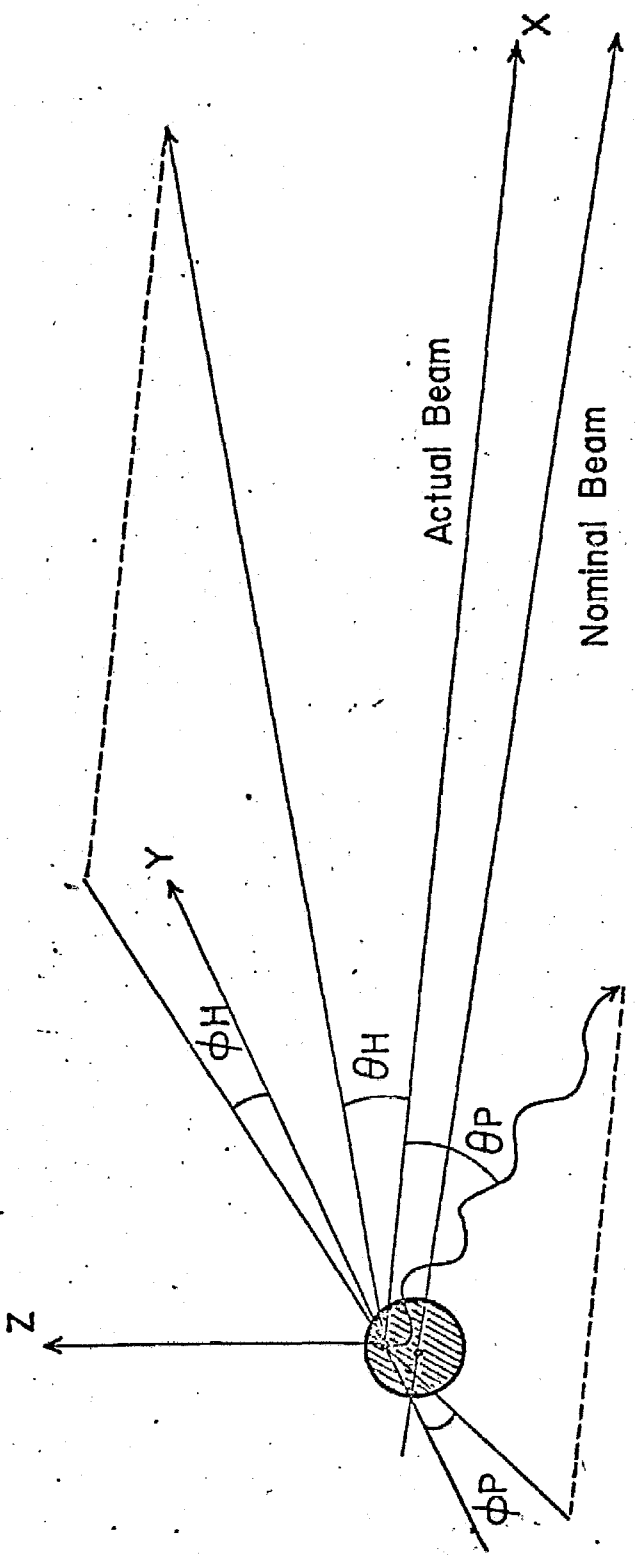

Figure 4.1 Definition of θ and ϕ Angles

runs not using a 1/8" differential pulse height counter.

Details of the method of calibration of this counter are found in Appendix F. The energy resolution of this counter was on the order to 3% HWHM, or a momentum resolution of 1.5% HWHM.

Corrections were made to the nominal beam energy for systematic angle and energy dispersions. Details can be found in Appendix A. Using the corrected beam energy, the helium kinetic energy and the measured angles of the photon and helium particles, a chi-square was generated. Details of the procedure are found in Appendix K.

Using momentum and energy balance, we can determine up to four unknown kinematic quantities by knowing the other twelve for a two body reaction. For example if sufficiently well measured, one could perform this experiment by knowing only the properties of the beam and target, and one final state particle, by doing a missing mass experiment. In the language of bubble chamber physics, this is a zero constraint fit, or 0-C, meaning that the reaction is not overdetermined, or, equivalently, has no redundant information.

Essentially one has four kinematic equations and four unknowns to solve. For each additional kinematic quantity measured, one overdetermines the solution by one, increasing the C of the fit by one. One now has more equations than unknowns. The technique for solving the equations is to adjust the unknowns until all of the equations are optimally satisfied. This is the essence of the kinematic fitting procedure.

Procedures for producing both 2 and 3-C fits were used. 2-C fits were employed where the energy of the final state was not known. 2-C fits served to analyze $\alpha + p \rightarrow He^3 + D$ data used to calibrate the helium detector.

For the $pd \rightarrow He^3\gamma$ data a 3-C fit was employed. We assumed the photon energy not to be known. Figure 4.6 shows a typical χ^2 plot.

The missing mass corresponding to the photon side of the experiment was computed in two ways. The first method computes

1) $$mm^2 = M^2 + 2(m_2E_1 - E_1E_3 + m_2E_3) + 2\,P_1P_3\cos\theta_{13}$$

where $M^2 = M_1^2 + M_2^2 + M_3^2$. Index 1 refers to the beam particle, 2 to the target deuteron, 3 to the helium particle. θ_{13} is the angle between the helium particle and the beam particle direction.

The second method uses the final particle angles only. P_3, the helium momentum, is calculated as:

$$P_3 = P_1/\sin(\theta_4 - \theta_3)$$

Using $E_3^2 = P_3^2 + M_3^2$, and substituting into equation 1), we obtain the desired result.

The center-of-mass angle of the helium particle was calculated to facilitate binning, and was used to calculate the kinematics of an event by an independent method from the χ^2 procedure described in Appendix K. Since each lab photon angle corresponds to a unique center of mass angle, it was used to compute the center of mass angle. In what follows, primed quantities refer to center-of-mass quantities, β and γ are the velocity

of the center of mass and $1/\sqrt{1-\beta^2}$, respectively. Defining the following quantities:

$$w = \gamma^2 P_3'^2 \tan^2\theta_4 + P_3'^2$$

$$x = 2\beta\gamma^2 P_3' E_4' \tan^2\theta_4$$

$$y = \beta^2\gamma^2 E_4'^2 \tan^2\theta_4 - P_3'^2$$

the cosine of the helium center of mass angle is calculated by

2) $$\cos\theta_3' = (-x + \text{sign}\sqrt{x2 - 4wy})/2w,$$

where sign = $\tan\theta_4/|\tan\theta_4|$.

4. Cuts

Several kinds of cuts were placed on the data, both to enhance the foreground-to-background signal, and to make the analysis more efficient. The following cuts were made:

1. coplanarity
2. vertex containment in target volume
3. containment of He^3 track in back wire chamber
4. dE/dx in differential pulseheight counter
5. time-of-flight and helium pulse height
6. helium angle and energy

The two-body reaction $pd \rightarrow He^3\gamma$ is required to be coplanar. A cut of $\pm 11^\circ$ was made on the coplanarity angle. Typical coplanarity plots, after applying dE/dx and target cuts, are shown in Figures 4.2, 4.3. Figure 4.2 is a favorable setting, 4.3 a difficult one. Figure 4.2 shows the intersection of the reconstructed helium trajectories with the target midplane, and indicates where a cut might be placed. Intersections outside of the indicated cut are due to spurious sparks in the helium wire spark chambers.

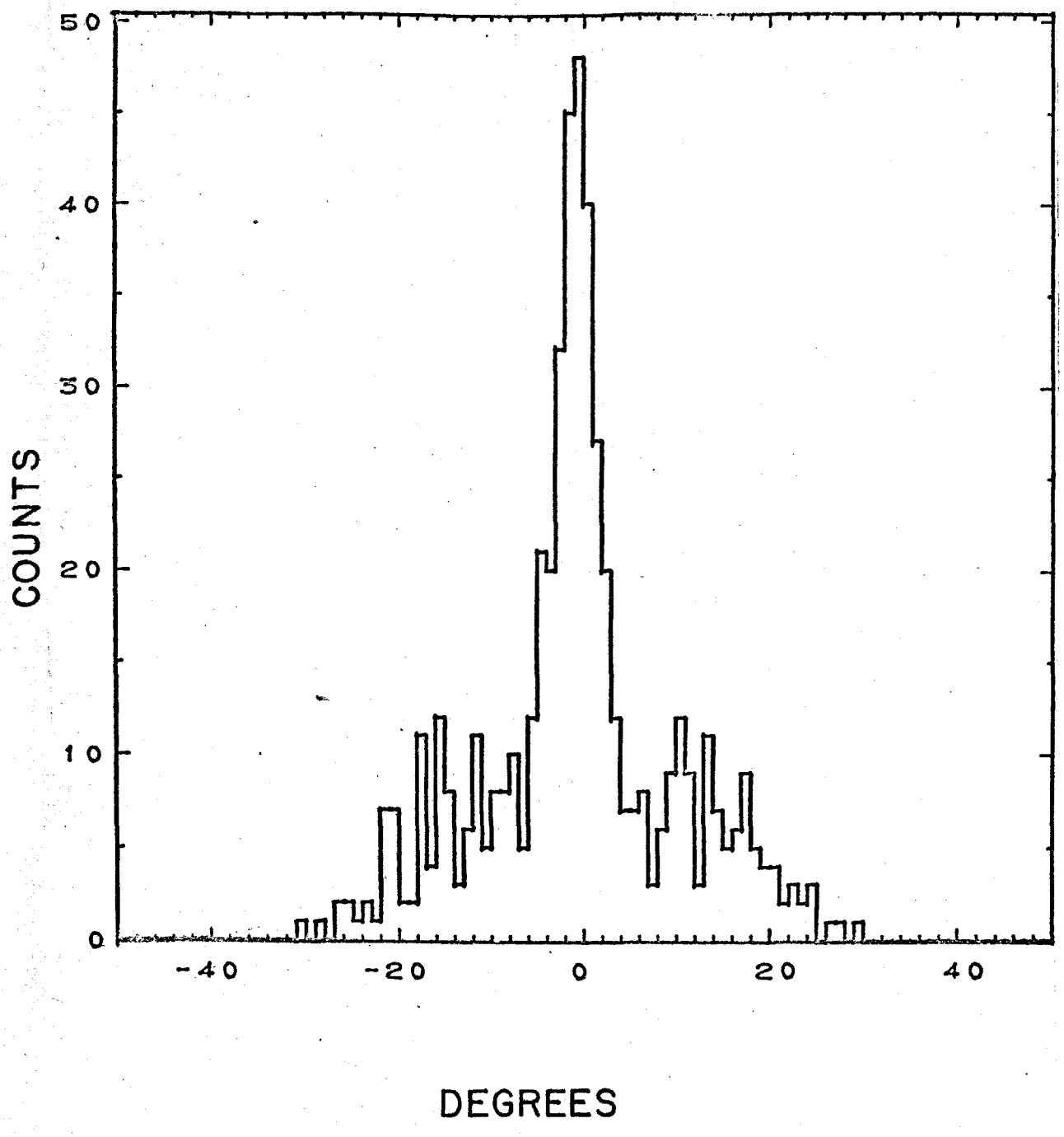

Figure 4.2 Coplanarity after a target cut, a DE/DX cut and a helium energy cut have been applied. Data is for a 90^{o} cm setting, and is one of the easier settings to separate background and foreground.

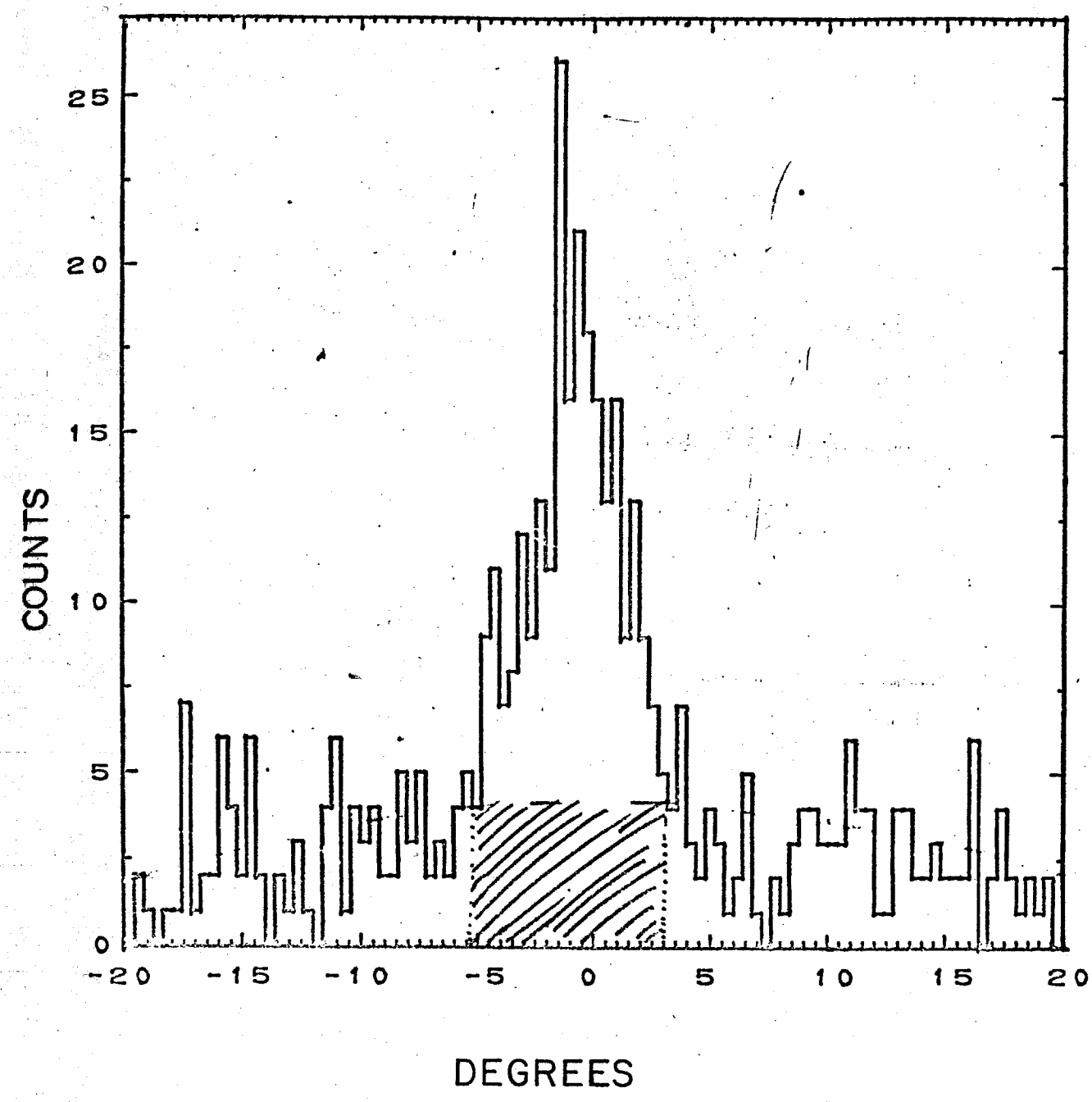

Figure 4.3 Coplanarity after a target cut, a DE/DX cut and a helium energy cut have been applied. Data is for a 45° cm setting, and is one of the more difficult runs for background separation.

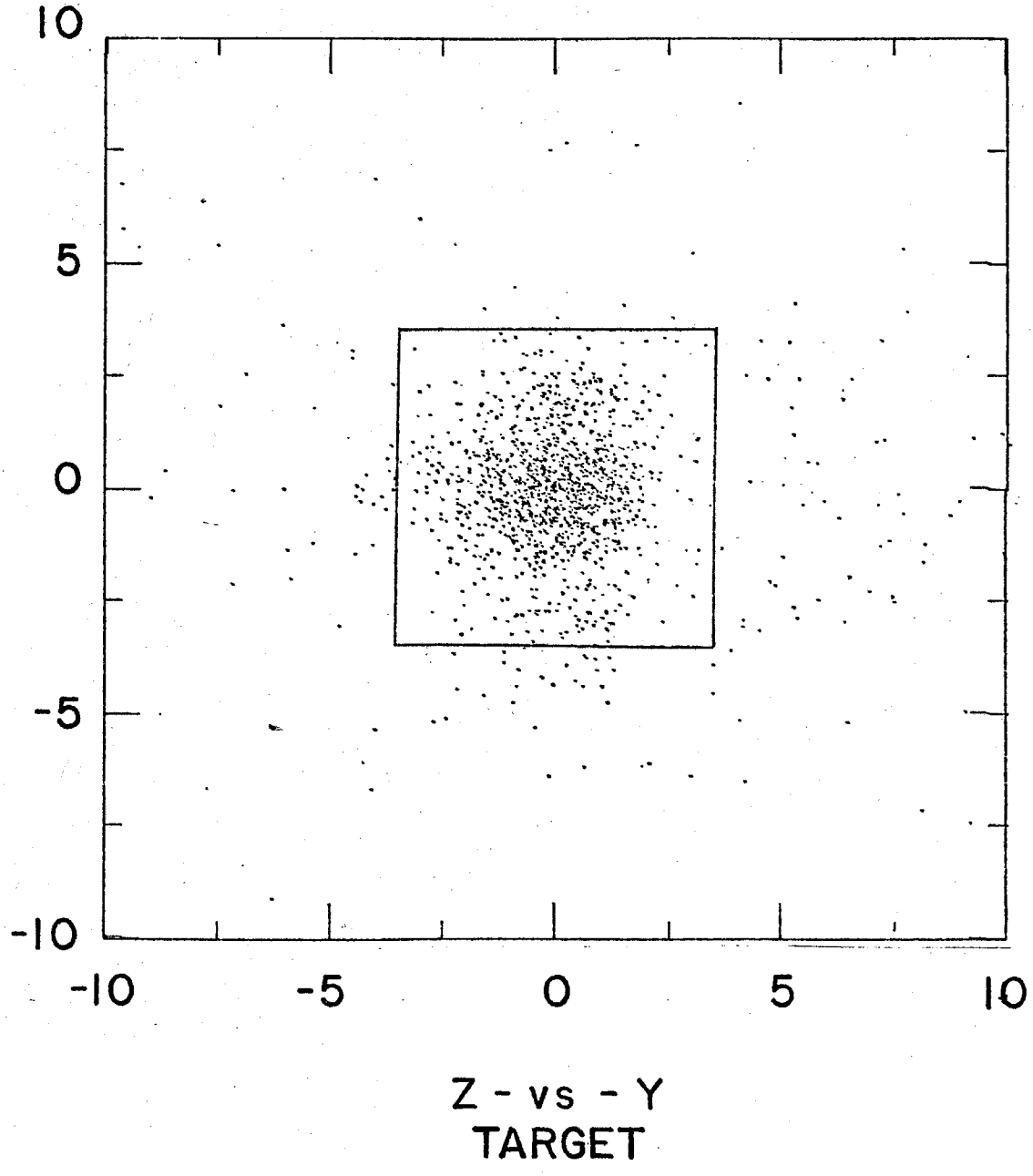

Figure 4.2 Reconstructed Event Origins

sparks in the helium wire spark chambers.

Local coordinates, for track-associated sparks in the wire chambers in the He^3 side relative to a chamber-centered coordinate system, corresponding to a given photon detector setting are restricted in position. A conservatively placed cut was placed around this region.

A differential pulse height counter was employed for those settings where the helium energy was high. Figure 4.3 is a distribution of pulse heights from this counter; the position of a conservatively placed cut for separating doubly ionizing from singly ionizing particles is indicated. This cut alone eliminated almost all triggers not containing a multiply charged particle.

For those runs employing the 1/6-inch liquid deuterium target the energy of the helium was too low for the differential pulse height counter to be used. The time-of-flight and helium detector pulse height information is correlated. In the energy region of this experiment, and for the particular experimental configuration used, the data for various reactions fall into well separated bands, as illustrated in Figure 4.4, which plots the time-of-flight ADC versus the helium detector ADC. Also indicated is the position of a possible cut; the triggers containing multiply charged particles lie above the indicated cut. As a check of this, only the upper band remains when a cut is made on the differential pulse height counter so as to include only multiply charged particles, for those runs employing the counter. Thus the differential pulse height counter and the time-of-flight and helium pulse height information pro-

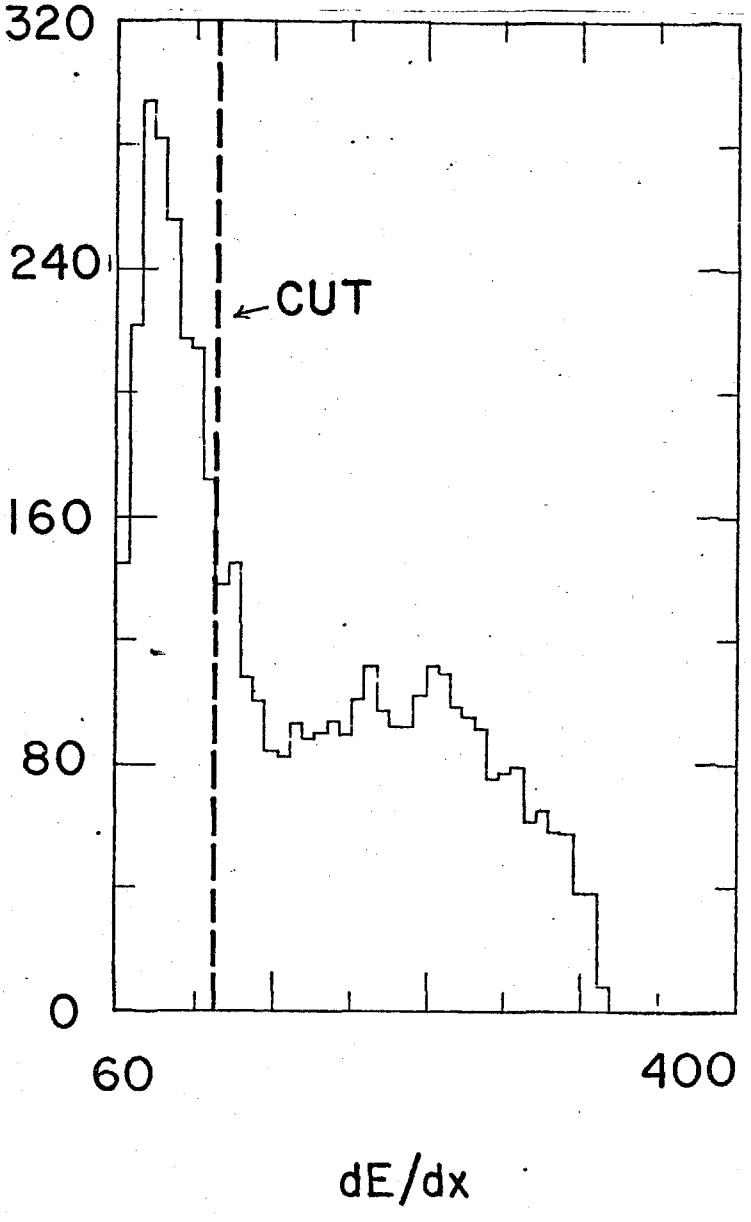

Figure 4.3 Differential Pulse Height Counter Spectrum

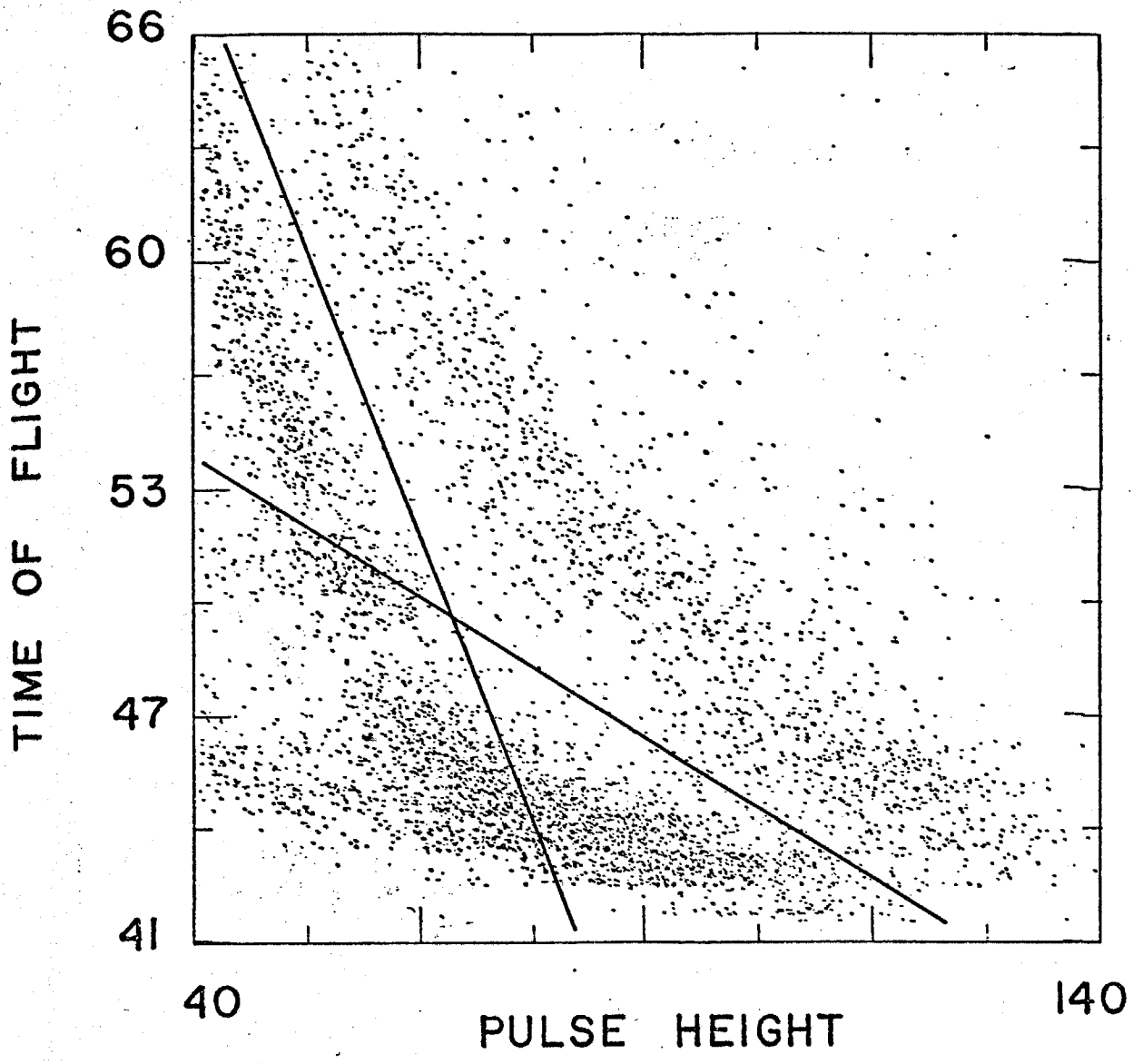

Figure 4.4 Time-of-Flight ADC Versus Helium Detector ADC

vide equivalent amounts of information. The differential pulse height counter was used where the He^3 energy was greater than 100 MeV (about 80% of the runs) to reduce the trigger rate from background processes.

Finally, a loose cut was placed on the correlated values of the helium lab angle and energy. This cut was effective in eliminating the background processes $p + d \rightarrow He^3 + \pi^o$, $(\pi^o \rightarrow \gamma\gamma)$ which, for a given photon detector setting, produced a much broader spectrum of angles and energies because it is a three body final state.

5. Efficiencies

In order to calculate cross sections we must first determine the efficiency of the apparatus for detecting an event of interest. Only after this efficiency is known can we transform the raw number of events produced by the data analysis into cross sections. The efficiency is in effect the probability that an event of interest will be detected.

The following factors will be considered in determining the overall detection efficiency:

A. Spark chamber efficiencies

B. Photon conversion efficiency

C. The geometric solid angle of the apparatus

D. He^3 breakup en route to the helium detector, and subsequent breakup in the detector

E. Counter and electronic efficiencies

Spark chamber efficiencies (Point A) have already been discussed,* and

*c.f. Data Summary Program, Part 2

will not be considered further. Photon conversion efficiencies (Point B) are discussed in Appendix D. Point D is discussed in Appendix F.6.

A. Geometric Solid Angle

The calculation of the geometric acceptance for this experiment was performed using Monte-Carlo techniques. These techniques have been discussed in detail elsewhere, and will not be elaborated upon here.[8,29]

The apparatus of this experiment was designed so that the geometric acceptance was determined solely by the photon counters. Total acceptance by the helium detector for any photon counter setting was one of the useful properties of using a large plastic detector. To be more precise, the solid angle was determined by the conversion counters located behind the $2\chi_o$ conversion slabs, and by the finite target size.

The wire chambers used for photon shower track delineation were made sufficiently larger than the trigger counter to minimize effects due to loss of tracks from the edges of the chambers. Monte-Carlo studies showed this effect to be less than 1%; we therefore ignored it.

The center-of-mass geometric acceptance is the quantity of interest for computing cross sections, and henceforth is the quantity referred to. The calculation proceeds as follows:

1. Using the distance of the trigger counter from the pivot, the target size, and the conversion counter size, we

determine a maximum azimuthal angle, and a minimum and maximum center of mass angle, θ_1, θ_2.

2. Within the region $2\Phi \cdot |\theta_2 - \theta_1|$, we generate $pd \rightarrow He^3\gamma$ events uniformly.

3. For a success, we inquire as to whether the photon converted. If it did not, label the trial a failure.

The geometric acceptance, in steredians, is then

$$\Omega = N_{success} \cdot 2\Phi \cdot |\theta_2 - \theta_1| / N_{trials}$$

The relative statistical error is determined by assuming that the successes and failures obey a binomial distribution, and is given by:

$$\Delta\Omega/\Omega = \frac{1}{\sqrt{N_{success}}} \cdot \sqrt{\frac{N_{trials} - N_{success}}{N_{trials} - 1}}$$

In order to minimize the amount of computer time used, it is advantageous to narrow down the range of Φ, θ initially in order to maximize the number of successes.

For each setting 40,000 trials were made. A typical geometric solid angle acceptance was on the order of .02332 ± .00029 steradian. Figure 4.5 illustrates a typical differential geometric solid angle.

Details of the program structure can be found in Appendix J. An independent check of the geometric acceptance calculations was made[58] for the reactions $pd \rightarrow He^3\gamma$ and $pd \rightarrow He^3\pi^o$ ($\pi^o \rightarrow \gamma\gamma$).

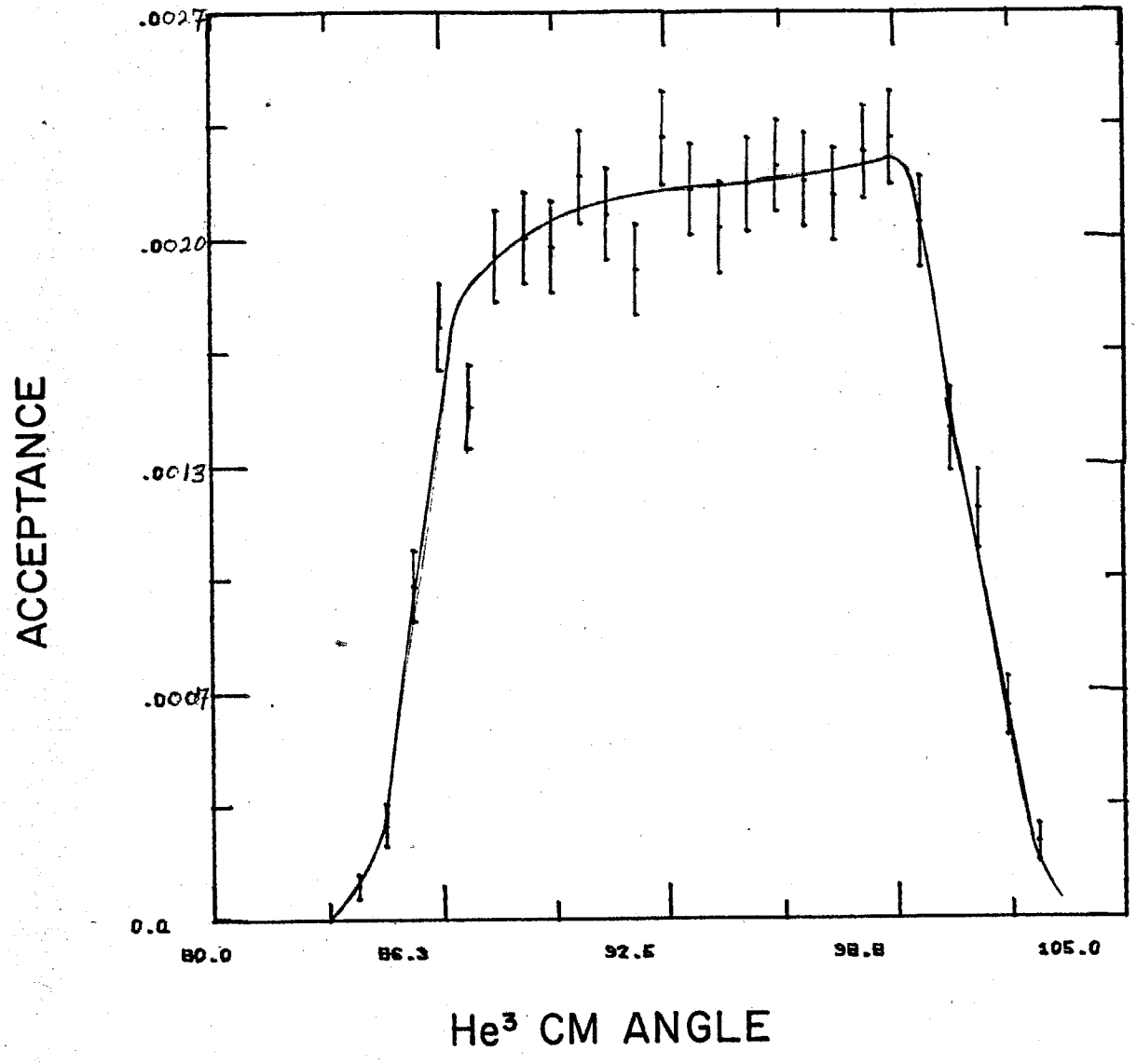

Figure 4.5 Typical Solid Angle Acceptance

The results agreed on the one percent level. Additionally, one can compute the lab solid angle for a two-body process rectangular detector using the formula[59]

$$\tan(\Omega) = ab/(c(c^2 + a^2 + b^2)^{\frac{1}{2}})$$

where a line from the source, of length c, intersects a corner of the detector, of size a,b. Special cases, checked by employing this formula, compare well with the Monte-Carlo calculations.

B. Electronic Efficiencies

The electronic efficiency is composed of individual counter efficiencies, the beam gate, and the total system dead time. The latter two factors were monitored constantly. The counters used in the event trigger were all more than 99% efficient; their contribution to the inefficiency of the system is taken to be negligible.

The spike-to-spill ratio (cf. Section 3.1) of the beam was monitored with a set of scalers. If properly tuned, the spike was never more than 5% of the total beam dump, and was typically 2%.

The system dead time (cf. Section 3.1) was determined by scaling all event signatures, as well as those occurring when a system ready gate was set. The dead time was as large as 20% for some settings, although typically it was less than 5%.

6. Cross Section Calculation

The differential cross section for a given setting is determined by the relation

$$N(\theta) = d\sigma(\theta)/d\Omega \times N_B \times Eff \times N_D$$

where:

θ = center of mass helium angle

$N(\theta)$ = number of events after background subtraction

$d\sigma(\theta)/d\Omega$ = differential cross section at a center of mass helium angle θ

N_B = number of beam particles = $2.85 \times 10^7 \times$ ORTECS

Eff = solid angle x electronic efficiency x spark chamber efficiency x He^3 breakup x photon conversion efficiency

N_D = number of target particles = $N_o \times t \times \rho/2$

N_o = Avogadro's Number = 6.023×10^{23}

t = target thickness

ρ = density of liquid deuterium, which was about .165 gm/cm^3

Thus

$$d\sigma(\theta)/d\Omega = N(\theta)/N_B \times Eff \times N_D$$

In general each run could have different values of each of the factors making up the differential cross section. McDonald[5] has shown that, assuming the number of events generated by a given run obeys a Poisson distribution, the value of the differential cross section that maximizes the likelihood function

$$L(x) = \pi_i (x\eta i)^{N_i} e^{-x\eta i}/(N_i)!$$

is given by

$$X = {}_i\Sigma N_i / {}_i\Sigma \eta_i$$

where η_i is all the remaining factors relating X, the differential cross section, and N_i.

Thus we compute the cross section for a set of runs as the ratio of the average number of events per run divided by the average efficiency. The relative error in X is given by

$$(\Delta x/x)^2 = (\Sigma_i \eta i^2 (\Sigma_j E_{j,i}^2))/(\Sigma \eta i)^2 + \frac{\Sigma Ni^2}{(\Sigma Ni)2}$$

where i labels the run, Ei,j is the relative error of the jth quantity, where j includes errors in:

1. target thickness
2. beam
3. total efficiency
4. background subtraction

7. Background Subtraction

The background subtraction was performed using a method of ratios. Using a center of mass angular distribution derived from analysis of the reaction pd → $He^3\pi^o$(37) (the largest background component - see Appendix L), background events were artificially generated using a Monte-Carlo program. These events were subsequently analyzed using a pd → $He^3\gamma$ hypothesis, and applying the same cuts used to analyze real data. The resulting chi-square distribution is that for the pd → $He^3\pi^o$ background only.

The method of background subtraction proceeds as follows:

1. Determine the ratio of events with $0 < \chi^2 < 10$ to that with $10 < \chi^2 < 20$, call this R, for the Monte Carlo events.
2. When extracting a cross section, tally the number of events with $10 < \chi^2 < 20$, call this N_B.

The number of real $p + d \rightarrow He^3 + \gamma$ events is then:

$$N = (N_T - R * N_B)/(1 - k - kR)$$

where

N = total real events

N_T = raw total events - i.e., events with $0 < \chi^2 < 10$

N_B = number of events with $10 < \chi^2 < 20$

R = ratio of foreground to background as determined by Monte-Carlo generated events

k = fraction of $pd \rightarrow He^3\gamma$ events with $\chi^2 > 10$

The R's depend on the specific geometry of the experimental apparatus, as well as any cuts applied during the analysis to suppress background. Different R's were generated for each angular setting. Table 4.1 lists the ratios used. Figure 4.6 illustrates a typical χ^2 distribution for 90^o cm data. The positions of the bins is indicated. Figure 4.7 illustrates a χ^2 distribution for 45^o cm data where the separation of the π^o background is more difficult.

8. Systematic Errors

The only systematic error in this experiment known to be larger than a percent was the thickness of the thin (nominally 1/6 inch) liquid deuterium target. During the course of data taking an effective change in thickness of about 25% was observed, as indicated by the target monitor rates (cf. Appendix B).

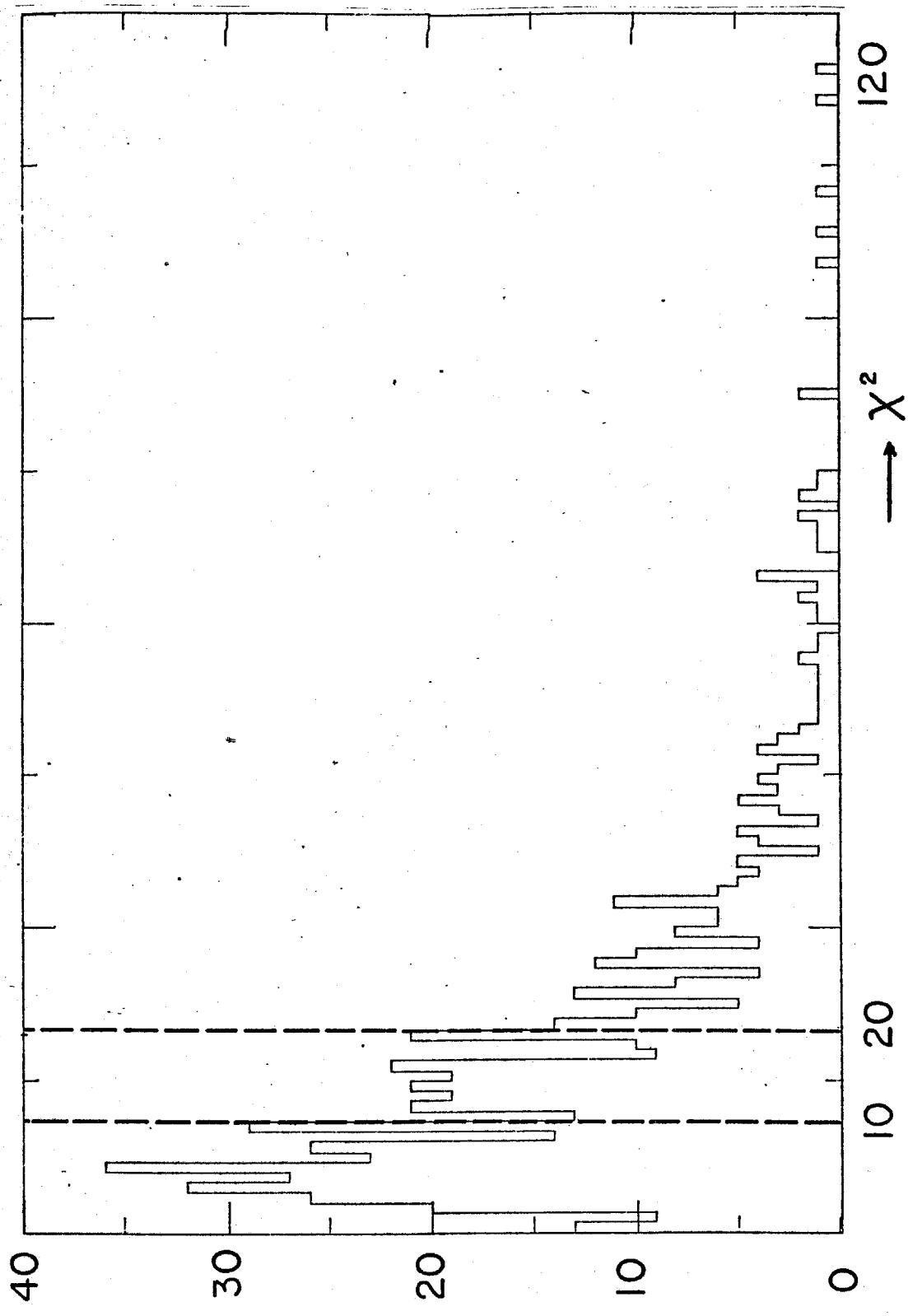

Figure 4.6 Typical Chi-Square Distribution for 90° cm data.

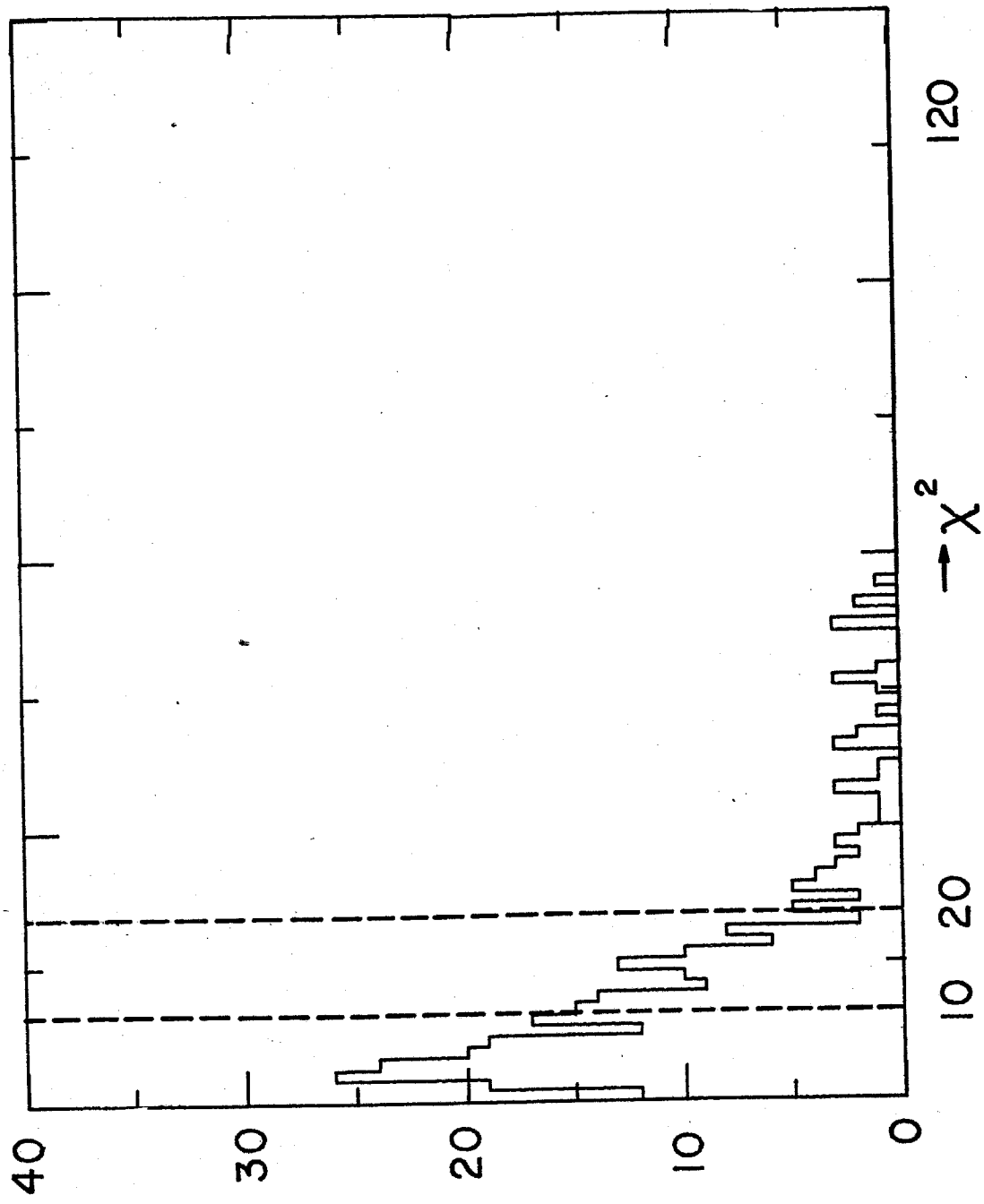

Figure Typical Chi-Square Distribution for 45° cm Data

Beam Energy MeV	Lab Angle of γ-Detector	cm Angle of He^3	Ratio
462	34^o	135^o	.258 ± .014
	44^o	120^o	.140 ± .007
	59^o	105^o	.184 ± .009
	71^o	90^o	.384 ± .023
	86^o	75^o	.657 ± .035
	103^o	60^o	.652 ± .034
	120^o	45^o	1.350 ± .065
377	71^o	90^o	.261 ± .014
571	71^o	90^o	.372 ± .021

Table 4.1 Background Subtraction Ratios. Each term is the ratio of events with $0 < \chi^2 < 20$, using Monte Carlo generated data.

Though a change in the effective thickness could be due to bubbles in the liquid, none were observed when visual checks of the target condition were made. Other indications are that the change was in fact due to a change in the geometry of the target. The thickness of the thin target was measured at liquid nitrogen temperatures subsequent to taking data, and a bulge of about 25% was indeed observed.

Data was taken at one photon counter setting using both the thick and thin target. Using the nominal thickness of the thin target yielded cross sections again about 25% discrepant from the thick target data (the monitors indicated no more than a percent of less fluctuation of the thick target thickness, again born out by a measurement at liquid nitrogen temperatures).

Using data from the monitors, corrections were made to the thin target data on the assumption that the target bulged. The other possibility is that the target was at one point effectively too thin. This, however, is not consistent with the thickness measurement made, or with the discrepancy in the cross sections calculated. Additionally, it is hard to imagine how the target could contract. The pressure of the gas buffer surrounding the target was rigorously the same as the liquid deuterium inside the flask. The only additional source of pressure would be due to the head of liquid leading to the flask. This presumably would produce bulging, if anything.

RESULTS

In this section we present the results obtained from the data analysis discussed in section 4. Seven data points were obtained at an incident proton energy of 462 MeV. This is the peak energy at which Δ production might play an important role. This energy is calculated by assuming that the helium can be considered to be made up of a proton and a spectator deuteron. As we will discuss in more detail later, this is almost certainly not the correct picture. One data point was also obtained for an incident beam energy of 377 MeV, and one for 571 MeV. For purposes of comparison, we also present data, appropriately scaled in beam energy to correspond to this experiment, from a helium-three photodisintegration experiment performed at the now defunct Cal Tech 1.5 GeV electron synchrotron.[5,56] These are the only data available providing a complete angular distribution in the appropriate energy region. The usual reciprocity relations are used to invert these data for comparison with our data. The results are shown in Table 5.1, where numerical values of the differential cross section for the reaction $pd \rightarrow He^3\gamma$ are displayed. The helium center-of-mass angle was computed using the photon lab angle and the beam energy. The errors quoted are statistical. Also, systematic corrections have been applied in particular to the two points for the thin target.

In Figure 5.1 we plot the corresponding angular distribution. On the same plot we show the data[5,56] for the inverse process. Data for the inverse process have been inverted using the detailed balance relationship (cf. equation 4, Introduction), in order to facilitate comparison.

Beam Energy MeV	Target	Photon Lab Angle	Helium cm Angle	$d\sigma/d\Omega$
462	Thin	34^{o}	135^{o}	6.80 ± .54
462	Thin	44^{o}	120^{o}	5.27 ± .60
462	Thick	44^{o}	120^{o}	5.78 ± .51
462	Thick	59^{o}	105^{o}	2.50 ± .17
462	Thick	71^{o}	90^{o}	2.16 ± .12
462	Thick	86^{o}	75^{o}	1.48 ± .10
462	Thick	103^{o}	60^{o}	.77 ± .11
462	Thick	120^{o}	45^{o}	.52 ± .06
377	Thick	71^{o}	90^{o}	2.90 ± .64
571	Thick	71^{o}	90^{o}	1.10 ± .098

TABLE 5.1

Angular Distribution for $pd \rightarrow He^{3}\gamma$ at 462 MeV.

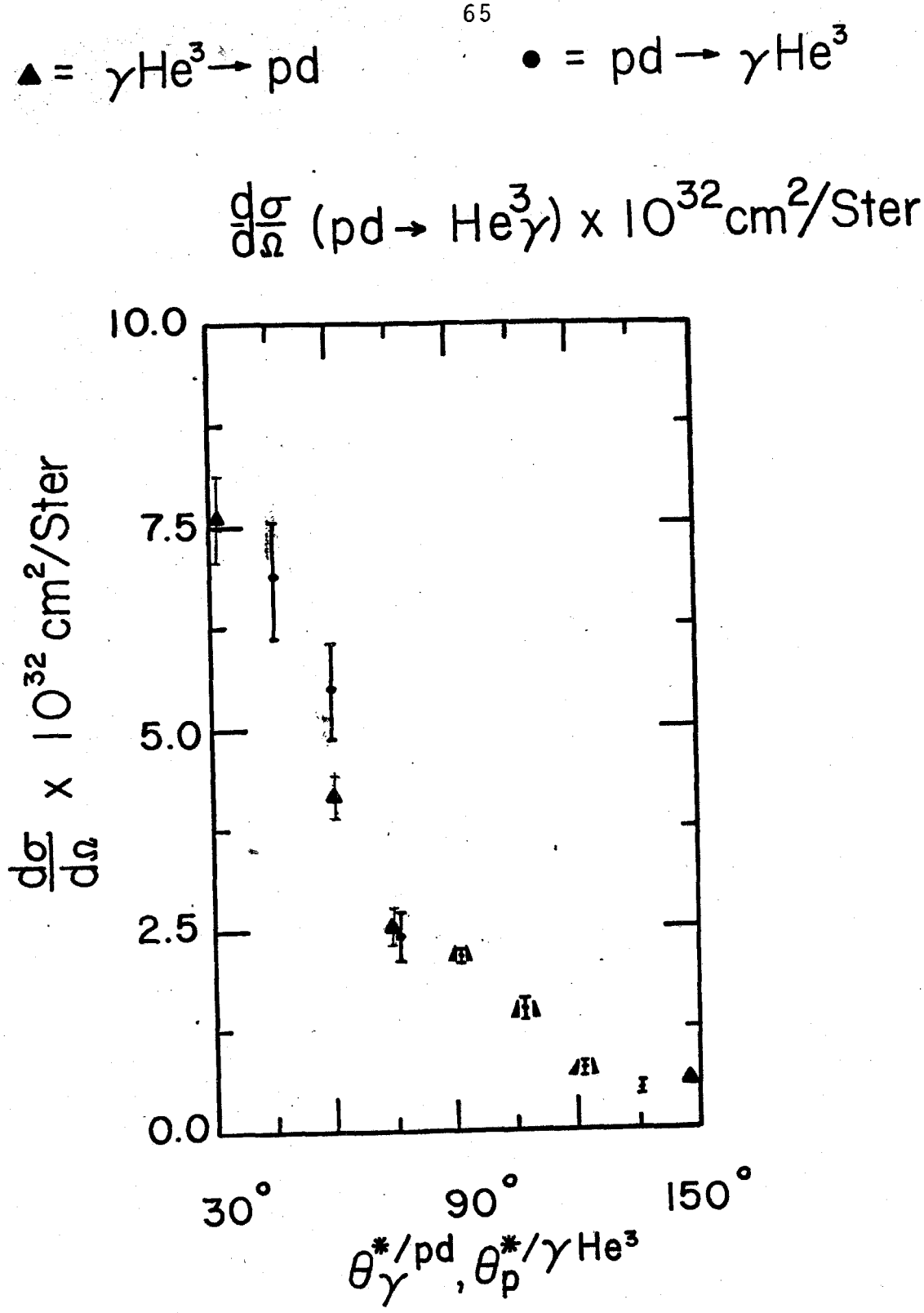

Figure 5.1 Angular Distribution for pd→ $He^3\gamma$, γHe^3 → pd. The latter reaction has been inverted using the detailed balance relationship to facilitate comparison.

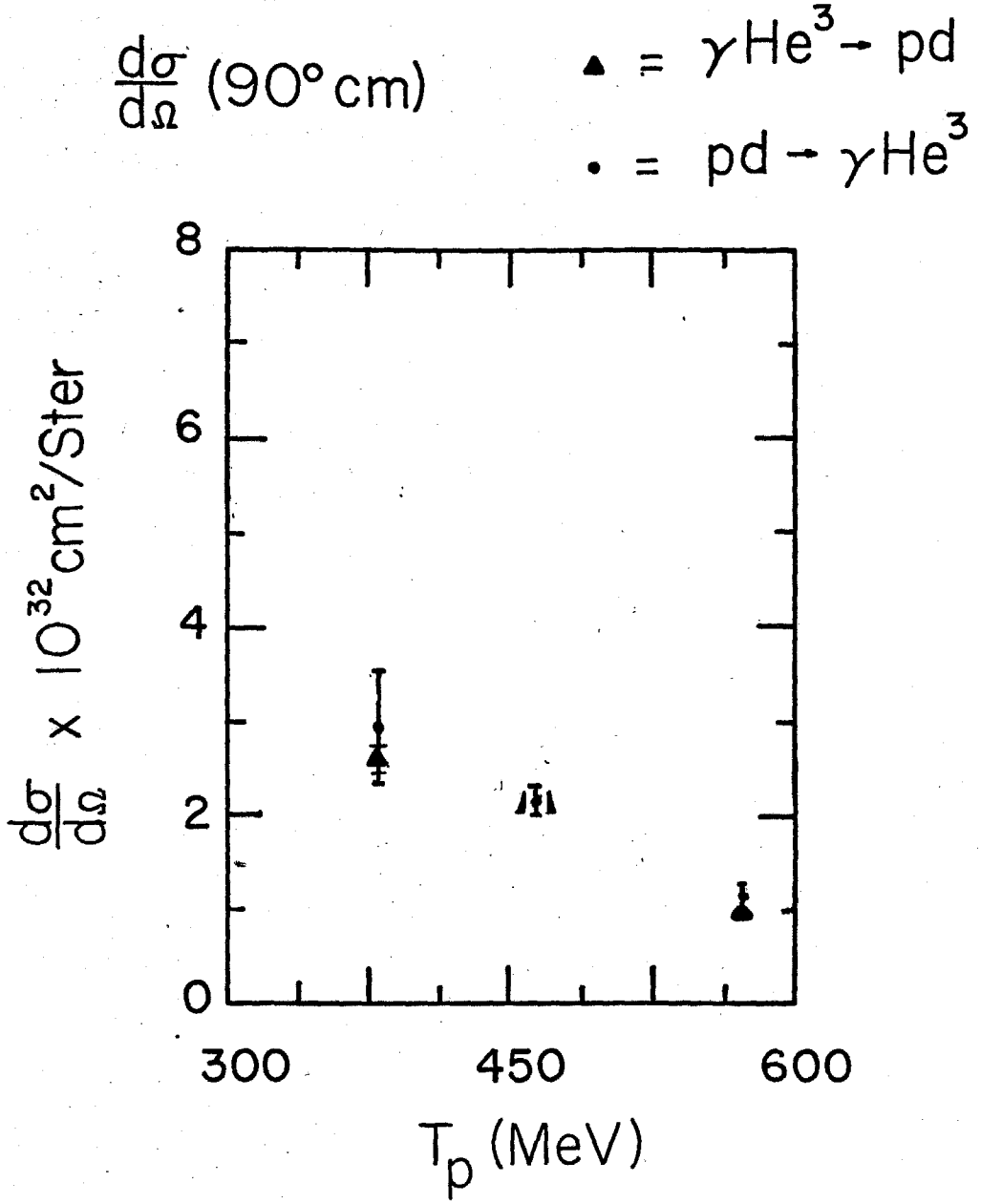

Figure 5.2 Energy Dependence of the 90-Degree cm Data.

Values of the inverted data are displayed in Table 5.2. The center-of-mass angle of the deuteron in the reaction $\gamma He^3 \rightarrow pd$ corresponds to the He^3 center-of-mass angle in the reaction $pd \rightarrow He^3\gamma$. The error bars for the reaction $\gamma He^3 \rightarrow pd$ include statistical errors, spark chamber efficiency errors.

Figure 5.2 shows the energy dependence of the differential cross-section at a center-of-mass angle of 90^o, again compared with data from the inverse process. These data would be expected to show some effect of Δ (1236) production at a proton kinetic energy of $\sim$ 460 MeV, if such isobar excitation plays a significant part in the process studied.

Finally, we give here the results of an analysis of our data with regard to the reaction $pd \rightarrow He^3\pi^o$. While details of this analysis are contained in Appendix L, we include this discussion because this process was the major background, and in fact the only one considered. (The only other possibility is $pd \rightarrow He^3\pi^o\pi^o$, and this is easily ruled out on kinematical grounds.) Also, for some selected energies and angles, we were able to compare our results with previous data for π^o production.[34] This enabled us to check our analysis programs and provided an additional check on the normalization of our data. Figure 5.3 shows the angular distribution for $pd \rightarrow He^3\pi^o$. Figure 5.4 shows the energy dependence of the differential cross section. Values of the cross section are displayed on Table 5.3. A more detailed discussion of the reaction $pd \rightarrow He^3\pi^o$ can be found in another report.[64]

BEAM ENERGY MEV	DEUTERON CM ANGLE	$\frac{d\sigma}{d\Omega} \times 10^{32}$
462	45	.61 ± .12
462	60	.64 ± .15
462	75	1.43 ± .23
462	90	2.16 ± .17
462	105	2.63 ± .35
462	120	4.04 ± .21
462	150	7.63 ± .69
377	90	2.52 ± .20
462	90	2.16 ± .17
576	90	.96 ± .16

TABLE 5.2 He^3 photodisintegration data used to compare with $pd \rightarrow He^3\gamma$ data. The photodisintegration data have been invented to correspond to the reverse reaction by assuming detailed balance is valid.

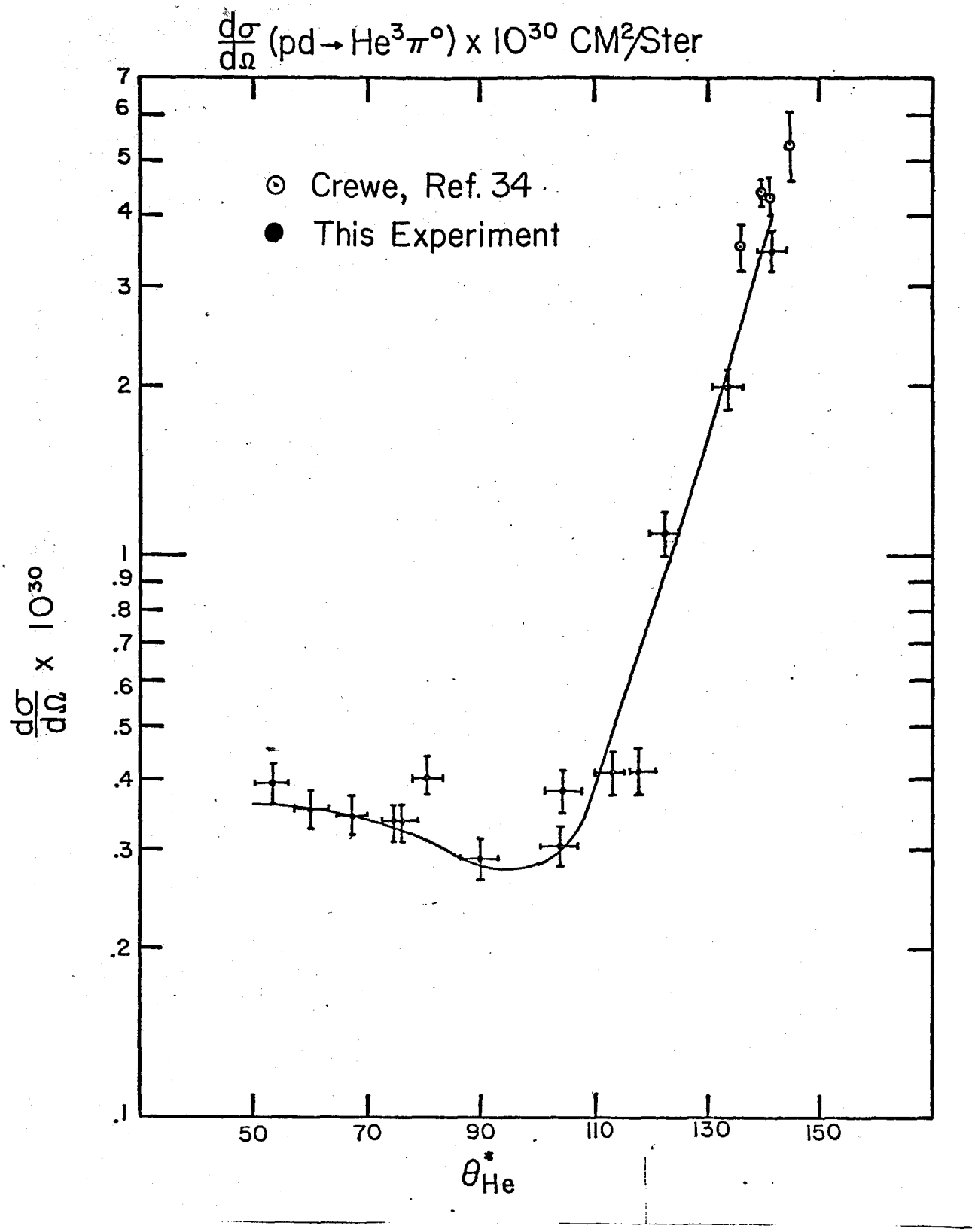

Figure 5.3 Angular Distribution for pd → $He^3\pi^\circ$ at 462 MeV.

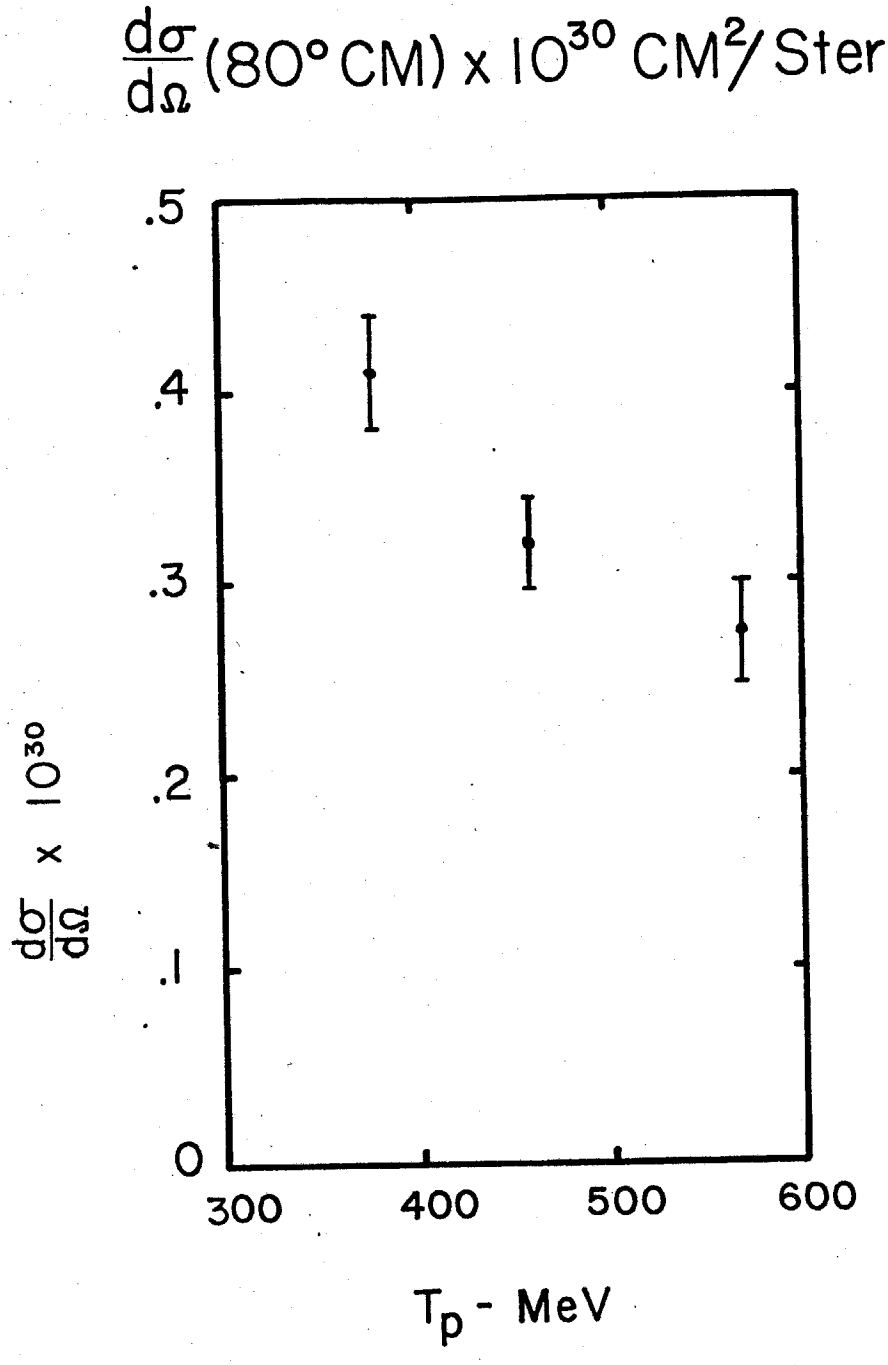

Figure 5.4 Energy Dependence of the Pi-zero Data

BEAM ENERGY MEV	HELIUM CM ANGLE	dσ/dΩ
462	30.0	35.0 ± 2.8
462	40.0	35.0 ± 2.8
462	53.5	39.1 ± 3.2
462	60.5	35.1 ± 4.4
462	67.5	34.2 ± 2.5
462	74.5	33.3 ± 2.7
462	76.0	34.5 ± 1.9
462	80.0	32.0 ± 2.5
462	90.0	28.6 ± 2.9
462	104.5	30.5 ± 3.2
462	105.0	38.0 ± 3.8
462	113.5	40.5 ± 3.6
462	122.5	111.2 ± 7.8
462	131.5	197.5 ± 13.3
462	140.5	344.1 ± 27.0
377	80.0	41.0 ± 3.0
576	80.0	27.5 ± 2.7

TABLE 5.3 Angular distribution for pd → $He^3\pi^o$

DISCUSSION

The following points stand out in the data:

1. There is no discernible enhancement in the 90^{o} data due to $\Delta(1236)$ production.
2. The shape of the angular distribution for the process $pd \rightarrow He^{3}\gamma$ agrees very well with its inverse.
3. The normalization for the reactions $pd \leftrightarrow He^{3}\gamma$ agrees with considerable precision.

McDonald,[5] on the basis of a study of the energy dependence of angular distribution coefficients, had concluded that Δ production is greatly suppressed in the photodisintegration of He^{3}. In particular, the role of the M1 transition in the Δ production mechanism, so important in the process $\gamma d \rightarrow np$, is largely suppressed in the photodisintegration of He^{3}. Our results confirm these conclusions. Note, however, that our argument is compelling only when taken in the context of both our present data and those of the inverse experiment. We note that Δ production also seems to be lacking in the process $\gamma He^{4} \rightarrow pt$,[36] although it is prominent in the reactions $np \leftrightarrow \gamma d$.[50] We also not that an enhancement due to Δ production is supressed in the reaction $pd \rightarrow He^{3}\pi^{o}$[37] (cf. Appendix L), although it is prominent in the reaction $np \rightarrow \pi^{o}d$.[60]

Why is Δ production not observed in the reactions $\gamma He^{3} \leftrightarrow pd$, when it is so evident in the reactions $\gamma d \leftrightarrow np$? Consider the following diagram for the photodisintegration of the deuteron:

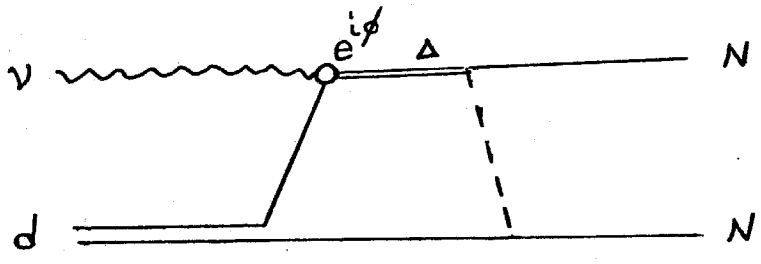

The deuteron is a very loosely bound system, and the breakup process proceeds relatively simply. One nucleon acts almost as a spectator, being required only to absorb a pion from the decay of the intermediate Δ. The exchanged nucleon is on the mass shell, and the reaction proceeds like $\gamma N \rightarrow \Delta$. Thus the energy dependence of the cross section in this process is almost entirely due to the intrinsic width of the Δ.

Now consider a possible diagram for the photodisintegration of He^3:

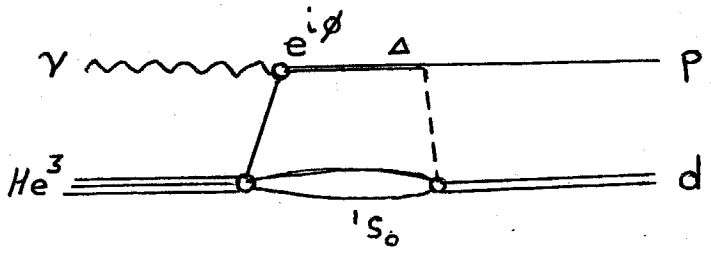

Isospin conservation keeps the intermediate two nucleon state from forming a deuteron.

The most likely two-nucleon state is $^1S_0$. Immediately we see that this configuration does not behave like a proton plus a spectator deuteron. Instead, we have to consider a vertex at which the $^1S_0$ state is formed, with a virtual proton being excited to a Δ by the incoming photon. The virtual nature of the proton obscures the kinematics of Δ production, together with the intermediate energy of the $^1S_0$ scattering length.

Data taken as a function of energy at 90^o center-of-mass angle, shown in Figure 5.2, show no discernible evidence of any enhancement due to Δ production. Similar arguments pertain to the process $pd \rightarrow He^3\pi^o$: in Figure 5.4, the energy dependent cross section for this process is shown, and again one sees no discernible evidence for Δ production.

No matter what the precise diagrams are that are used to explain the qualitative aspects of the data and predict relative magnitudes of various features, this is a new and unique test of time-reversal invariance; it does suggest that models employing the $\gamma N\Delta$ vertex as a source of T-violation may not apply here. A completely different set of amplitudes are called upon in these reactions than those encountered in tests such as $np \leftrightarrow \gamma d$ and $\pi^- p \leftrightarrow \gamma n$.[71]

A unique feature of the present test of T-invariance in the electromagnetic interaction is the parameterless comparison of the absolute normalization of a pair of reactions in a detailed balance test. There is excellent agreement, as best seen is Figure 5.2, with no parameters adjustable to obtain this agreement. This feature alone adds significance to this test of T-invariance by suggesting that changes in the magnitude, rather than the relative phase, of various amplitudes does not occur. Such mechanisms have been mentioned in tests of T-invariance such as $\gamma n \leftrightarrow \pi^- p$, where total cross sections are measured and where from time to time violations have been reported,[53] and later denied.[54]

All tests of time-reversal invariance employing the techique of detailed balance, and in particular those measuring total cross sections, are prone to normalization difficulties. During the course of data taking, considerable care was therefore taken to monitor beam and target conditions on both reaction $pd \rightarrow He^3\gamma$ and $\gamma He^3 \rightarrow pd$, as explained in Appendix N of this thesis.

In summary, we find on the basis of comparisons of both shape and normalization, that our data are consistent with time-reversal invariance in

in the electromagnetic interaction of hadrons. Any discrepancies between the reactions $pd \leftrightarrow He^3\gamma$ may be due to errors in various efficiency calculations, but do not seem to constitute a violation of the size needed to explain the now well established CP violation. Upon performing a point by point comparison of the 462 MeV data, we find an average discrepancy of $.03 \pm .07$, as illustrated in Table 5.4. Similarly, a point by point comparison of the 90° center-of-mass points gives an average discrepancy of $-.09 \pm .10$, as shown in Table 5.5 Within the limits of our errors, we see no evidence for a time reversal violation.

θHe-cm	$X\gamma He^3$	Xpd	$(Xpd - X\gamma He^3)/Xpd$
60	.64 ± .15	.77 ± .11	- .17 ± .24
75	1.43 ± .23	1.48 ± .10	.04 ± .17
90	2.16 ± .17	2.16 ± .12	0.00 ± .10
105	2.63 ± .35	2.50 ± .17	.05 ± .16
120	4.04 ± .21	5.27 ± .60	.23 ± .12
		Average	= .03 ± .07

TABLE 5.4 Comparison of the reaction pd → $He^3\gamma$ at 462 MeV with data from γHe^3 → pd at the same cm energy. The latter reaction was inverted assuming detailed balance is valid.

Proton Energy MeV	$\frac{d\sigma}{d\Omega}/\gamma He^3$	$\frac{d\sigma}{d\Omega}/pd$	$(\frac{d\sigma}{d\Omega}/\gamma He^3 - \frac{d\sigma}{d\Omega}/pd)/\frac{d\sigma}{d\Omega}/pd$
377	2.52 ± .20	2.90 ± .64	-.13 ± .23
462	2.16 ± .17	2.16 ± .12	0. ± .10
576	.956 ± .16	1.10 ± .10	-.13 ± .17
		Average =	-.09 ± .10

TABLE 5.5 Comparison of the 90° center of mass points for the reactions $pd \rightarrow He^3\gamma$, $\gamma He^3 \rightarrow pd$. The arrow indicates an overlapping point. The γHe^3 data was inverted using the detailed balance relationship.

VI. APPENDICES

A. The Beam

1. General Considerations

Good resolution, based on some Monte Carlo studies, of signal from background in the reaction $pd \rightarrow He^3\gamma$ require the proton beam to satisfy the following requirements:

a. A momentum bite of $< 1\%$ for energies from 300 to 600 MeV;

b. An angular divergence of $< .5$ degrees, at the same energies.

Useful counting rates required a flux of no less than 10^8 protons/sec at the liquid deuterium target. Finally, practical consideration dictated that the beam be compatible with another experiment already in progress.

The 184-inch synchrocyclotron at LBL operates at a fixed energy of 735 ± 20^1 MeV energy, for protons. For other energies, a copper degrader was placed in the beam. Table 6.1 illustrates the amount of copper needed for various energies for a proton beam. The point at which the beam emerged from the degrader was taken as the optical source for the subsequent magnetic spectrometer system.

Figure 6.1 shows the main components of the proton beam. Not shown are the thin window helium bags which were added to reduce angular spread from multiple scattering due to the long air path. The long path (about 80 feet) from the copper degrader to the liquid deuterium target was used to produce the desired characteristics of the beam. Dispersive elements were introduced to provide angular and momentum dispersion, and slits were used to define angular and momentum

Tp - Mev	Degrader - inches of Cu
555	4 - 1/2
500	5 - 3/4
454	6 - 13/16
400	8
350	9
303	9 - 15/16

Table 6.1 Amount of Copper Degrader Used in the Proton Beam

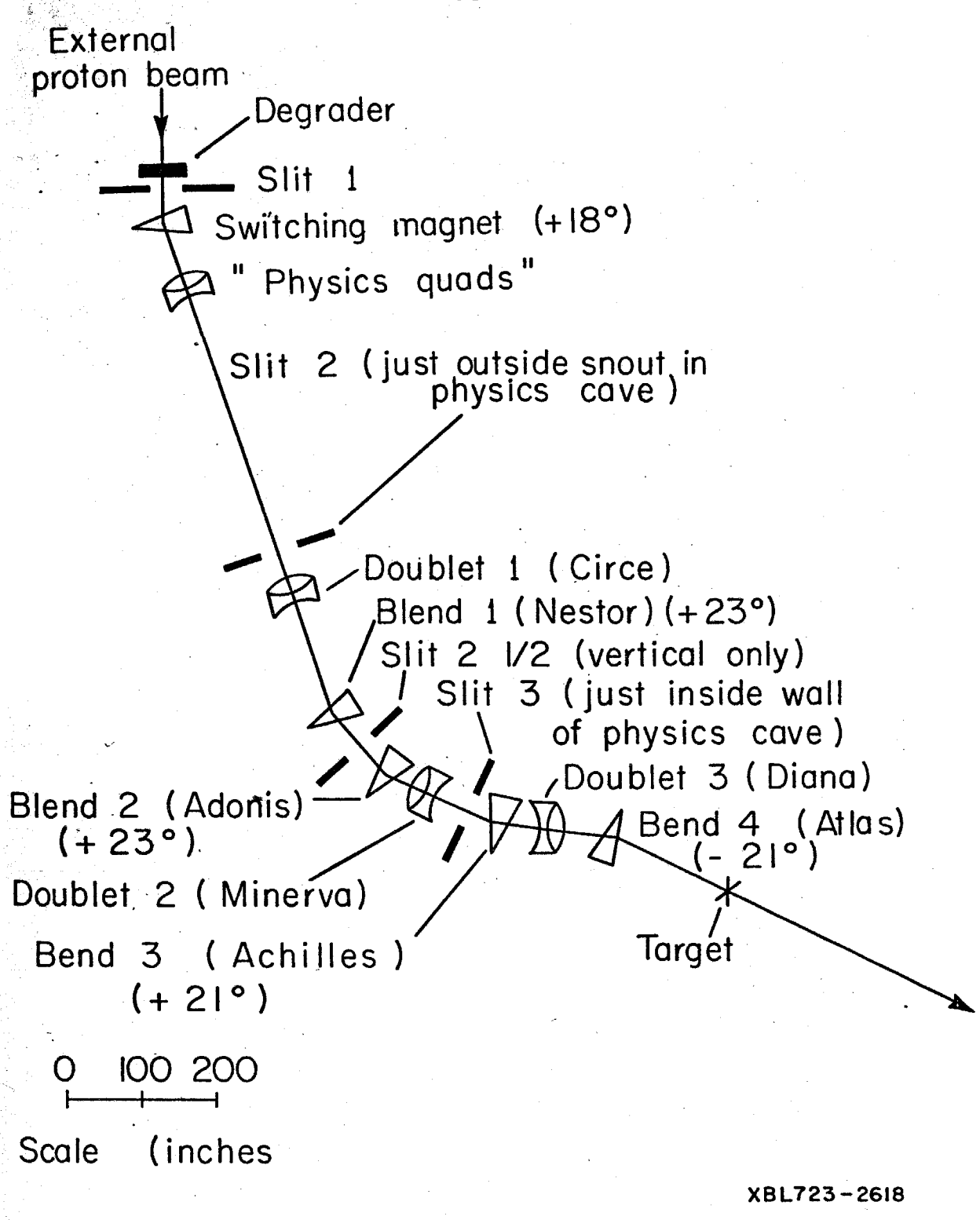

Figure 6.1 Structure of the Proton Beam

acceptance. Following are the main features of the beam. Referring to Fig.6.1,slit 1 determined the effective source size, and slit 2 determined the angular divergence of the beam. Bends 1 and 2 were used to introduce momentum dispersion. The momentum bite of the beam was determined by slit 3. The final quadrapole pair (Diana) produced an image of slit 3 at the target, with a magnification of about 1.8. Tables 6.2 and 6.3 give brief descriptions of the function of each element, for the horizontal and vertical planes respectively.

Starting values for the magnet currents were obtained using both OPTIC[1] and Transport.[2] These programs were also used to investigate the effects of off-momentum particles. Shown in Figures 6.2 and 6.3 are typical ray traces for on-momentum protons, for the horizontal and vertical planes, respectively. Figure 6.4 shows typical ray traces for one percent off-momentum protons.

Tuning up the beam involved use of beam integrators, split ion chambers, counters and an impressive amount of Polaroid film. The direction of the beam could be determined for each element using split ion chambers. (A split ion chamber is an ion chamber with a slot in the middle. The signals from each half are compared differentially. A null condition locates the position of the beam in one dimension.) Pictures were taken liberally to measure the shape of the beam, and compared to the calculated shapes obtained from OPTIC and Transport. The attentuation was measured at various points by using two standard beam integrators. Using the above procedures, slit positions and magnet settings were derived for several beam energies. It was then a straightforward matter to interpolate settings for other beam energies.

Element	Function
Slit 1	Determines the horizontal size of the source.
Switching Magnet	Steers the beam to the center of the physics quads. A small amount of dispersion is incurred.
Physics Quads	These are set to provide parallel to point focusing at slit 2.
Slit 2	This determines the angular acceptance from the source.
Doublet 1 (Circe)	These are set to produce a parallel beam between the subsequent two bends.
Bends 1, 2 (Nester, Adonis)	Both bending in the same direction, these elements provide momentum dispersion.
Doublet 2 (Minerva)	Provides a focus at slit 3.
Slit 3	The dispersion provided by Bends 1, 2 enables the momentum resolution of the beam to be determined by slit 3.
Bends 3, 4 (Achilles, Atlas)	Are used only for bending and steering the beam.
Doublet 3 (Diana)	Provides an image at the target of the dispersed beam at slit 3.

Table 6.2 Function of the Elements of the Proton Beam - Horizontal View

Element	Function
Slit 1	Determines the vertical* size of the source.
Physics Quads	These are set to provide parallel to point focusing at slit 2.
Slit	This determines the vertical angular acceptance from the source.
Doublet 1 (Circe)	Produces a waste between bends 1 and 2, and has some effect on the vertical acceptance of the system.
Slit 2½	This determines the vertical beam size at the target.
Doublets 2, 3	Provide point to point focusing of the beam between slit 2½ and the target.
Slit 3	Used only to clean up the beam.
Slit 3½	Used only to clean up the beam.

* The bending magnets, in principal, have no effect in the vertical plane.

Table 6.3 Function of the Elements of the Proton Beam - Vertical Plane

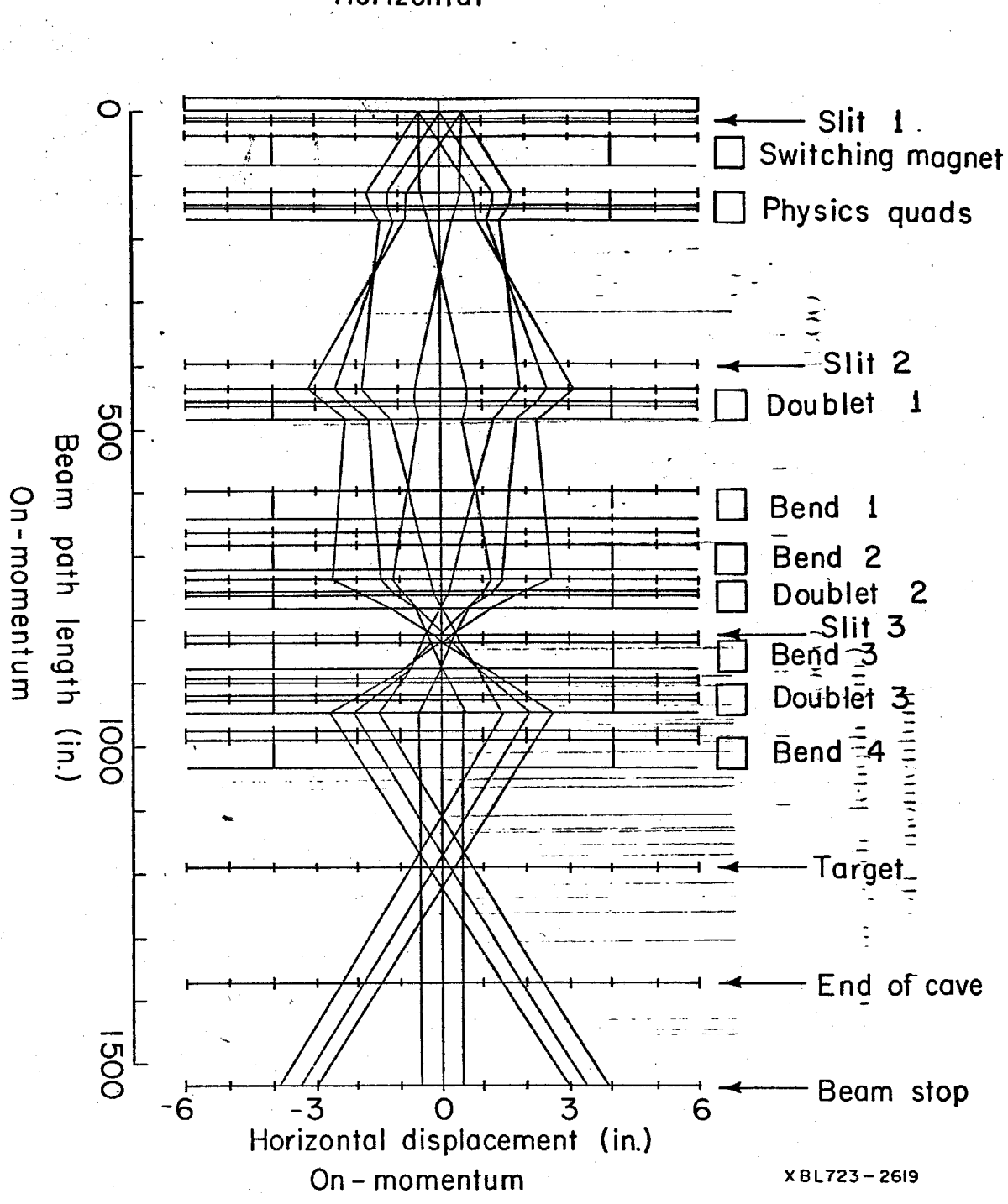

Figure 6.2 Ray Trace for On-Momentum protons - Horizontal View

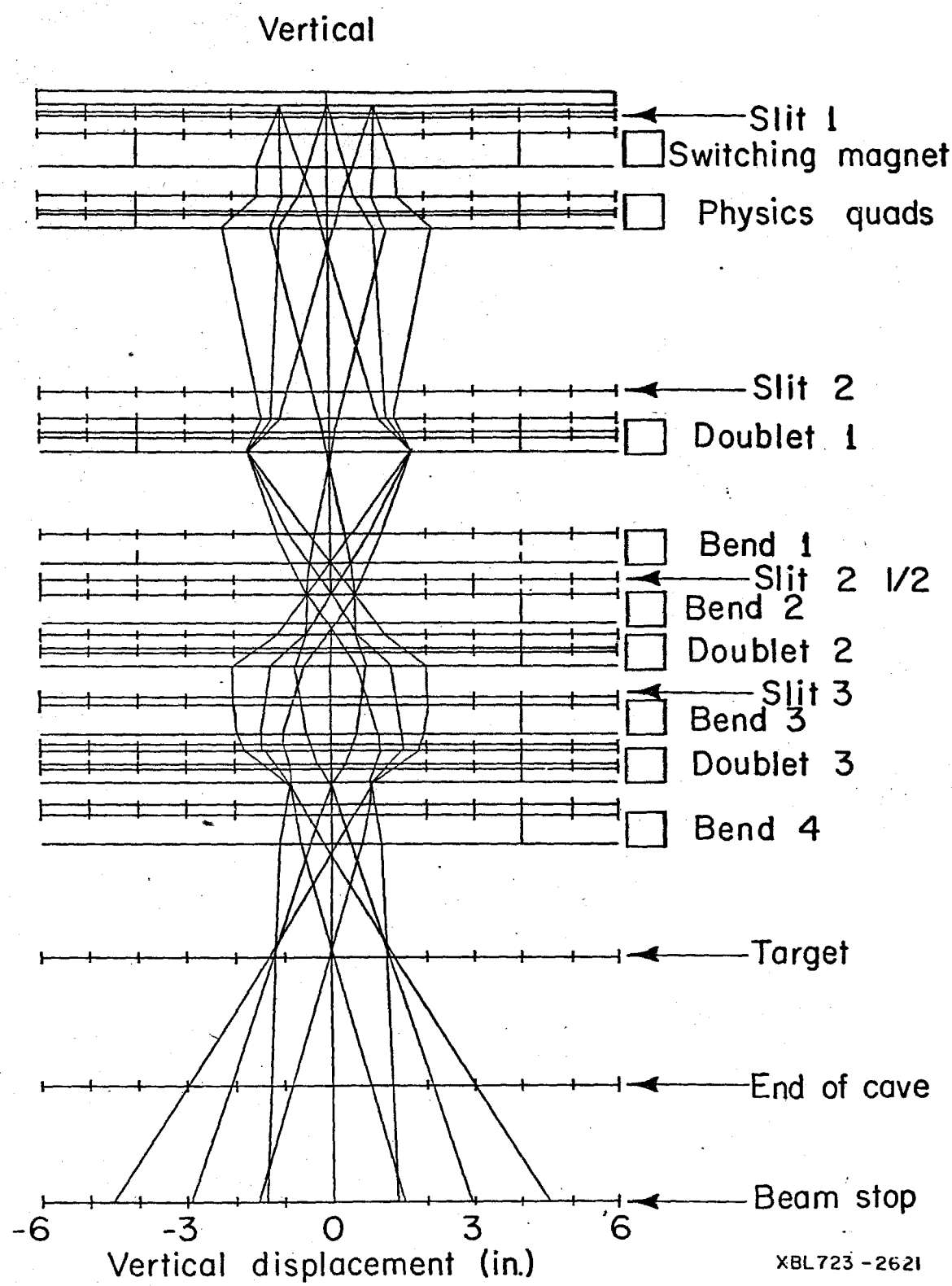

Figure 6.3 Ray Trace for On-Momentum Protons - Vertical View

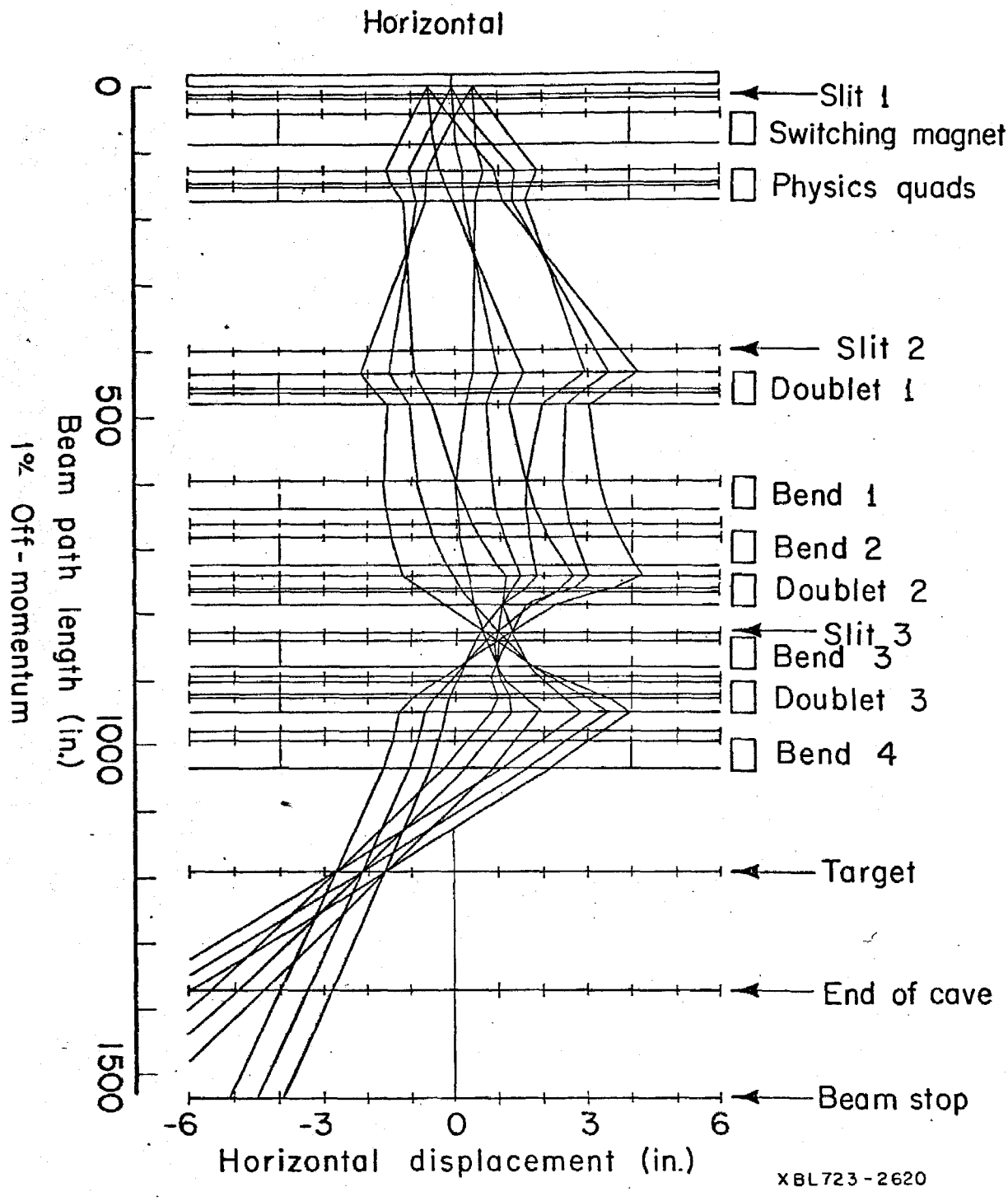

Figure 6.4 Ray Trace for Off-Momentum Protons - Horizontal View

The resulting beam spot size at the target was about two inches in diameter. Pictures taken at the beam stop and at the target showed that the angular divergence was on the order of or less than .5°. The flux at the target for 500 MeV protons was determined to be about 10^8/sec, maximum. Pictures were also taken at various points along the beam line and compared with the beam design. The agreement was generally quite good when one considers that the design employed only first order optics.

The magnet currents were measured using shunts and a potentiometer. The beam energy was measured periodically (see Appendix C) and found to be reproducible to within .3 percent. The magnet currents were re-measured every four hours during the course of the experiment, and were found to be stable to within about .1%.

The cyclotron is capable of accelerating deuterons and alpha particles with no special preparation, since the synchronous frequencies for both are the same, or some harmonic of that for protons. Tritium and Helium-3 beams, however, required some black magic of the kind only the cyclotron crew could provide. Patience and experience enabled them to deftly place delicate tuning devices, for example lead bricks, on the capacitor of the oscillator, thus shifting the frequency enough to produce a useable frequency modulated beam for those runs where particles other than protons were needed. The magnet settings for those runs were derived by taking into consideration the appropriate particle momenta, particle mass to charge ratios, etc.

Helium-four beams were used to produce the reaction $\alpha p \rightarrow He^3 d$. The He^3's were then used to provide further calibration of the thick plastic detector. Details are given in Appendix F.

2. Beam Energy on an Event-by-Event Basis

Several corrections were made on an event-by-event basis in order to remove systematic beam effects. The absolute beam energy was measured using a set of variable thickness copper degraders (cf. Appendix C). The measurements were repeated periodically, and the beam energy for a set of runs was referred to the most recent measurement. The energy was related to the range by the function

$$\begin{aligned} \ln T\,(\text{MeV}) = \; & 3.2273 + .53471\,(\ln R) \\ & + .016216\,(\ln R)^2 - .0036318\,(\ln R)^3 \\ & + .00043731\,(\ln R)^4 \end{aligned}$$

where R is the range in copper in gm/cm^2.

Using the above energies, the value of the energy corresponding to the actual magnet currents observed during a run was computed using:

$$T_{corr} = T_{meas}\left(1 + 0.46 \left| \frac{P\,dT}{T\,dP} \right| \Delta i/_i \right)$$

Table 6.4 indicates the values of T_{corr} for various run intervals, and also the dispersion ratio, $\left| \frac{P\,dT}{T\,dP} \right|$.

T_{corr} is the beam energy at the center of the target. To this we subtracts .24 MeV when the thick (1/2 in.) target was employed, .08 MeV when the thin (1/6 in.) target was used.

BEAM ENERGY DATA

Run Interval	Beam Energy	Dispersion Ratio
202 - 203	462.710	1.670
205 - 206	466.073	1.668
207 - 215	466.214	1.668
220 - 224	462.537	1.670
225 - 228	461.468	1.670
231 - 235	462.250	1.670
236 - 241	462.389	1.670
242 - 244	460.450	1.671
245 - 258	460.838	1.671
259 - 266	467.140	1.668
267 - 269	467.724	1.667
270 - 291	463.632	1.669
293 - 294	380.122	1.712
295 - 303	576.385	1.619
304 - 307	379.824	1.712
322 - 322	558.516	1.627
323 - 327'	0.000	1.670
328 - 331	462.105	1.670
332 - 367	461.390	1.670

BEAM WIDTH - IN PERCENT

Run Interval	Beam Width
202 - 215	.590
220 - 224	.470
225 - 235	.490
236 - 244	.440
245 - 258	.540
259 - 291	.490
293 - 294	.510
295 - 303	.420
304 - 307	.510
308 - 375	.520

Table 6.4 Beam Energy and Beam Width for all Runs

Using the event origin, computed using the intersection of the helium trajectory with the target midplane, the energy, corrected for a systematic horizontal dispersion, is computed using

$$T_{event} = T_{corr} \left[1 + .004 \left| \frac{P\, dT}{T\, dP} \right| (Y - Y_o)\right]$$

where Y_o is the mean position of the event origins, Y the position of the event origin.

3. Angular Divergence on an Event-by-Event Basis

A correction to the beam direction was made using data from the beam design. The corrections were

$$\theta_y = \langle \theta \rangle_y + .5\,(Y - Y_o)$$

$$\theta_z = \langle \theta \rangle_z + .4\,(Z - Z_o)$$

where θ_y, θ_z are in degrees, $\langle \theta \rangle$ is the average divergence at the target center.

B. TARGET MONITOR

1. Overview

A set of range telescopes was constructed to measure pd elastic scattering rates at the same time that pd $\rightarrow He^3$ γ data were being collected. The position of these telescopes is shown in Figure 2.1. The rates were used as a check on the deuterium density in the target, as well as the liquid level in the target flask.

At one point a set of three counters was placed directly in the proton beam, which was then run at low intensity. Coincidences were taken between the three counters, and the rates compared with the rates for the telescopes. This established a ratio between telescope rates and beam intensity.

The telescopes were surveyed into a kinematic setting for pd elastic scattering that was kinematically unavailable to pp elastic scattering, (see Fig. 6.5) the biggest possible source of background. Once in place, the telescopes were seldom moved. Surveys were made periodically to check their positions.

2. Design and Construction

Figure 6.6 illustrates schematically the construction of the two telescopes and their positions relative to the beam at 462 MeV. Each telescope was mounted on a "uni-strut" stand at target level.

Considerations which went into the design of the telescopes include:

a. Differences in energy acceptance over the angular acceptance of the telescopes.

b. Range straggling.

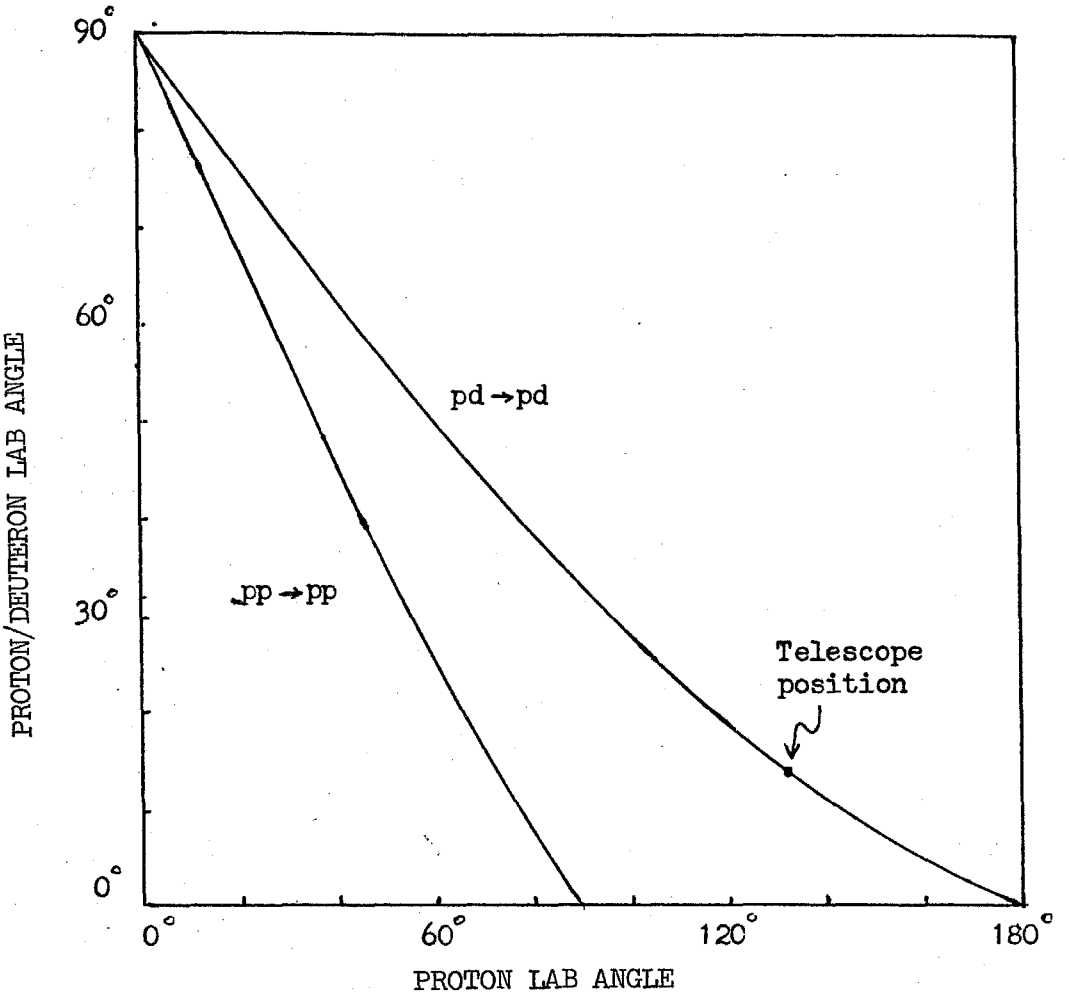

Figure 6.5 Kinematic Position of the Target Monitor Telescopes

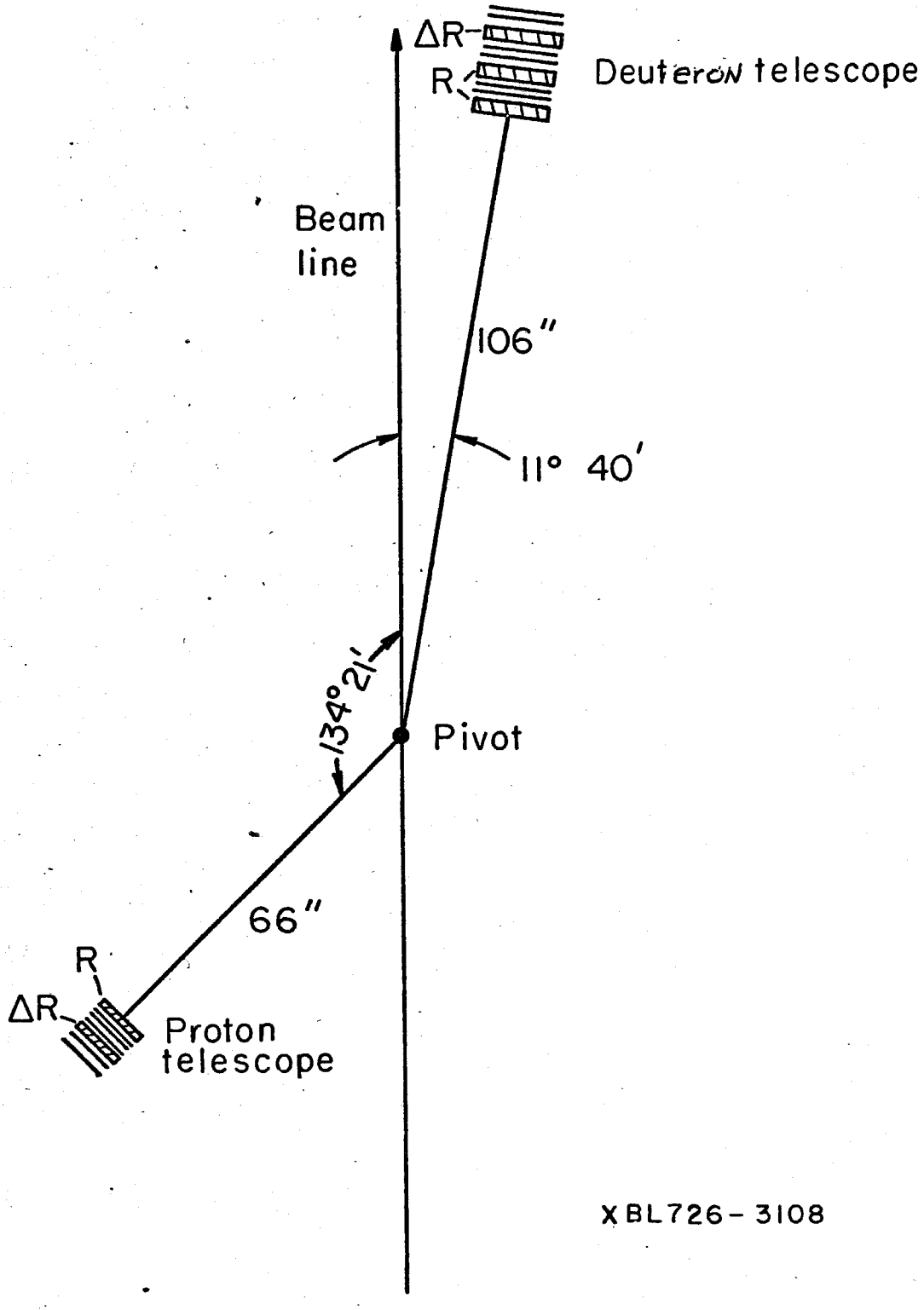

Figure 6.6 Schematic View of the Target Monitor Telescopes

c. Energy losses of the p and d in the target.

d. Scintillator thickness and energy loss.

e. Multiple scattering.

f. Changes in beam energy.

In addition, an overall countion factor was included in order to make the design quite conservative. Table 6.5 shows some typical values of degrader thickness. Refer to Fig. 6.6 for the meaning of R, ΔR.

Shown in Fig. 6.5 are the kinematics for both pd and pp elastic scattering. Indicated on the pd curve is the position of the proton and deuteron telescopes. This position eliminates most of the pp scattering, still leaving the proton in pd elastic scattering with a useful energy.

Copper was used for all of the absorbers. The copper absorber was slightly larger than the active area of the counters to compensate for the effects of multiple scattering. The counters were all one-eighth inch thick.

3. Electronics

Shown in Fig. 6.7 is the logic used in the telescopes. For increased efficiency, two counters were used everywhere and the signals added resistively.

Majority logic was used with the three counters in the proton telescope. The proton energy was sometimes very low for low beam energies, and quite possibly the three counters would be too thick for the proton to completely penetrate. Thus two counters out of three were

Table 6.5

Degrader Thickness - gm/cm^2

Beam	Protons		Deuterons	
	R	ΔR	R	ΔR
462 MeV	.94	1.55	40.4	15.8
571 MeV	2.15	2.23	68.0	25.5

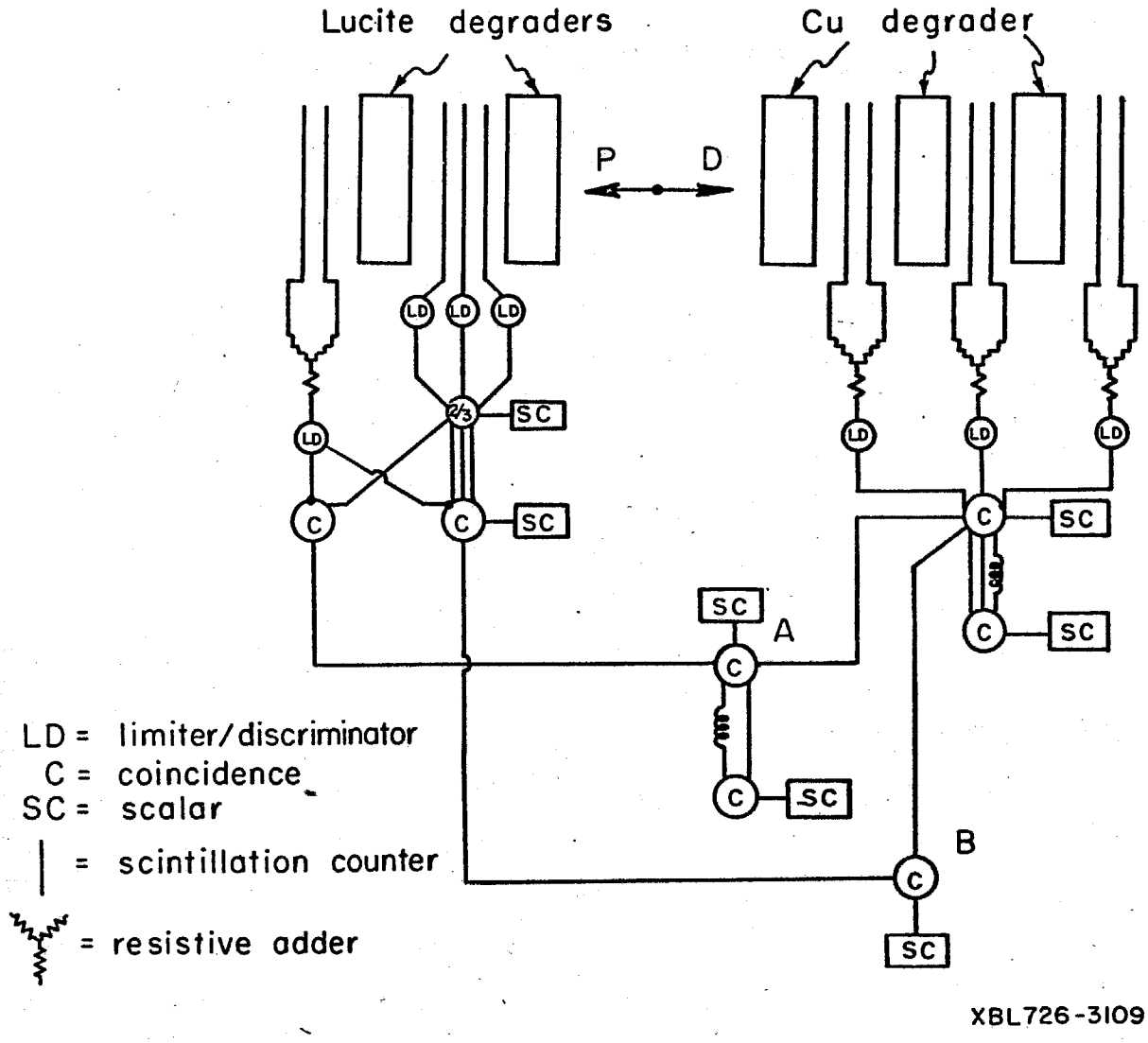

Figure 6.7 Target Monitor Logic Electronics

also accepted.

The coincidence labeled "A" is the master coincidence, and gives the pd elastic scattering rate. Another coincidence circuit, with one signal delayed, measured a random rate. The randoms rate was also measured for the deuteron telescope, since it was close to the beam.

Finally, coincidences between the deuteron telescope, and the triple coincidence rate for the proton telescope were collected at "B". If the absorber thicknesses were correct the ratio of A/B should be 1.

4. Uses

As mentioned, once the monitors were surveyed in place, and the correct amount of absorber put in place, the monitors were not moved while collecting data at a given energy. We collected pd $\rightarrow$ $He^3\gamma$ data at three energies, 377, 462, 576 MeV, finishing all data collecting at a given energy before proceeding to the next.

The telescope's function, while collecting data, was to monitor the deuterium density in the target flask. Periodically the telescopes were moved to a position favorable for pp elastic scattering in order to perform an ion chamber calibration. Three direct beam counters were placed in a low intensity beam (about 10^5 protons/sec), and the rates for triple coincidences in these three counters compared to the coincidence rate in the two telescopes. This established a ratio of beam flux to telescope rates. The procedure was to then increase the beam flux to the level used while collecting data, and, with this known beam, calibrate the ion chambers.

C. BEAM ENERGY AND STABILITY

Range-energy measurements were used to measure the absolute energy, and as a check on the stability, as a function of time, of the degraded particle spectrometer. These measurements were made each time the spectrometer was turned on after the magnets had stabilized, and occasionally between runs.

The method of measurement is based on measuring the relative ionization versus range, using a standard absorber (in this instance copper). Plotting the ratio of the current readings from two ionization chambers versus absorber thickness, one obtains a Bragg curve, as illustrated in Fig. 6.8. The Bragg curve contains the effects of range straggling and beam momentum dispersion, so one must obtain from this curve the mean range.

A prescription for obtaining the mean range, independent of the beam momentum dispersion, is described by Mether and Segrè[3]. Let R* be the mean range, and assume that the distribution of ranges due to straggling has a Gaussian form of probability:

$$P(R) = (2\pi)^{-\frac{1}{2}} \sigma^{-1} \exp\left(-(R-R^*)^2\right)/2\sigma^2$$

Let i(t) be the ionization per centimeter in the gas inside of the chamber for a particle at a distance t for the end of its range in the absorbing material (copper). The measured ionization in the ion chamber will then be of the form $I(R) = K\int_0^\infty \exp\left(-(X-R^*)^2 2_o{}^2\right) i(X-R)dX$, where t = X-R, K is a constant. Defining a new set of dimensionless variables $t' = t/\sigma$, $X' = (R-R^*)/\sigma$, this can be put in the form

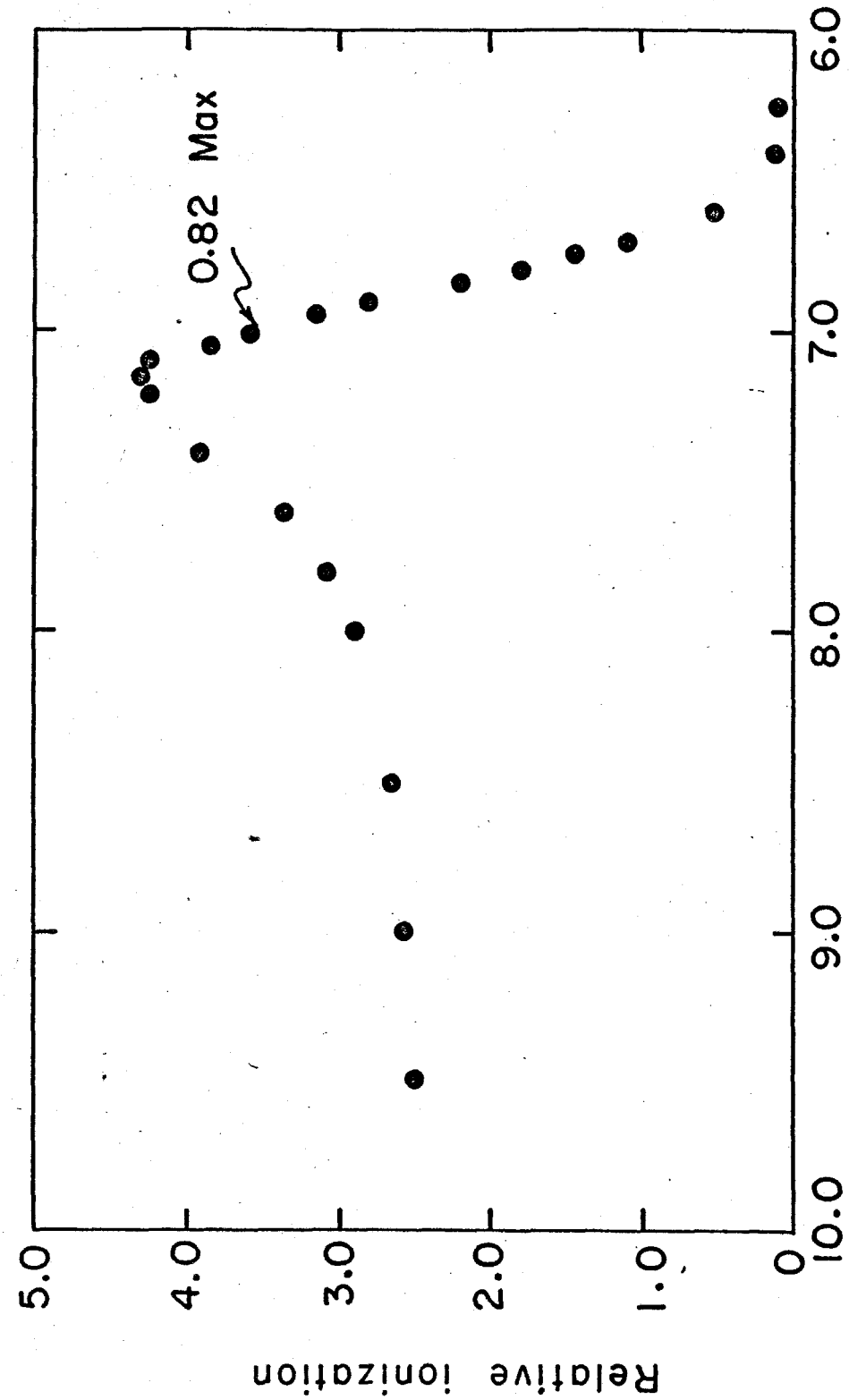

Figure 6.8 Typical Bragg Peak Obtained from a Range Measurement

$$I = K\int_0^\infty \exp(X' + t'')i'(t')dt'.$$

Mether and Segrè state that $i'(t')$ is accurately represented by the form

$$i' = (\text{const})t'^{-.46} \quad \text{then } I = K\int_0^\infty \exp(X' + t')t'^{-.46}\,dt'.$$

The results of a numerical integration of the quantity

$$f(X) = \int_0^\infty \exp(X' + t')t'^{-.46}\,dt',$$

normalized to one at the peak, are shown in Fig. 6.9 . The range is taken to be $X' = 0 = R-R^*$, independent of any beam dispersion. This occurs at .82 of the maximum of the Bragg peak, and is the value used in all of our measurements, as illustrated in Figure 6.11.

The apparatus is shown schematically in Fig. 6.10. It consists of two ion chambers, and a variable thickness of copper absorber. The variable thickness of degrader was measured by a precision potentiometer. The potentiometer was used to measure the position of the movable wedge.

Figure 6.8 illustrates a typical plot of specific relative ionization versus potentiometer setting. The value of the potentiometer setting at .82 times the peak of the relative ionization curve is indicated. The absolute energy was determined using data from the range-energy tables compiled by Janni[4].

Figure 6.9 Numerical Integration Results

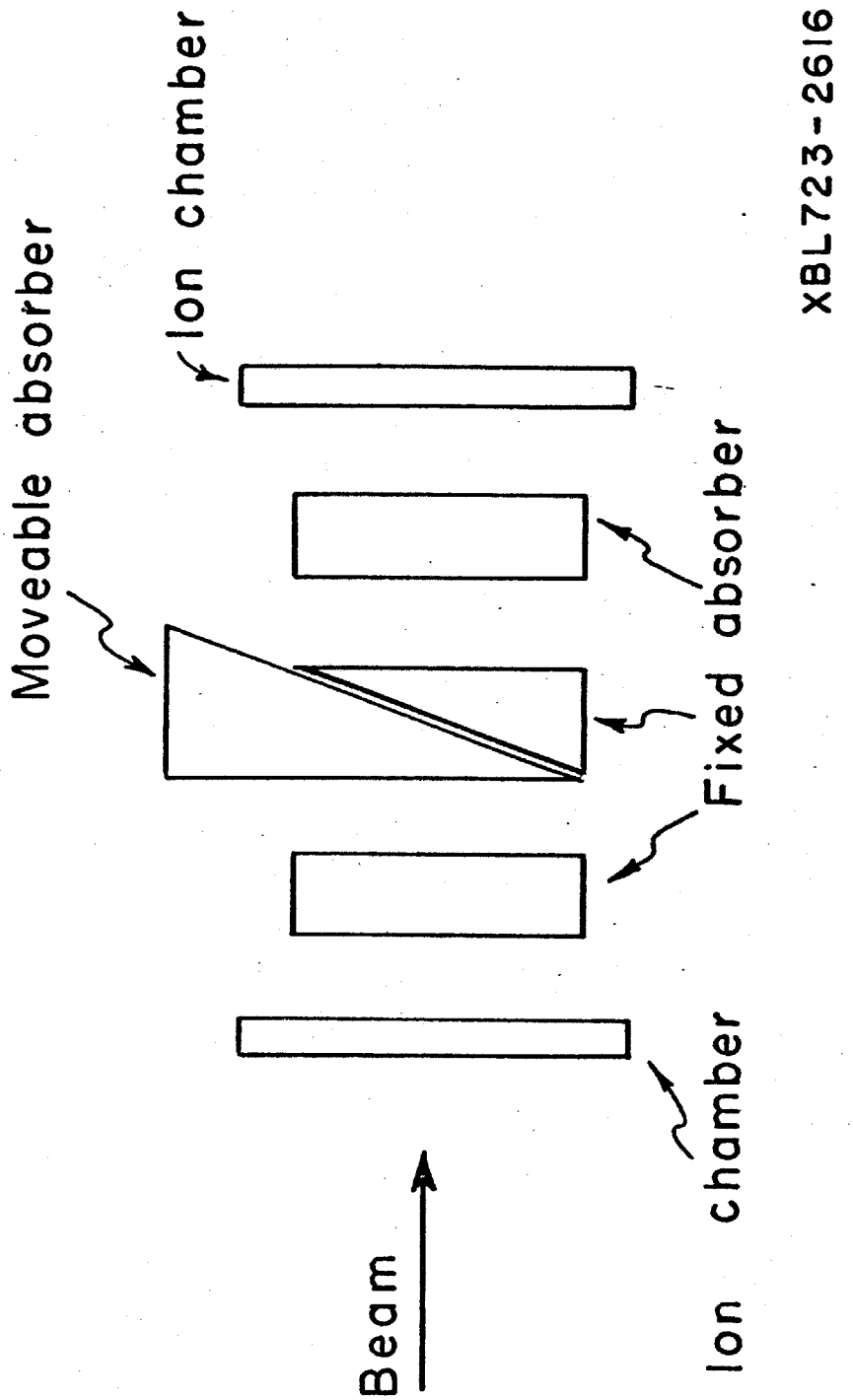

Figure 6.10 Range Measuring Apparatus

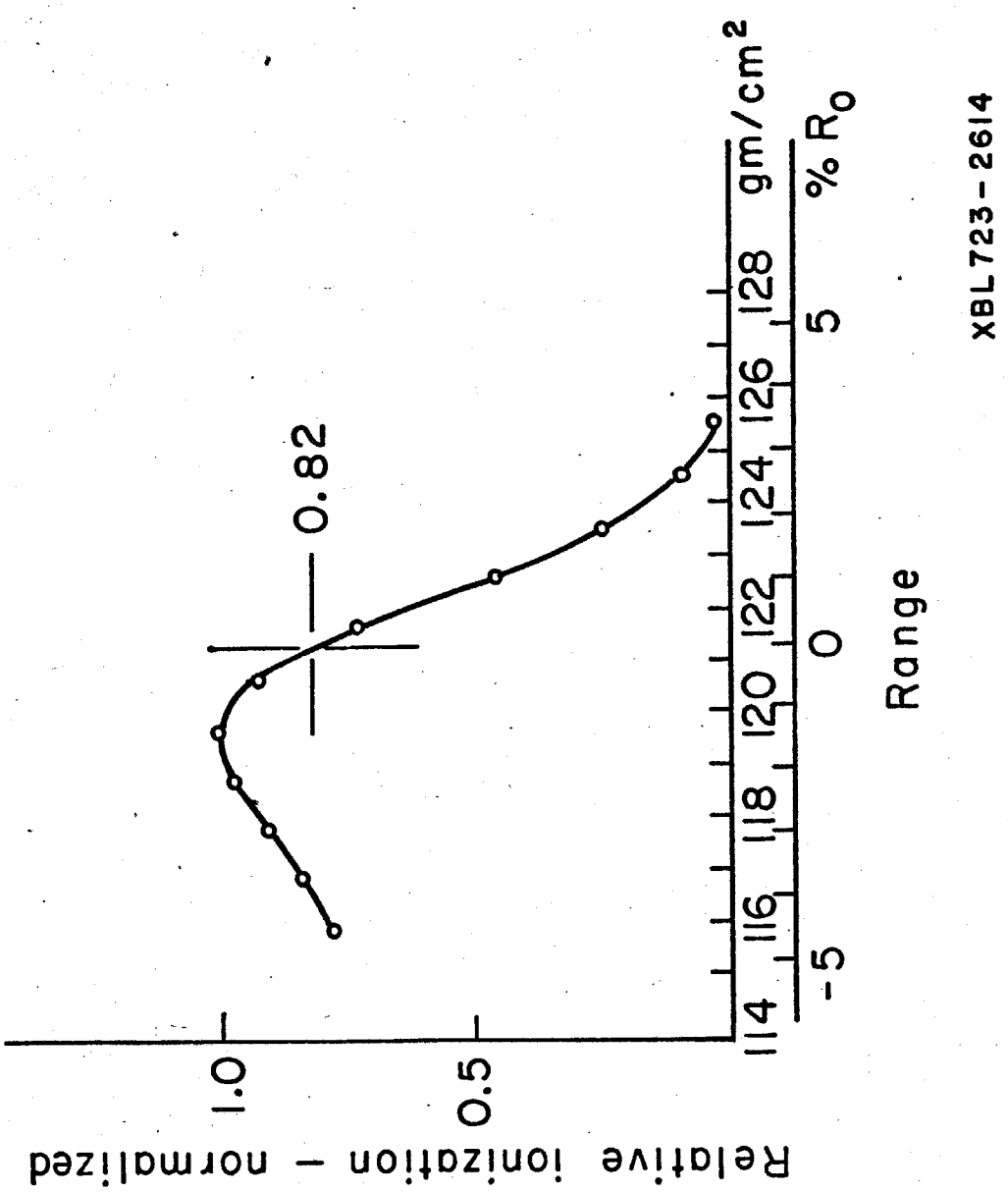

Figure 6.11 Relative Ionization Versus Range with Mean Range Noted

D. PHOTON COUNTERS

We now discuss the photon hodoscope/spectrometer which was designed to have optimal performance in the energy region between .15 and .7 GeV. Two counters were actually used during the experiment after a decision was made to increase the geometric detection efficiency of the apparatus because of the very low cross section for the process $pd \rightarrow He^3\gamma$. The two counters differed substantially in design and performance, one being designed and constructed specifically for this experiment, the other being an adaptation of an existing counter. Only the new design will be described in detail. Discussions of the design and performance of the other can be found in the references[7,8,9].

In general, the counter should specify as completely as possible the four vector of the photon, with high efficiency and good time resolution. Specifically, it should provide:

1. Good energy resolution, to help separate the process $pd \rightarrow He^3\gamma$ from the process $pd \rightarrow He^3\pi^o$, $\pi^o \rightarrow \gamma\gamma$.
2. Good spatial location of the photon, in order to enable one to impose angle and coplanarity constraints.
3. Provide the highest possible detection efficiency consistent with good spatial resolution.

1. Construction

Figure 6.12 is a schematic representation of the basic components of the detector. The total length of the absorber is $10X^o$ consisting of a $2X^o$ converter, and a main radiator of $8X^o$ thickness. Inserted between the converter and the main radiator were a thin trigger counter and four wire spark chambers. The wire chambers were used to

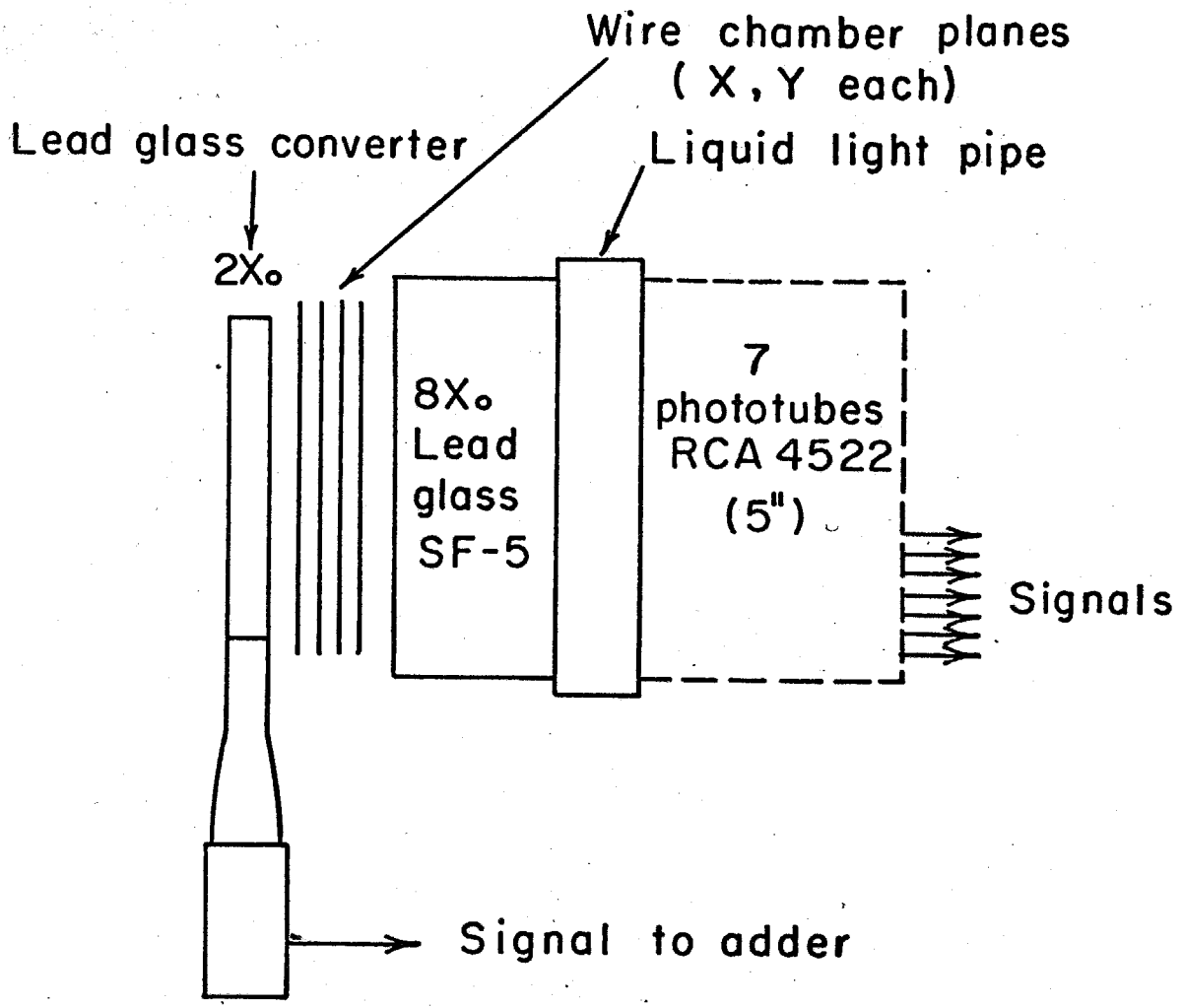

Figure 6.12 Basic Components of the Photon Detector

delineate charged particle tracks, which were then used to localize the small fiducial volume in which the photon conversion took place. A thin veto counter was placed in front of the converter which served to suppress charged background triggers.

In order to obtain maximum energy resolution, the optical coupling between the radiators and the phototubes was optimized. The converter/radiator was joined by a folded light pipe to a fast 5-inch phototube, of high quantum efficiency[10]. The main radiator was viewed from the back by seven 5-inch phototubes. The optical coupling was made by a light pipe consisting of a set of interlacing hexagonal cones, as shown in Fig. 6.13A. The cones consisted of polished aluminum set in epoxy. The phototubes and main radiator were joined to the light pipe with an adhesive sealant (RTV). The light pipe was then filled with a clear mineral oil[11] with an index of refraction equal to the geometric mean of the indices of the glass of the phototube face and the lead glass block. Figure 6.13B shows the main block assembly before it was encased in a 1/4-inch iron box.

2. Counter Calibrations

The counter was calibrated in the parasitic electron beam available at the Caltech synchrotron. The beam was obtained from the back side of a quantameter, and emerged through a small hole in the shielding wall. Also used was a magnet/counter setup which provided tagged photons. The test setup is illustrated in Fig. 6.14. The energy resolution of this setup was, unfortunately, only on the order of $\Delta p/p \cong 3\%$[6,17]. This was one of the largest uncertainties in determining the energy resolution of the detector. Figure 6.15 shows the

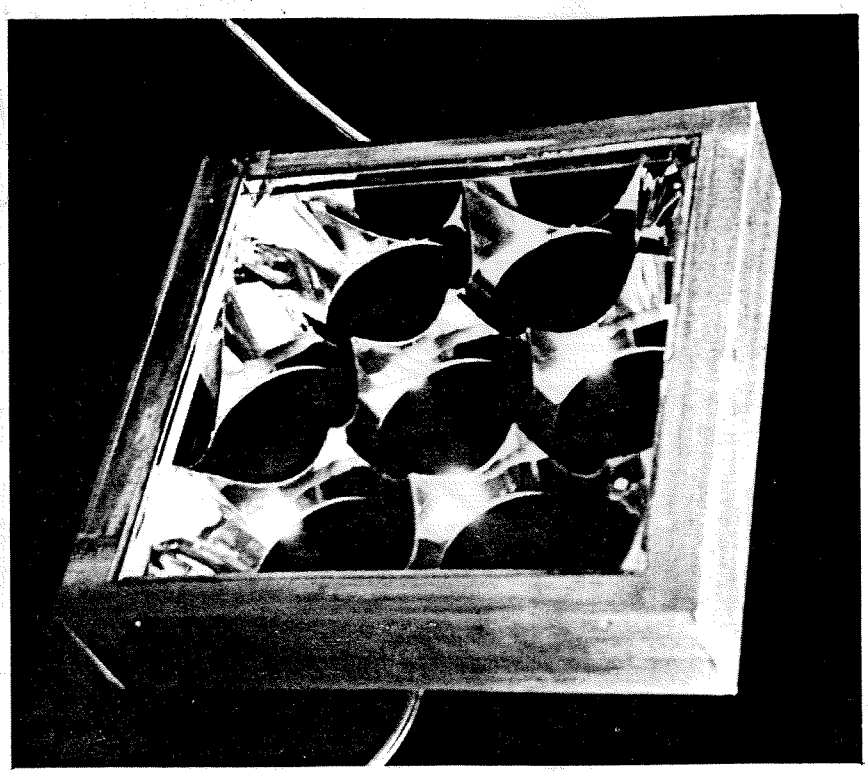

FIGURE 6.13 A

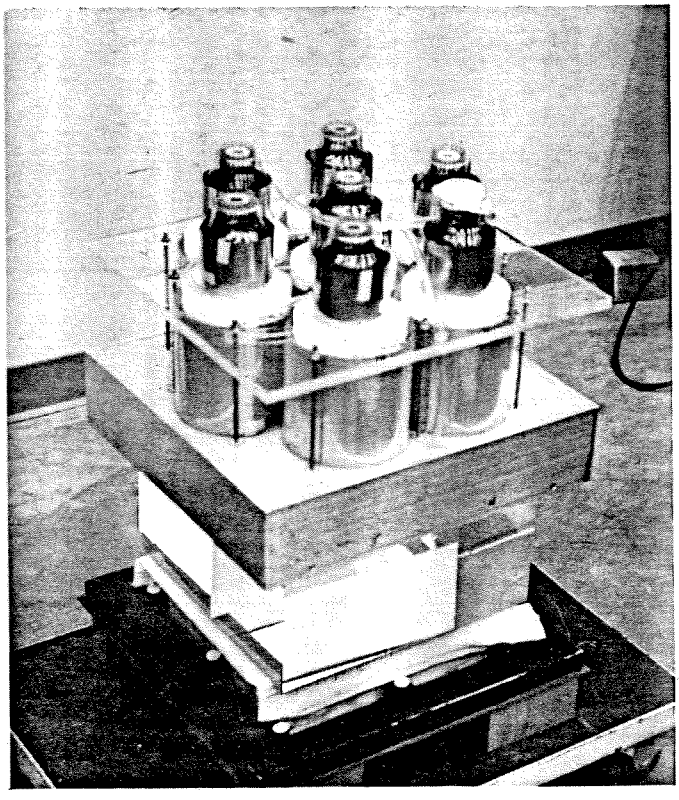

FIGURE 6.13 B

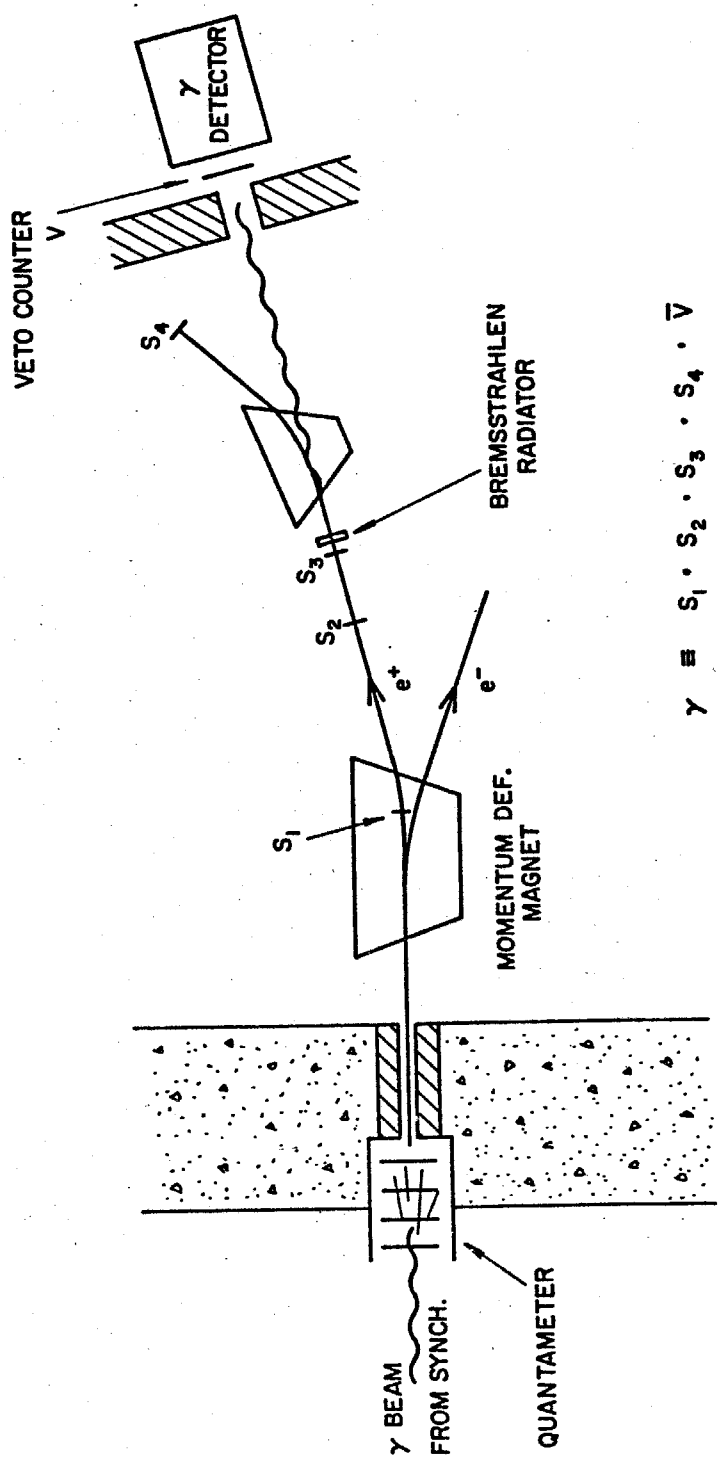

Figure 6.14 Tagged Photon Beam Experimental Setup

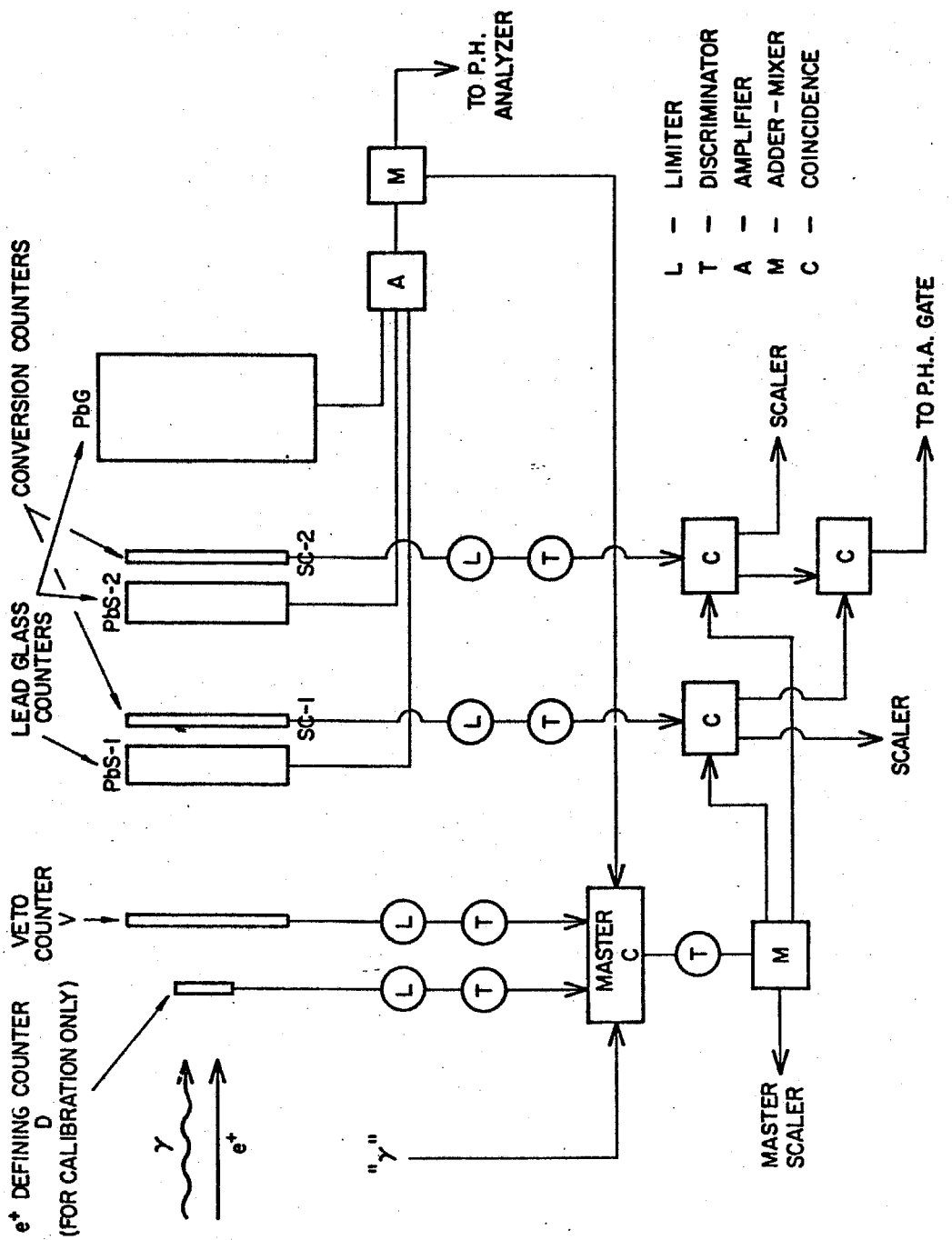

Figure 6.15 Photon Detector Logic Electronics

electronics used in conducting the calibrations. While the conversion efficiency of the converter/radiator was being determined, a veto counter was positioned in front of the converter.

Because they were far more copious, positrons were used rather than tagged photons. As S. J. Yellin has pointed out[8], the calibration is independent of whether one uses electrons, positrons, or photons. Basically, the energy resolution depends on the total amount of Cherenkov light available. This, in turn, depends to a great extent on the total path length of the charged particles in the shower[6], since all the charged particles are electrons or positrons with $\beta \sim 1$ for high energy incident particles. By actual measurement, the total path length is not sensitive to the kind of incident particle, as long as its energy is high ("high" is about 70 MeV for lead[12]).

3. Energy Resolution

The counter was tested in three basic configurations:

a. Two converter/radiator, each $2X^6$ thick, and the $8X^\circ$ block.

b. One converter radiator of thickness $2X^\circ$, and the main block.

c. The main block alone.

In each configuration, the outputs from each section were added. The gains of the tubes were then adjusted for each section to optimize the resolution of the counter, for one energy. Then a calibration was done over an energy interval of 150 to 600 MeV. For configuration (3), the block had to be rotated 90° in order to contain the whole shower at all energies.

Figure 6.16 shows the linearity for configuration (1). It was inter-

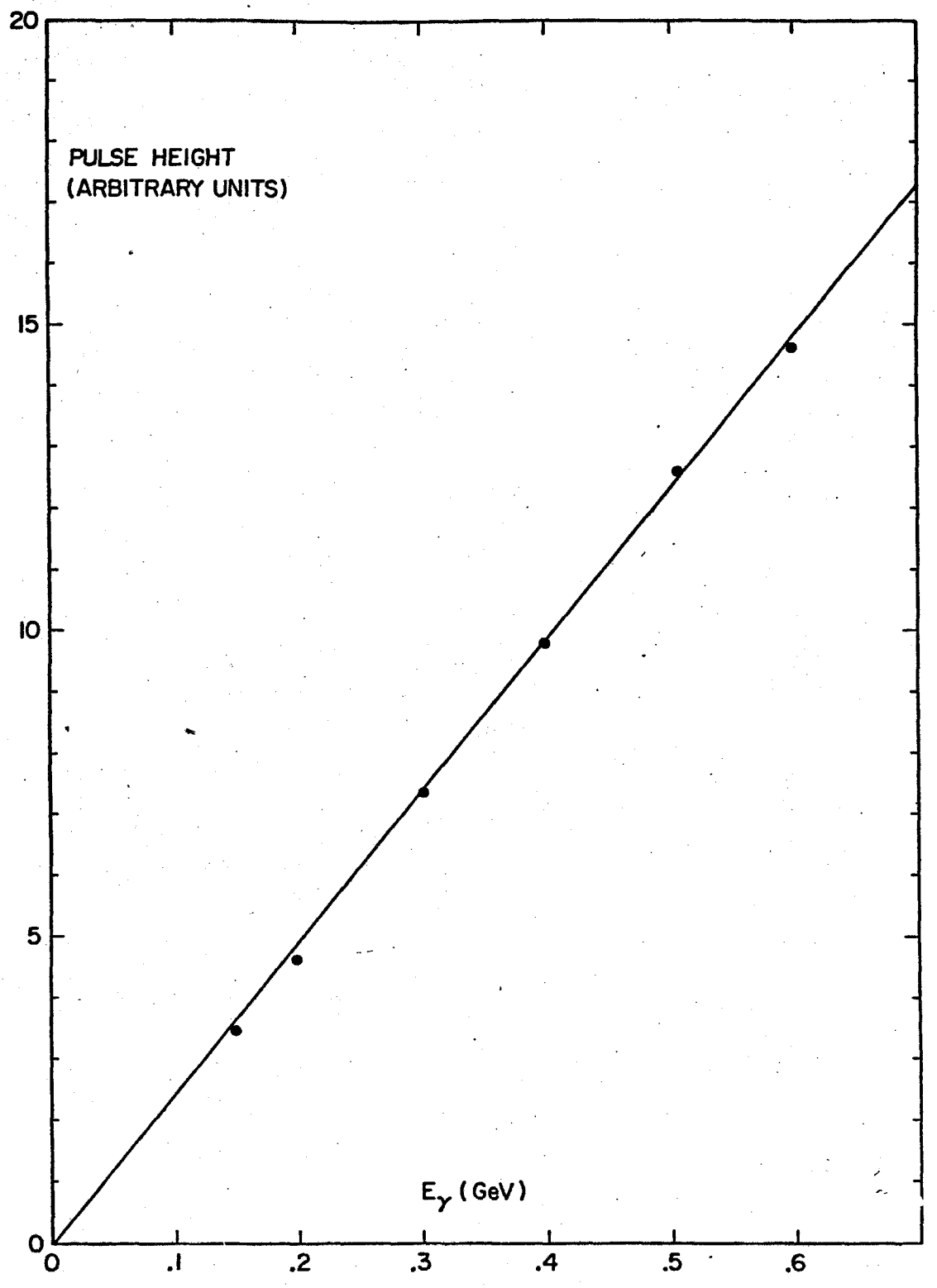

Figure 6.16 Pulse Height Versus Energy

esting to note that the resolution was as good for configuration (1) as for configurations (2) and (3). In other words, the resolution was not apparently degraded at all by splitting the radiator into sections. Figure 6.17 shows the resolution for configuration (1).

The resolution contains a largely unknown beam resolution. We investigated the extent of this contribution as follows. Using a light emitting diode, we matched the mean pulse height from the diode to that from 500 MeV electrons. The width of the spectrum using the diode was on the order of 4 to 5%, as compared to 7% using photons!

To put this in perspective, the other counter used in the experiment has a resolution of about 10% at 500 MeV. The 5% figure for the new counter represents a factor of four improvement in light collection. A better beam is needed to test the lower limit on the resolution of this counter.

4. Detailed Distributions

Pulse height distributions were taken of each component of the detector individually in order to investigate the mechanisms of shower detectors a little more fully. Figure 6.18 shows the pulse heights from each component, and the summed signal for 500 MeV positrons.

Studies of the longitudinal behavoir of showers[13,14] suggest that rather large fluctuations in the pulse heights should occur in each section of the counter . This is seen in the widths of the individual distributions. The summed signal, however, is rather well defined, again, as it is for the block alone, again illustrating there is little

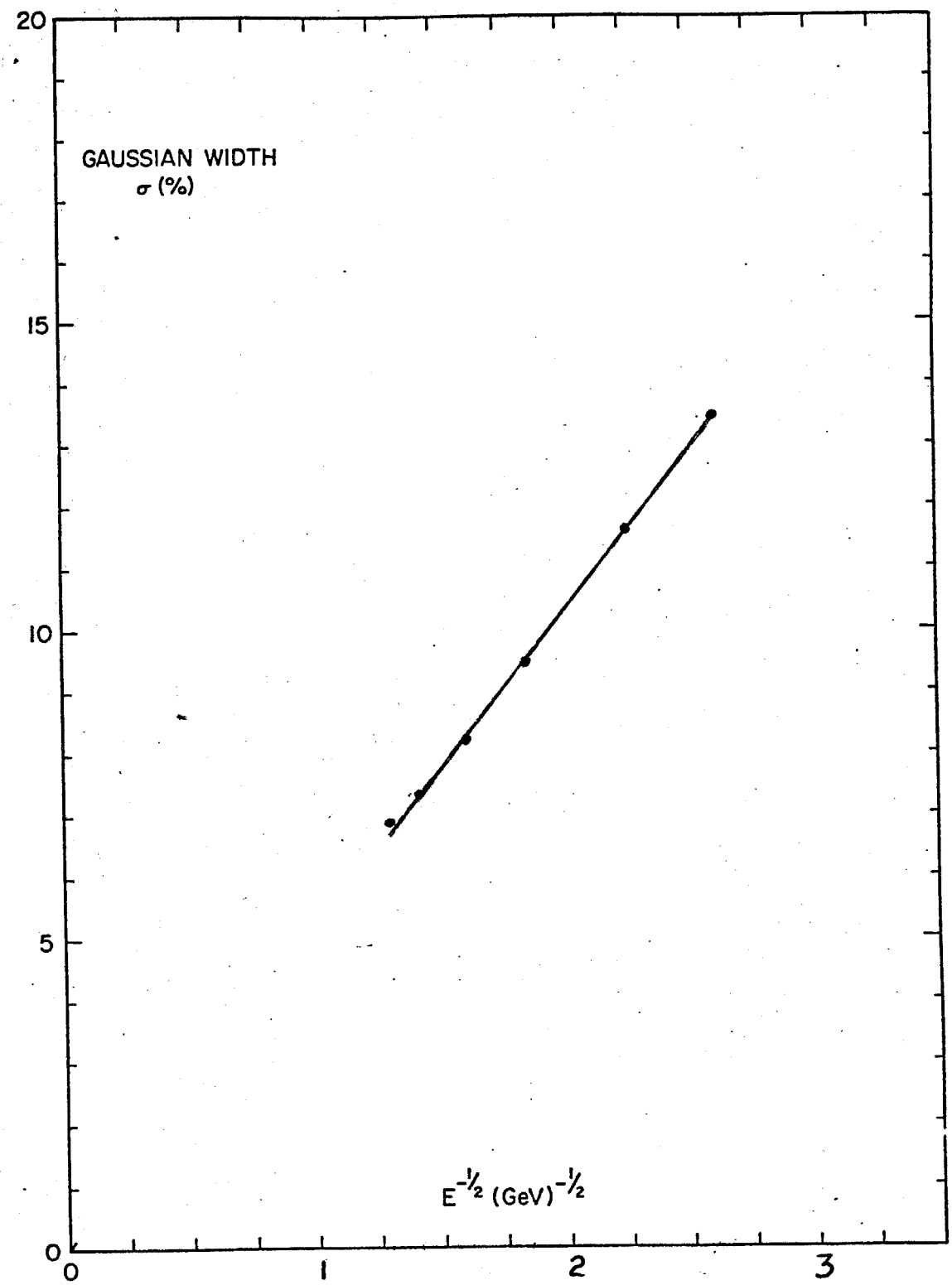

FIGURE 6.17 Energy Resolution Versus Photon Energy

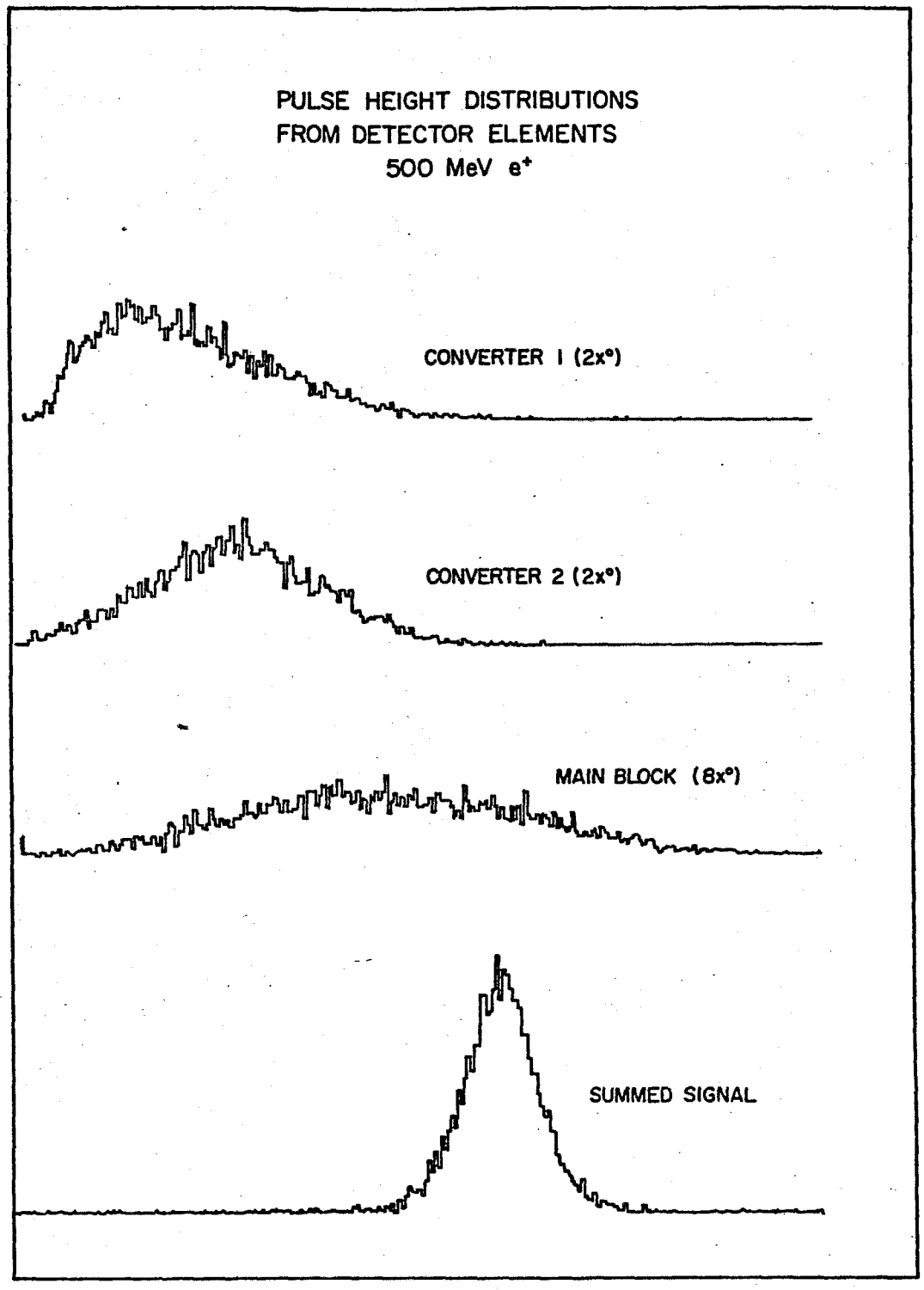

Figure 6.18 Individual Component Pulseheight Spectra

degradation of the energy resolution due to splitting the radiator into pieces.

5. Conversion Efficiency

Knowledge of the overall detection efficiency of the apparatus demanded that we know the conversion efficiency of the 2Xo converters rather well. Using coincidence and anticoincidence requirements, we measured the conversion efficiency as a function of incident photon energy.

The results are displayed in Fig. 6.19 for energies between .1 and .6 GeV. For completeness, the efficiencies are also shown for the two converter configurations, giving a total converter thickness of 4Xo. Curve 1 is applicable to the configuration used in this experiment, and shows the efficiency being only about 40% at .1 GeV, and becoming about 70% for all energies above .3 GeV. A good fit to this data is obtained by a curve of the form $A_1 + A_2 e^{-A_3 k}$, k = photon energy in MeV, $A_1 = .762558$, $A_2 = -1.00956$, $A_3 = -.0110533$.

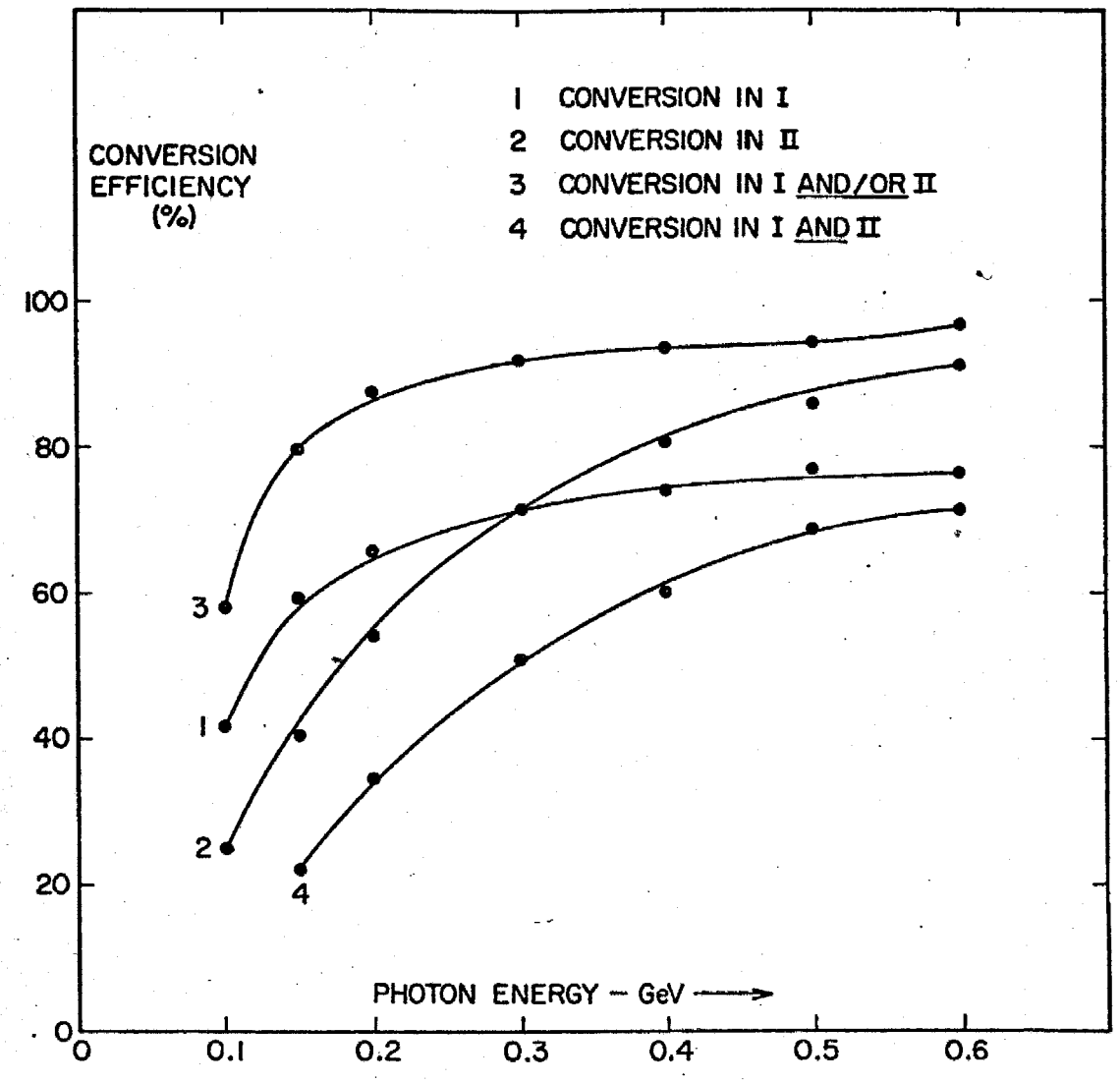

Figure 6.19 Conversion Efficiency Versus Energy for $2X^{o}$ and $4X^{o}$ Converter Configurations

E. VERTEX LOCATION - PHOTON CHAMBERS

We make the same assumptions for the photon counter spark chambers as for the helium counter chambers (cf. Appendix G), save that the chambers are not assumed to be in a plane. They were separated by about 1.5 inches. The task of the reconstruction procedure is to provide a set of slopes and intercepts from which the photon vertex is constructed.

The chambers for the photon counters consisted of four pairs of X-Y gaps for each counter. When reconstructing both tracks and vertices, the X and Y views were treated independently. Figure 6.20 shows what the positions of the sparks for an electron-positron pair shower might look like in each view.

There are two distinct steps to the vertex finding procedure:

a. Track reconstruction.

b. Vertex location.

Each step is done in both the X and Y view, in both photon counters if necessary.

1. Track Reconstruction

The procedure involves a least-squares-fit on three and four spark combinations, with the subsequent elimination of sparks used in a fit. Using the known chamber positions (see Fig. 6.21), a matrix M is pre-computed for use in constructing a straight line fit to the component tracks of a shower:

$$\begin{vmatrix} a \\ b \end{vmatrix} = M\vec{x}$$

XBL726-3115

Figure 6.20 Typical Electron Pair Shower

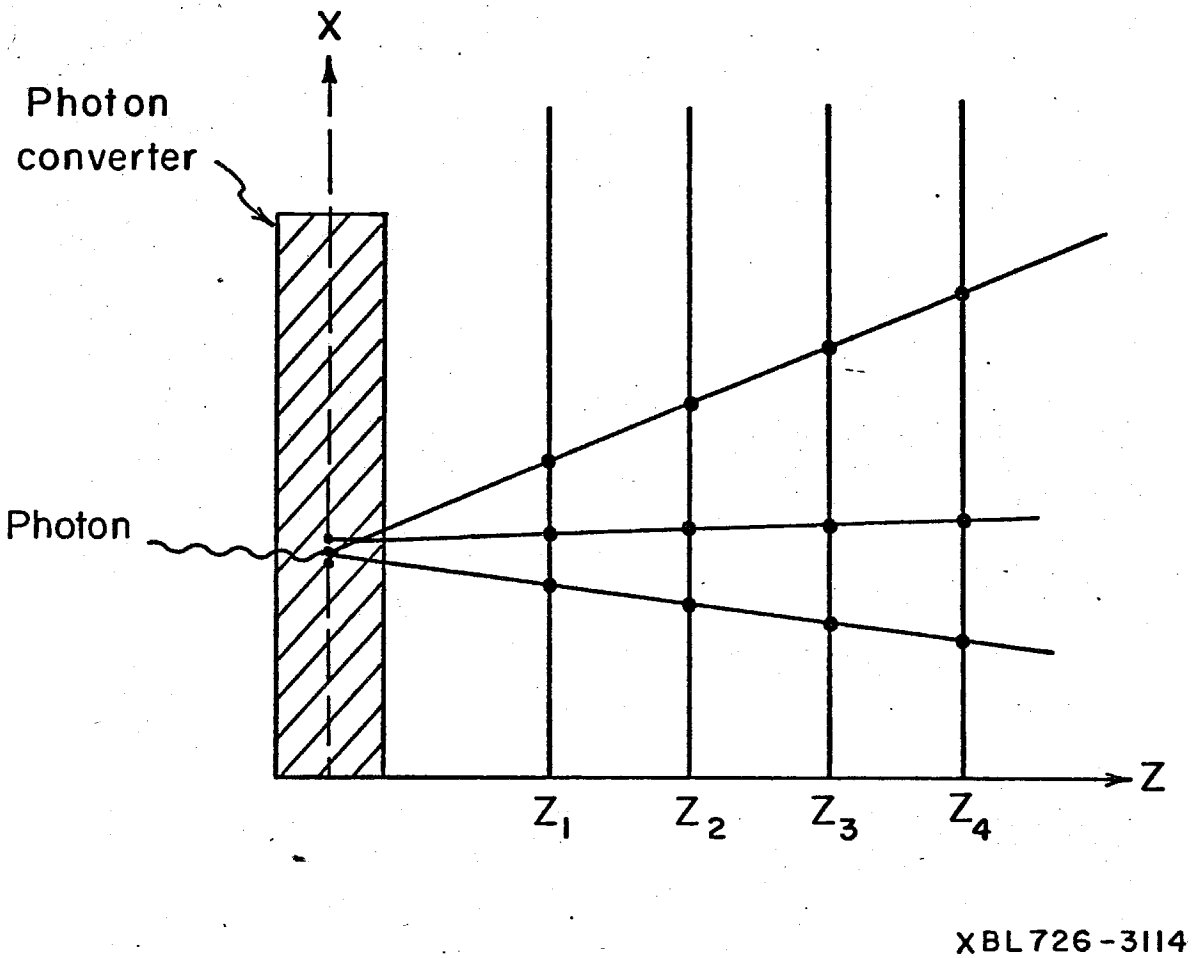

Figure 6.21 Relative Positions of Lead Glass Converter and Wire Spark Chambers

where $\vec{x}$ is a vector containing the x-coordinates of the sparks in the X-Z plane, a is the line slope, b the intercept with the X-axis. Determining the line involves only the X's; the X's are the fixed chamber positions. This allows the matrix M to be pre-computed.

Next, the distance from each spark to the fitted line is calculated and compared to a fitting parameter specified by the user. If all distances satisfy the comparison, the following information is stored:

a. slope;

b. intercept;

c. contributing sparks;

d. maximum distance from any spark to the fitted line.

The sparks "used up" by a given fit are eliminated from further consideration. The above procedure is repeated until all three and four spark combinations satisfying the constraint imposed by the fitting parameter have been found.

2. Vertex Reconstruction

Vertices are also constructed in each view independently. Basically, the procedure is to look for tracks which intersect the midplane of the converter within some specified distance from one another. Each time such a vertex is found, the tracks composing it are subsequently eliminated from further consideration.

In practice, the formation of vertices is subject to many complicating factors, especially in the photon energy region of about 150 - 450 MeV, which we find in this experiment. For pair production, one expects the RMS angle between the two electron tracks to be about

M_e/E, where M_e is the mass of the electron, E is the incident photon energy. In practice, both tracks experience some multiple scattering, more or less depending on the depth of conversion inside the converter. At times, this can be serious enough to make the point of conversion appear to occur outside of the converter.

Another potential problem comes from single track events, most probably due to one particle of a pair being absorbed. These tracks can have a substantial slope, increasing the error in the vertex location.

Following is a description of the assignment of a vertex and an associated error under three somewhat different circumstances: single tracks; a pair of tracks; and three or more tracks.

There is one major physical assumption made in the assignment of vertex positions and errors: due to the complexity of the shower process, nothing can be assumed about the trajectory of the particles' path within the converter. Errors and vertices will be assigned as though the particle's track can be projected in a straight-line fashion into the converter.

a. Single Tracks

The vertex is taken to be the intersection of the track with the midplane of the photon converter. The error is defined by the condition (see Fig. 6.22)

$$2\delta = X_o \tan \theta.$$

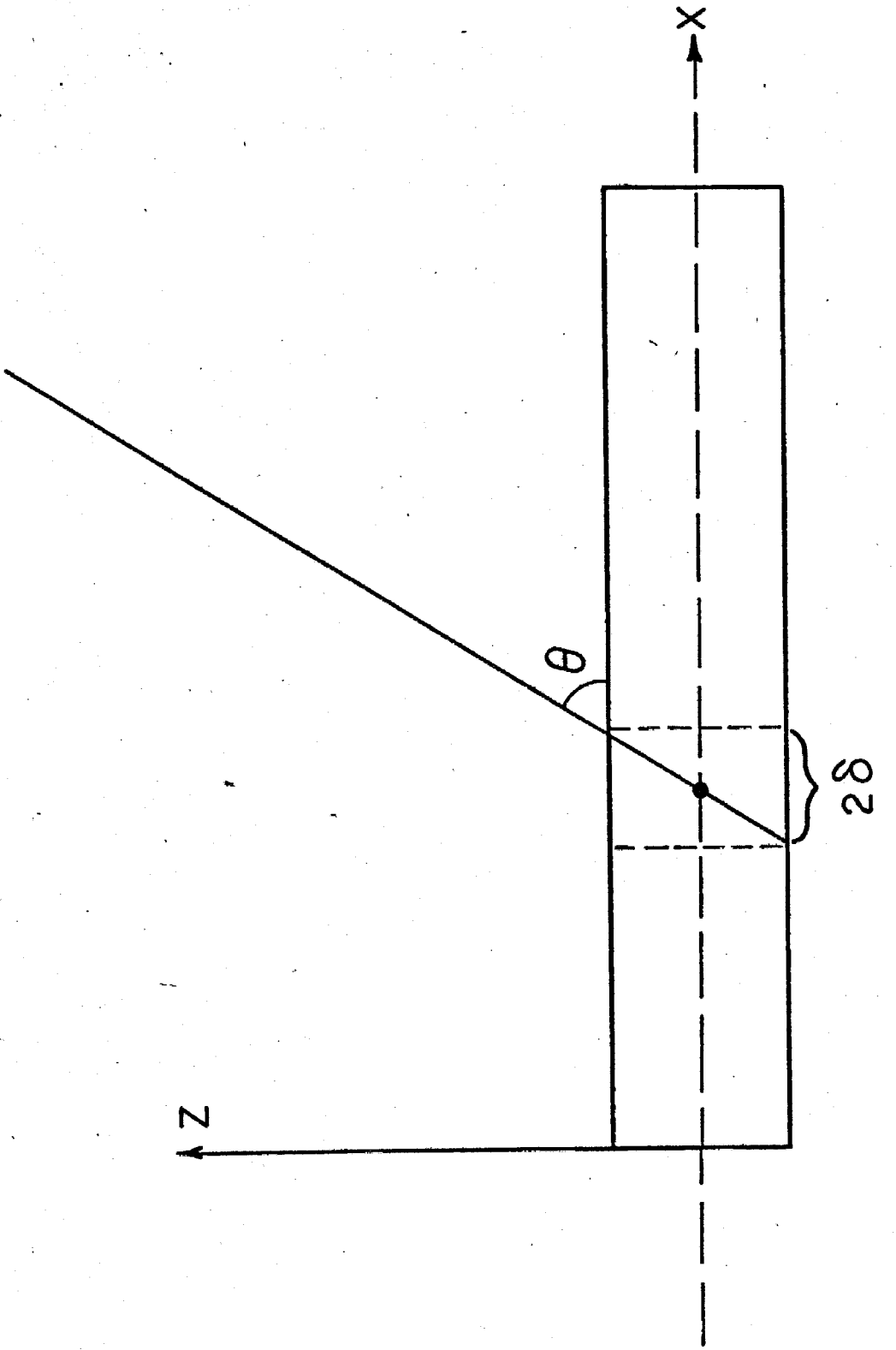

XBL726-3113

Figure 6.22 Resolution for a Single Track

b. Pairs of Tracks

Three situations are possible when pairs of tracks are considered; the apparent point of conversion can appear to be: 1) within, 2) beyond, 3) before the converter. Situations two and three arise because of multiple scattering effects. If the intersection does not lie within the converter, the two points of intersection of the tracks with one of the surfaces of the converter are required to be within a specified distance. If they are not, each intersection is considered to be a separate vertex.

For situation one, the vertex is taken to be the projection on the converter midplane of the point of intersection. Assignment of an error, on the vertex position is illustrated in Fig. 6.23.

In the second and third situation, one computes the points of closest approach of the two tracks on the surface of the converter closest to the point of intersection of the tracks. The vertex is taken to be the midpoint of the two points on the surface. The error is taken to be one-half the maximum distance between points of intersection with the top and bottom surface of the converter.

Figure 6.24 illustrates why all four points of intersection must be considered for pairs of tracks. About one half of the time, due to multiple scattering, one expects the tracks to have the same slope. Using the points of intersection on only one surface could clearly cause one to seriously underestimate the error in the vertex position.

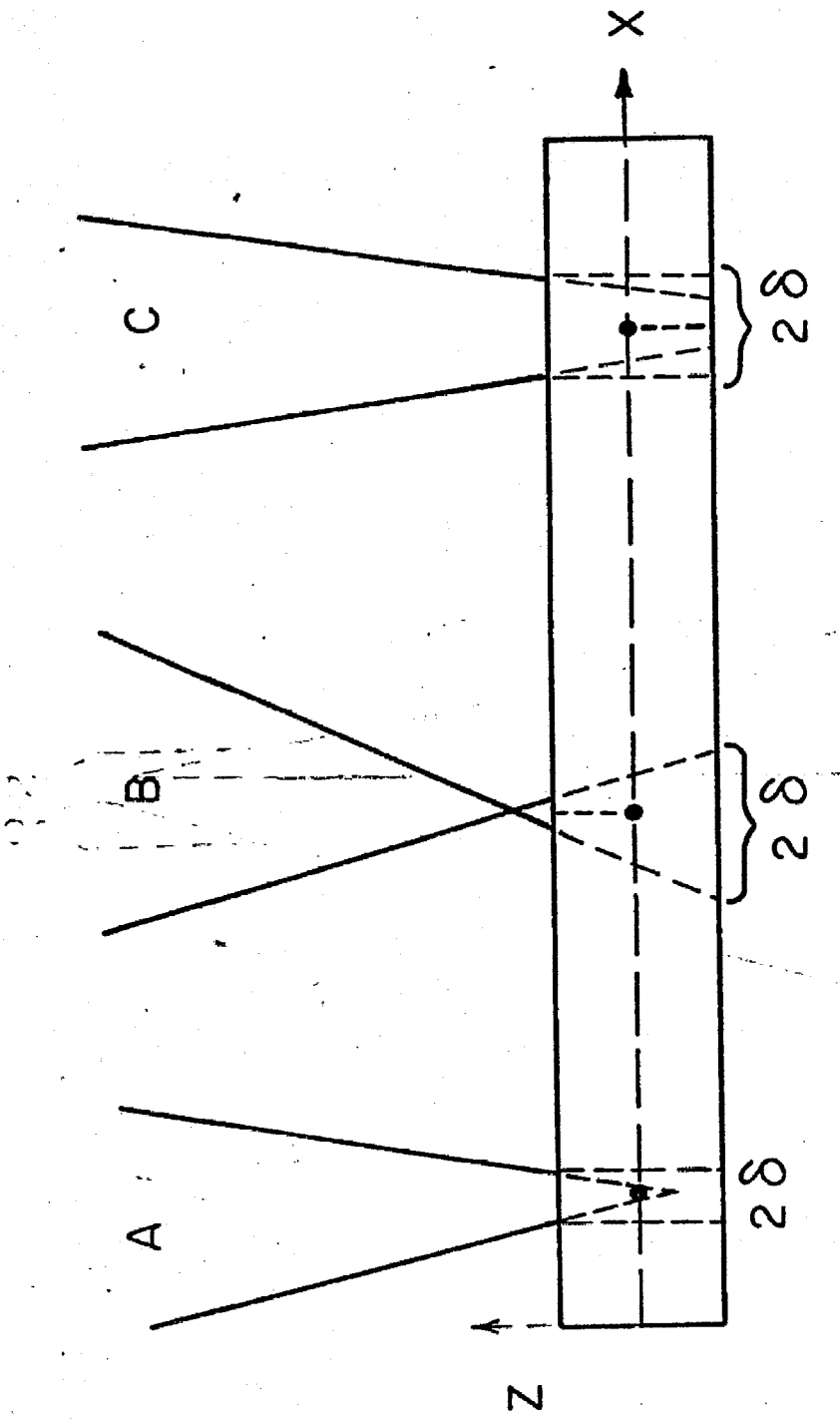

XBL726-3112

Figure 6.23 Assignment of a Vertex Error - Pairs of Tracks

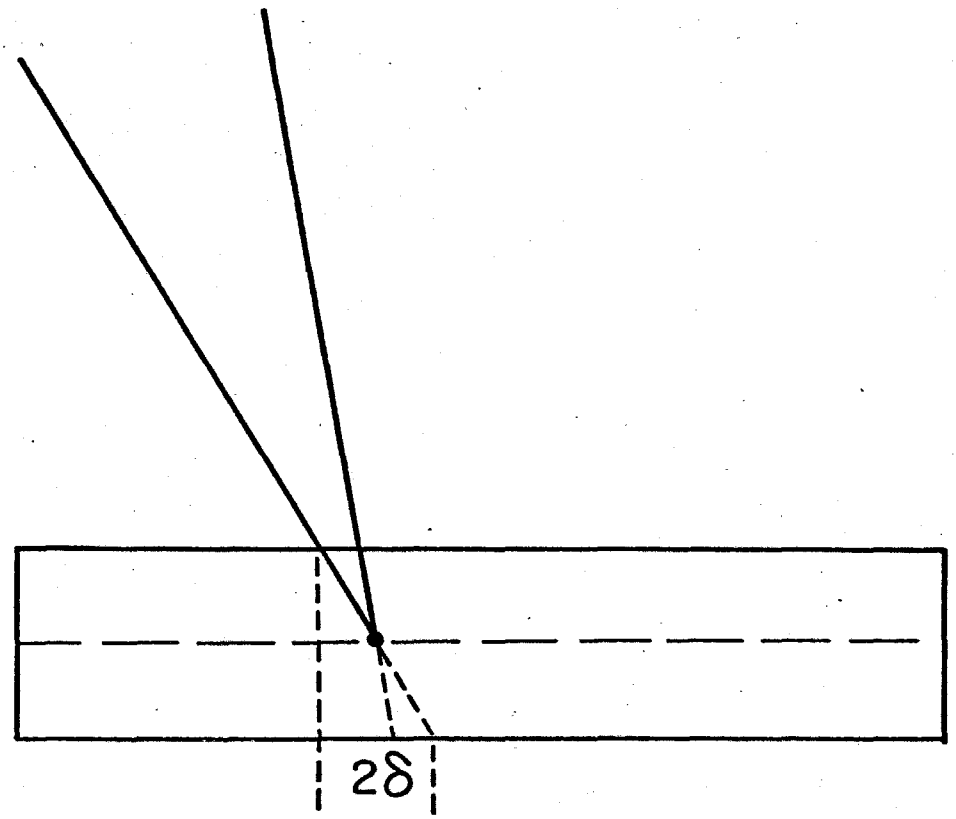

XBL726-3110

Figure 6.24 Assignment of a Vertex Error When Both Tracks Have the Same Slope

c. Three or More Tracks

Showers involving three or more tracks are treated as overlaps of pairs of tracks. Using the vertex assignment described for pairs, one now searches to see whether any vertices due to pairs of tracks overlap within the fit parameter. If so, one then checks to see whether the pairs have a track in common. If so, the number of tracks contributing to a vertex is reduced by one. The vertex coordinate is taken as the mean of the component vertex pairs.

An error is assigned as with pairs of tracks. The absolute maximum is computed for the distance between the intersection of any pair of component tracks with either surface of the converter. The error is one half of this distance. (See fig. 6.25).

For each of above situations, and for each vertex located, the following information was recorded:

1. X and Y coordinates;
2. errors in X and Y coordinates;
3. the number of tracks contributing to a vertex, in each view;
4. the distance of closest approach - meaningful only for pairs.

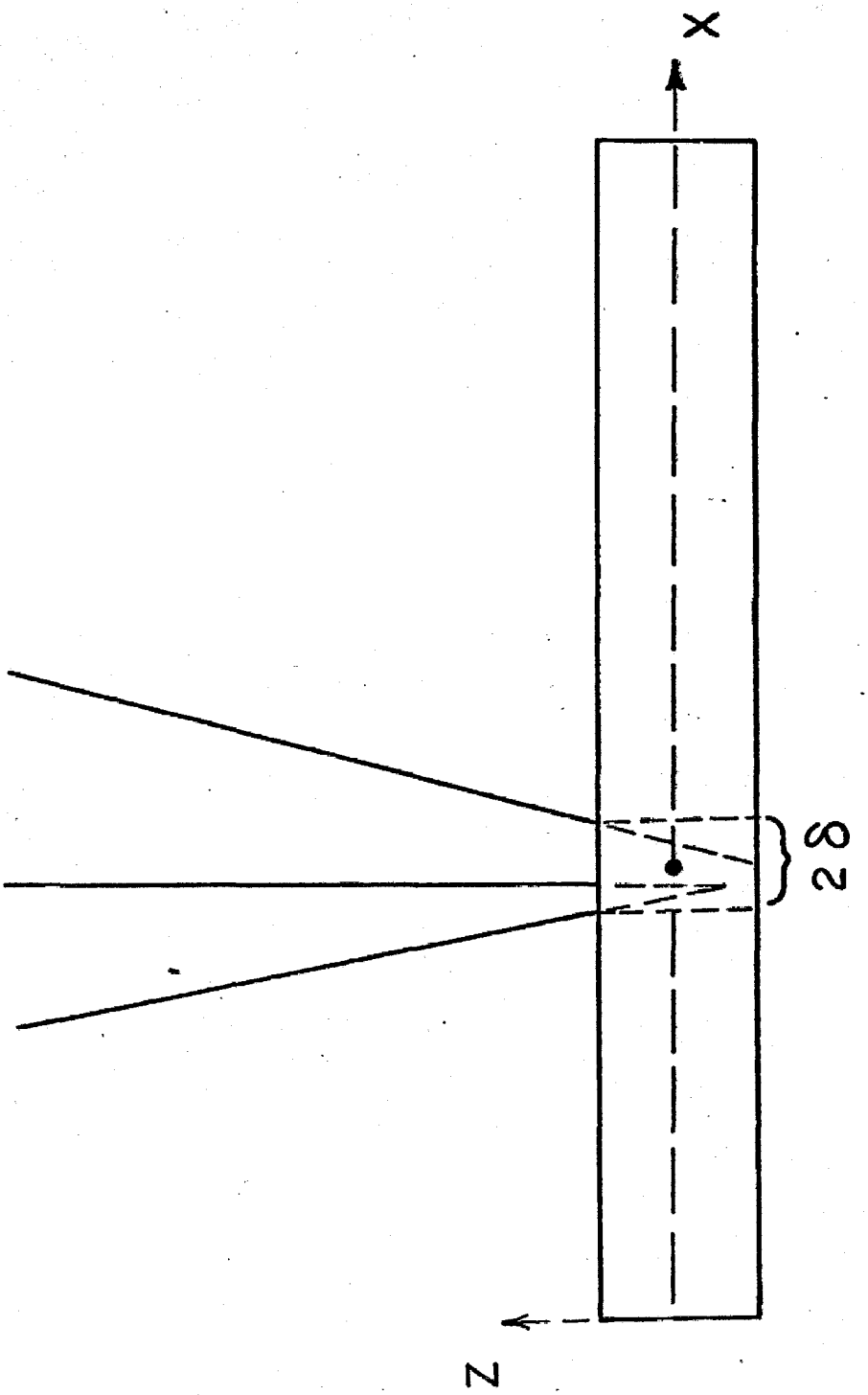

Figure 6.25 Assignment of a Vertex Error - Three Tracks

F. HELIUM DETECTOR

General Overview

In this section we discuss the construction and use of a thick plastic total absorption scintillation counter for the detection and energy determination of He^3 particles. Counters of this type have been used before for protons[15,16] in the energy region $\leq$ 160 MeV. The momentum resolution obtained by us was on the order of 1.5% with good uniformity across the face of the counter.

Two factors motivated the development of such a counter for this experiment:

1. It was desirable to let the photon detectors determine the geometric efficiency. Without moving the counter, it provided total angular acceptance of the lab He^3's. This enabled us to detect photons at any lab angle without moving the helium counter. Also, we were able to increase the geometric efficiency of the experiment by using two photon detectors.
2. A detector was called for with a dynamic range of about 60 to 340 MeV He^3's.

A magnet/wire-chamber spectrometer was considered. The small lab angle of the helium at some settings (as low as 7^o), loss of solid angle, and prohibitive amounts of absorber, especially for settings with low helium energies, were some of the reasons for not choosing this option. Other points of comparison will be made later.

1. Construction

Figure 6.26 shows an exploded view of the counter (not necessarily to scale), and Fig. 6.27 shows some construction details.

The active area of the detector consisted of a block of pilot y scintillator 60 centimeters wide and high, and 10.65 centimeters thick. The thickness was chosen so as to just stop 430 MeV He^3's. The light pipe consisted of two parts: (1) a 45 centimeter high × 60 centimeter wide × 10.65 centimeter thick piece of lucite; (2) 4.5 inch in diameter × 5 inch lucite cylinders. Each cylinder was rounded, on one end, to fit the face of an RCA-4522 phototube.

Except for the top and bottom, the whole counter was wrapped with aluminized mylar, and one layer of two mil aluminum. The nonactive area was, additionally, wrapped with black tape.

The whole counter was mounted in a 1/4 inch iron frame, which served both to provide mechanical rigidity, and shielding from stray fields. In addition, each photomultiplier tube had its own μ-metal shield.

For about two-thirds of the runs a differential pulse height counter was placed in front of the helium counter. This consisted of a 1/8 inch scintillation counter, connected by a folded light pipe to an RCA-4522 phototube. Thin mylar sheets were appropriately shaped and placed so as to increase the uniform thickness of this counter.

2. Stability

In order to minimize the effects of drifts in the helium counter, the phototubes were closely monitored. As shown in Fig. 6.27, three

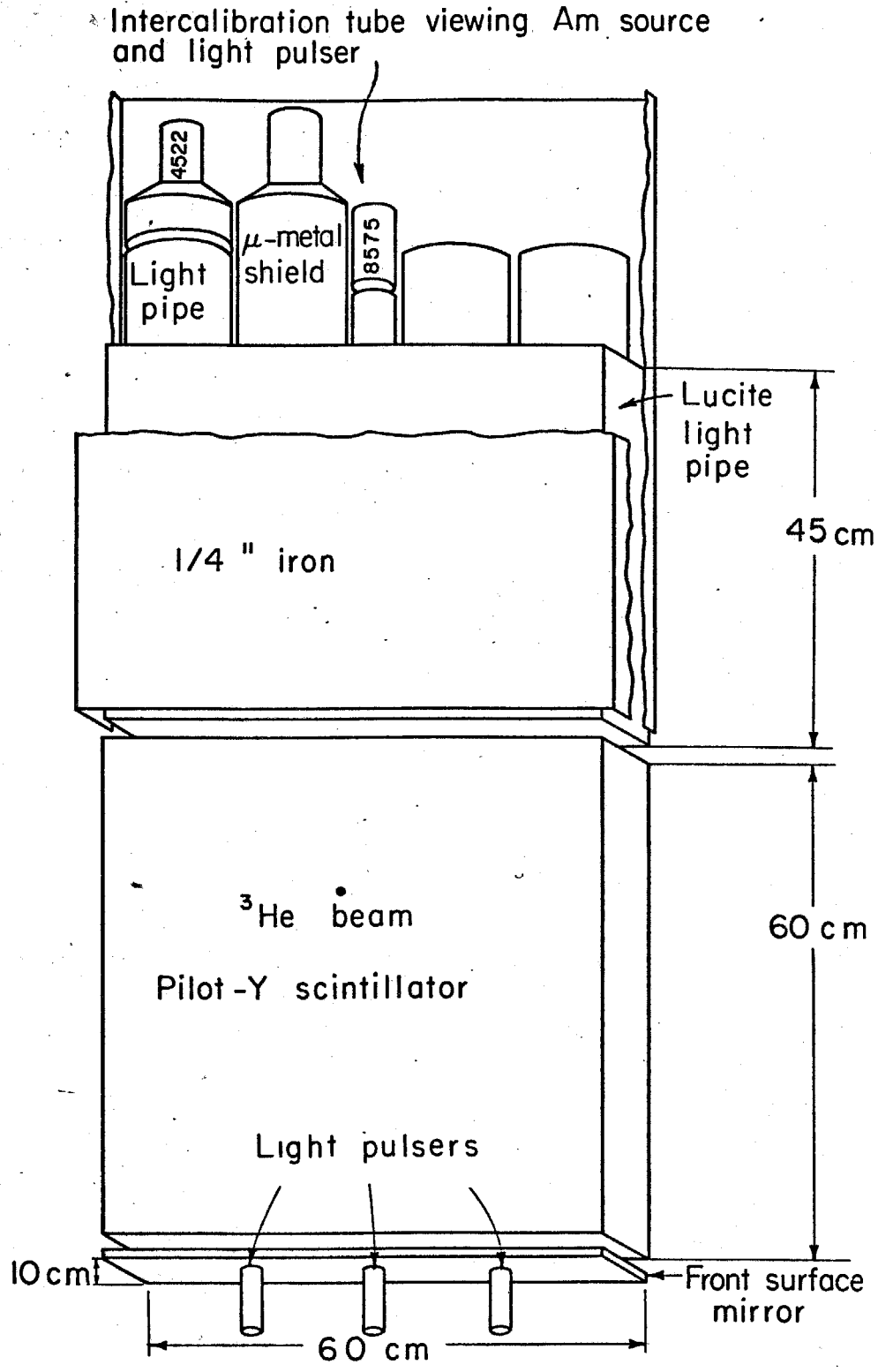

Figure 6.26 Exploded View of the Helium Detector

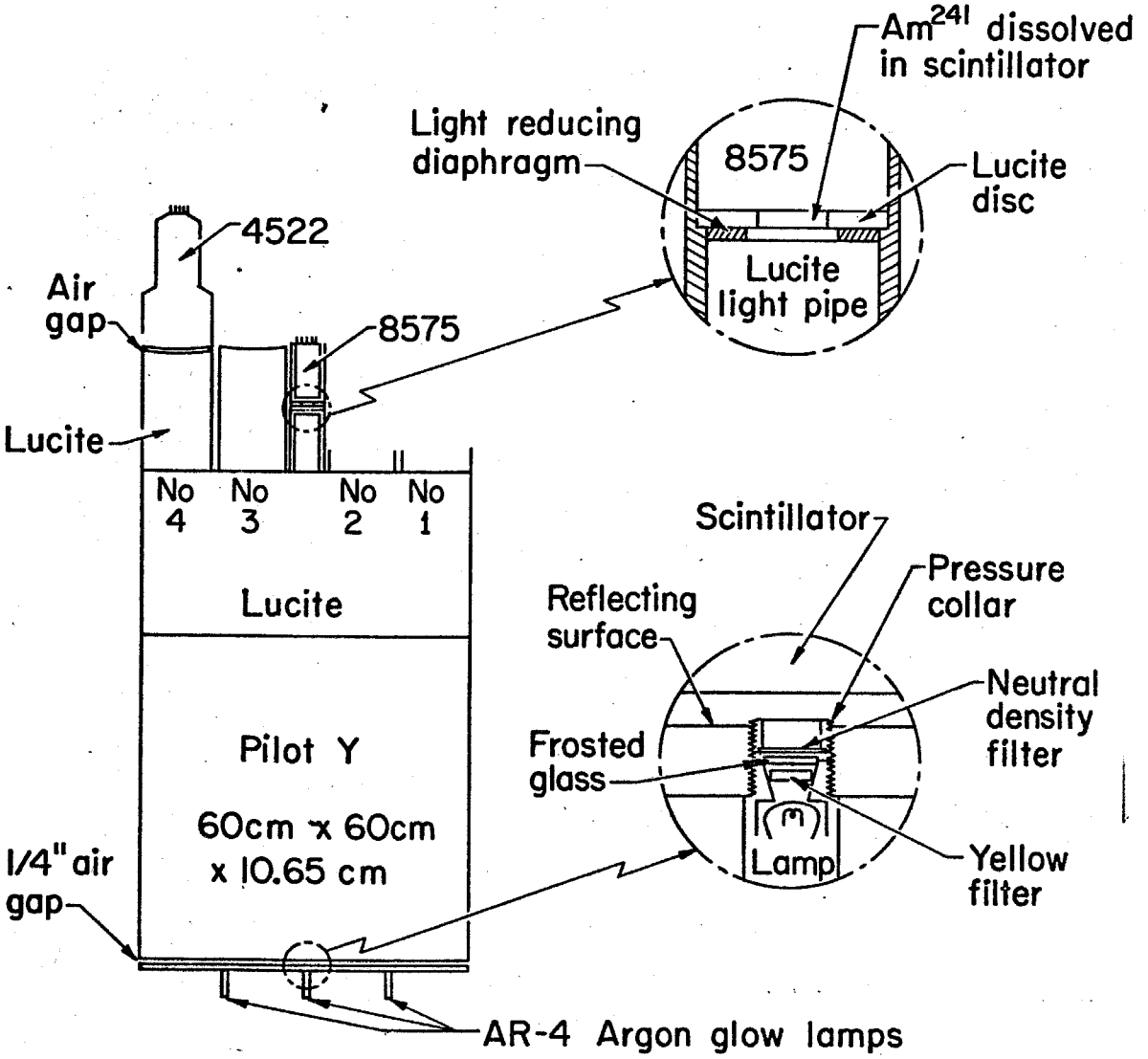

Figure 6.27 Helium Detector Construction Details

AR-428 argon glow lamps were mounted on the bottom of the counter. Before the experiment, these lamps were tested and found to have pulse height stabilities of about one percent per week. During the experiment, these lamps were flashed continuously, and served as a reference.

Figure 6.28 shows a schematic layout of the electronics associated with the helium counter. The output of the helium counter entered a linear gate, gated for stabilization purposes by an appropriately timed signal from the argon lamp, then through a linear amplifier, a biased amplifier, and finally into a pulse height analyzer (PHA). A signal from the PHA was fed into a Canberra digital stabilizer. This device continuously adjusted the linear amplifier gain so as to, one the average, keep the argon flash pulses in the appropriate PHA channel. If the phototube voltages drifted too far, the power supplies had to be adjusted (the voltages of the power supplies were measured with a digital volt meter at least every eight hours).

Periodically, the stability of the argon lamps themselves was checked against an Americium-241 source. Notice in Fig. 6.26 that the 8575 phototube is directed at both the source and the argon flashlamps. Spectra were taken periodically using a PHA of the flashlamps and the source simultaneously. Figure 6.29 shows the part of the spectrum for the Americium-241 source.

The procedure was to compute intercept of a straight line fit to the linear portion of spectrum (as indicated in Fig. 6.29) with the channel number. If necessary, the power supply voltage on the 8575

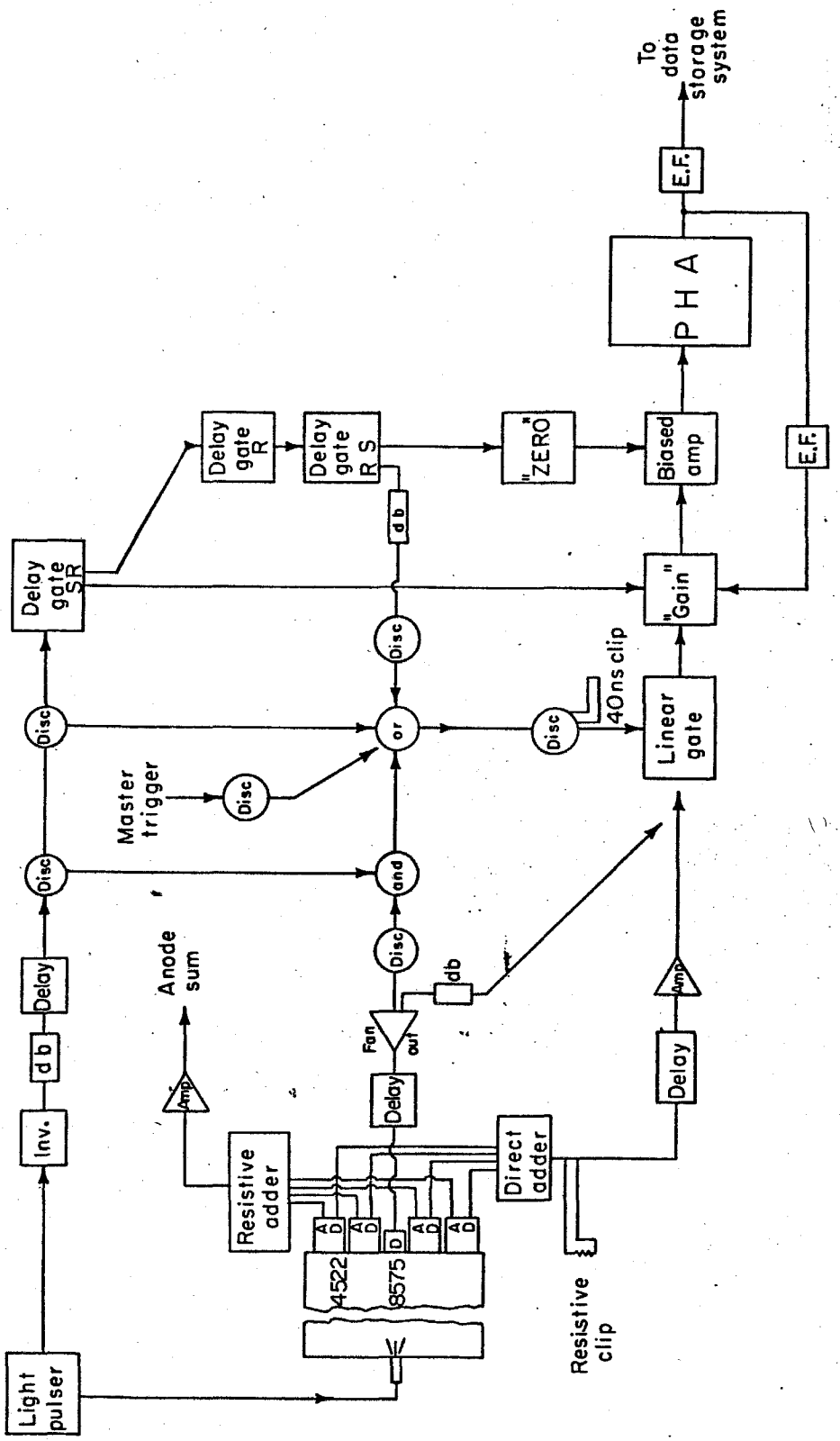

Figure 6.28 Helium Detector Logic Electronics

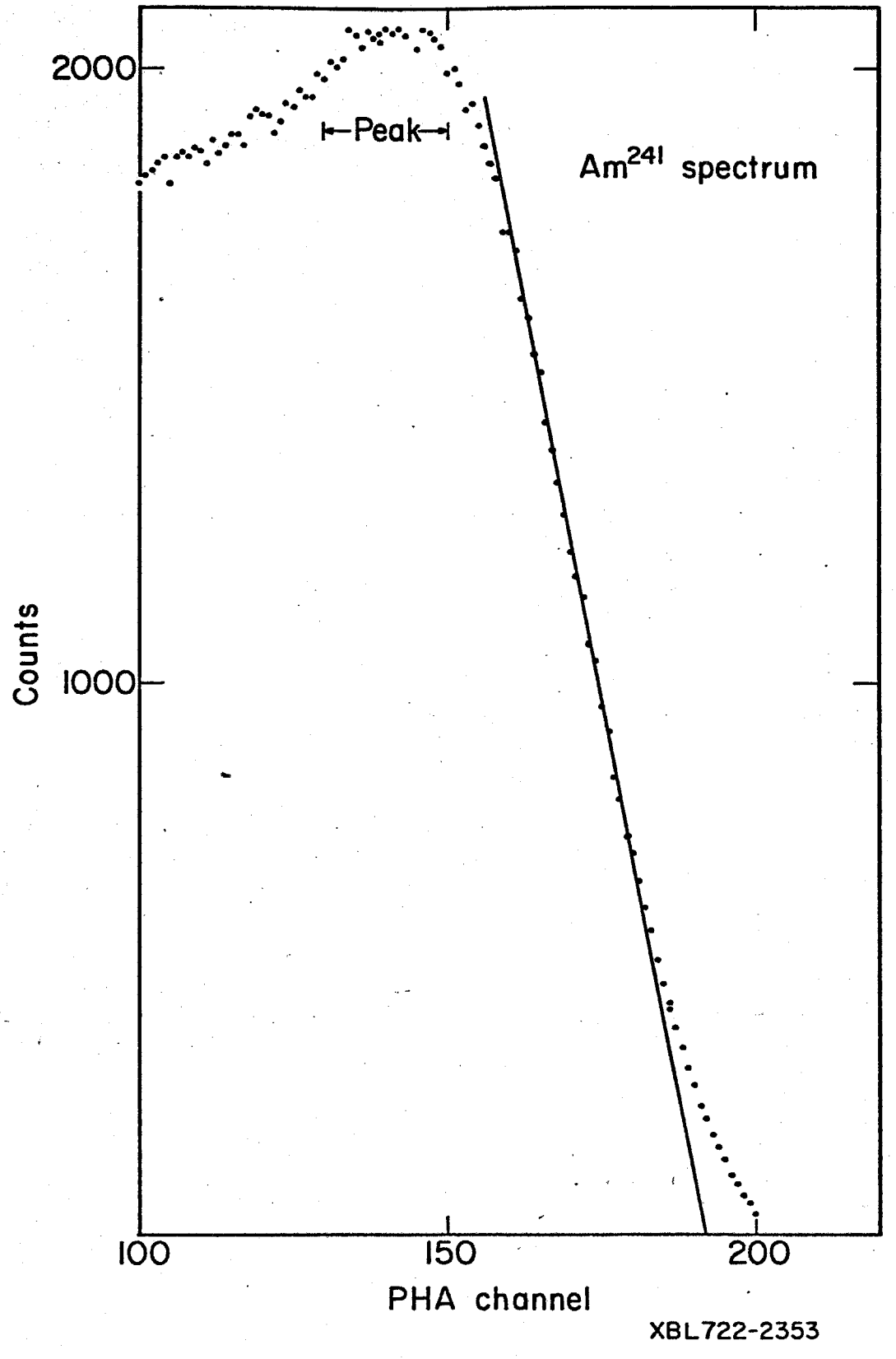

Figure 6.29 Americium-241 Energy Spectrum

phototube was adjusted to make this point fall into the appropriate channel. With new voltage on the phototubes, the voltage bias on the argon lamp in general had to be changed to make it fall in the appropriate channel. At this point the argon flash lamps themselves were calibrated and acted as a temporary standard while data were being taken.

3. Differential Pulse Height Counter

The helium detector presents a large surface for randoms, and during the setup of the experiment it was realized that the trigger rate was prohibitive. A differential pulse height counter (henceforth DEDX counter) was added to the trigger for all runs where the helium energy was greater than 100 MeV. A discriminator level was set on this counter using passing alpha particles. The discriminator level was set conservatively. Installation of this counter reduced the trigger rate by a factor of 50. Figure 4.3 is an example of a PHA distribution of some of the data, showing the helium peak.

The voltage on the phototube for this counter was carefully monitored, in anticipation of having to add the DEDX pulse height to that of the main scintillator, for some runs, to obtain the helium particle's energy. Adding the two pulse heights, rather than considering the DEDX counter to be an ionization energy loss and correcting for this, was to be done only as a last resort, however. Heavy charged particles passing through thin amounts of material obey a Vavilow distribution in the energy lost to the material. Thus the fluctuations in pulse height can be large, especially for high energy heavy charged particles, broadening the resolution accordingly.

4. Total Absorption Scintillation Counters vs. Magnet/Wire Chamber Spectrometers

The biggest advantages of a magnet/wire-chamber spectrometer (MWCS) is the relative simplicity of the physics of the device, and the typically .5% momentum resolution obtainable. The primary advantage of a total absorption scintillation counter (TASC) is the large solid angle available. For this experiment, it was a distinct advantage to have the geometric efficiency determined solely by the photon counters. Location of photon vertices to any precision at these energies is difficult, and would have made determination of the solid angle difficult and imprecise had the helium counter not accepted all lab angles available to the photon counters.

The TASC is potentially a more compact device, and it is possible to reduce the amount of energy absorbing material in the particle's path more with it than with a MWCS. This was important at some kinematic settings where using a MWCS would have made it impossible to measure the energy of the helium before it was absorbed.

As mentioned, the simplicity of the physics involved with a MWCS is a very distinct advantage. The TASC we ultimately used was a complicated device when investigated in detail. With a MWCS one needs only insure that the magnet and wire chambers function properly. With a TASC one suffers from all the problems possible with scintillation counter : light leaks; phototube stabilities; the need for mapping ; energy tails which are in general energy dependent ; somewhat inferior resolution ; possible changes in the characteristics of the plastic with age ; radiation exposure ; stress.

With a MWCS, problems with particle breakup, and background in general tend to be less serious, as one measures the energy of all particles independently. The TASC gives an energy averaged over all particles within the trigger. In addition, the TASC must be tailored for each energy range.

If the thickness of the counter is more than that necessary to absorb the highest energy particle of interest, one runs the risk of large pulse heights due to highly penetrating backgrounds. Both devices have their respective energy regions where they are best suited. Simplicity and resolution argue for the MWCS where possible. Calibration is simple: magnet currents can quite standardly be kept to within a few tenths of a percent; wire orbiting can be used for the momentum calibration. Calibration of the TASC usually demands accelerator time. This can be expensive.

One way to improve future designs of TASC's might be to consider a modular approach. If the detector were constructed of, for example, 3/4-inch sheets of scintillator, each sheet joined to its own phototube by a folded light pipe, then the total thickness of the detector could be tailed closely to the kinematic demands of each experimental situation. Ambiguities due to highly penetrating backgrounds would be greatly reduced by the veto counter situated behind the detector. One would, additionally, have an immediate range measurement by recording the number of modules penetrated. An alternative method to the one reported above would have to be devised for keeping the phototubes calibrated.

5. Calibration

Two sources of data were used in order to calibrate the He^3 counter:

a. Information collected using the 88-inch cyclotron at LBL. A well collimated He^3 beam, with a $\Delta p/p$ resolution of about .01% FWHM, at energies of 69 and 130 MeV, provided two points.

b. Data collected on the 184-inch cyclotron at LBL. This data was relatively free of a background and yielded He^3's of known energies in the region of 200 - 265 MeV.

Thus the calibration data spanned an energy region of about 69 - 265 MeV. Each data point provided two quantities needed for subsequent analysis:

a. the energy of the He^3 particle at the front (i.e., closest to the target) surface of the counter.

b. the counter pulse height.

Using these quantities a predicted counter response was derived. Other workers[15,16] had determined that the light output of a piece of scintillator in response to a charge particle is well represented by:

$$dL/dx = g \cdot dE/dx \cdot (1 + b\, dE/dx)^{-1}$$

where

dE/dx = ionization loss of the He^3 in the scintillator

b = a saturation parameter

g = the gain of the counter

dL/dx = light output of the scintillator

The resulting pulse height is assumed to be equal to the total light output, with g,b appropriately adjusted, as will be discussed. Thus:

$$\text{Pulse height} = \int_o^V dL = \int_o^V g\, dE/(1 + B\, dE/dx)$$

Letting

$$E = m\gamma, \quad dE = m\beta\gamma^3 d\beta$$

$$\text{Pulse height} = \int_o^V \frac{g \cdot m \cdot \beta d\beta}{(1-\beta^2)3/2\ (1+b\ dE/dx)}$$

where

V = He^3 velocity at the front surface of the counter

m = He^3 mass

Using the above definition of the predicted pulse height, the parameters b,g were determined using a least square minimization technique. Using the observed pulse heights, the parameters b,g were adjusted so as to minimize the quantity

$$\chi^2 = \sum_i \frac{(pH_i(obs) - pH_i(pred)^2}{\sigma_i^2}$$

The resultant values of b,g giving the best fit are:

$$b = 9.566 \times 10^{-3}$$

$$g = 1.325$$

Using this empirical form for pulse height as a function of energy, a fit was produced which provided the helium energy, as a function of pulse height, at the point it entered the detector.

A function of the form

$$E_c = A_1 * \text{Exp}\,(A_2 * E_L) + \sum_{i=1}^{5} A_{i+2} * E_L^{i-1}$$

where

E_c = energy at the surface of the counter

E_L = pulse height-pedestal

was used. The values of the coefficients used are:

A_1 = -18.3142

A_2 = -.122678

A_3 = 22.528

A_4 = 1.52817

A_5 = -3.04728E-3

A_6 = 7.73417E-6

A_7 = -7.80569E-9

To obtain the value of the kinetic energy at the event origin, taken to be the target midplane, a correction must be made for ionization losses in going from the target to the detector. This is a function of the experimental context of the counter rather than the calibration of the counter itself. Here the functional form used was

$$E_T = C_1 \cdot \mathrm{Exp}\,(E_c/-C_2) + C_3 + C_4 * E_c$$

Where E_T is the energy at the center of the target. The values of the C_i's used are:

C_1 = 64.4612

C_2 = 72.6527

C_3 = 40.5348

C_4 = .939958

When using the thin target, the differential pulse height counter was not in place. The values of the C_i's in this situation are:

$$C_1 = 40.7473$$
$$C_2 = 43.2372$$
$$C_3 = 26.283$$
$$C_4 = .939052$$

Shown in Fig. 6.30 is a pulse height spectrum using 114.6 MeV incident He^3's. Figure 6.31 shows the same plot with a logarithmic scale. The shoulders in the second plot are due to He^3 breakup, and saturation effects. These effects are energy dependent. As the helium energy increases the fraction of the distribution within these tails increases, up to about 7% at 250 MeV. These shoulders were studied carefully, and a correction for them was made for this effect in the data analysis.

Using data on the light output charged particles in plastic scintillator as a function of energy, a computer program to simulate the counter response was produced. Figure 6.32 shows the results for incident particles with kinetic energies from 0 to 500 MeV for a four-inch thick counter. The response is seen to be fairly linear above 100 MeV incident energy. The peak occurs at the energy for which the particles pass through the counter. Notice that for a counter of this thickness He^3's with a kinetic energy greater than 210 produces a unique pulse if, as was the case, only protons, deuterons and He^3's are present.

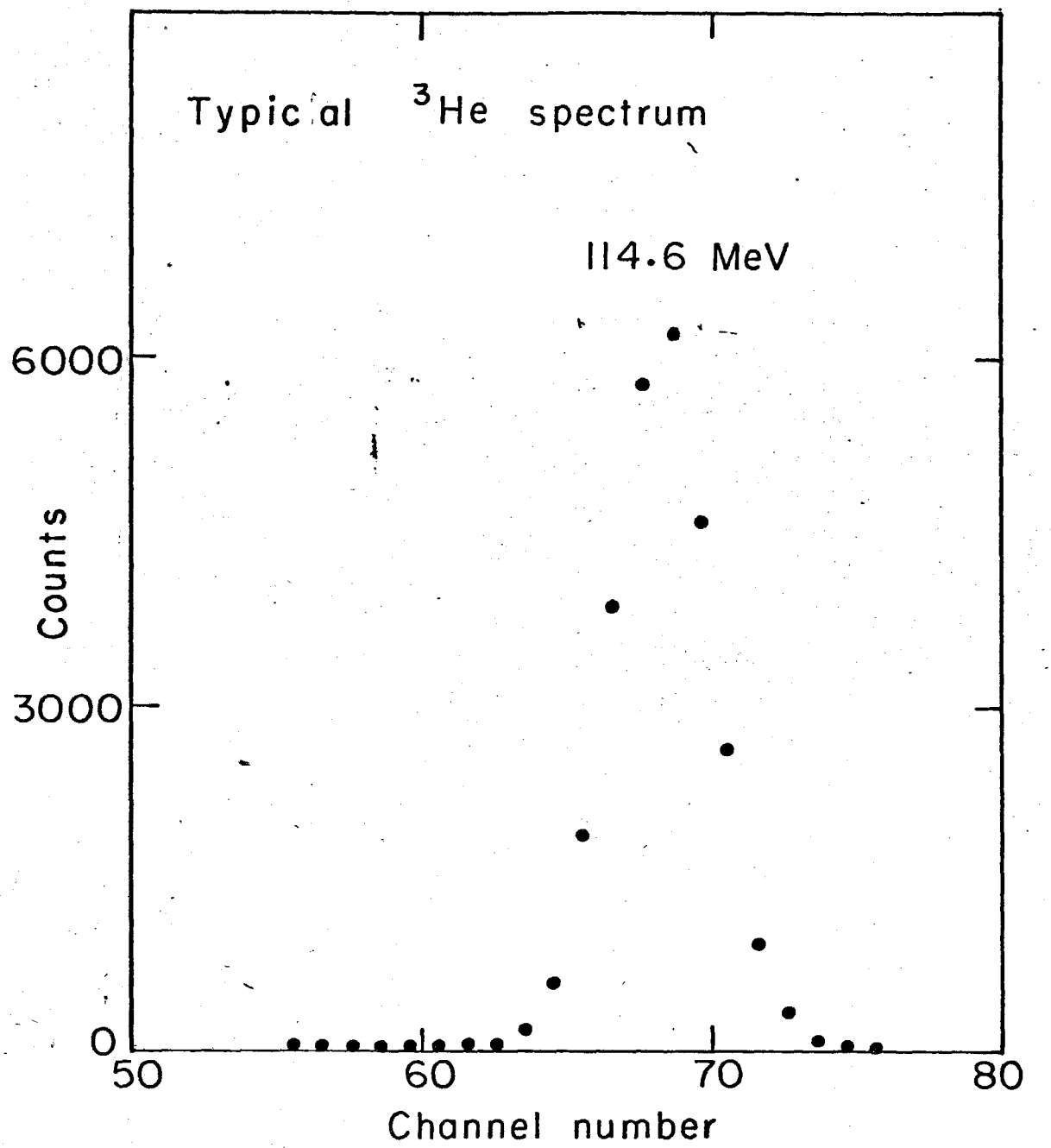

Figure 6.30 Typical He^3 Spectrum - 114.6 MeV Heliums

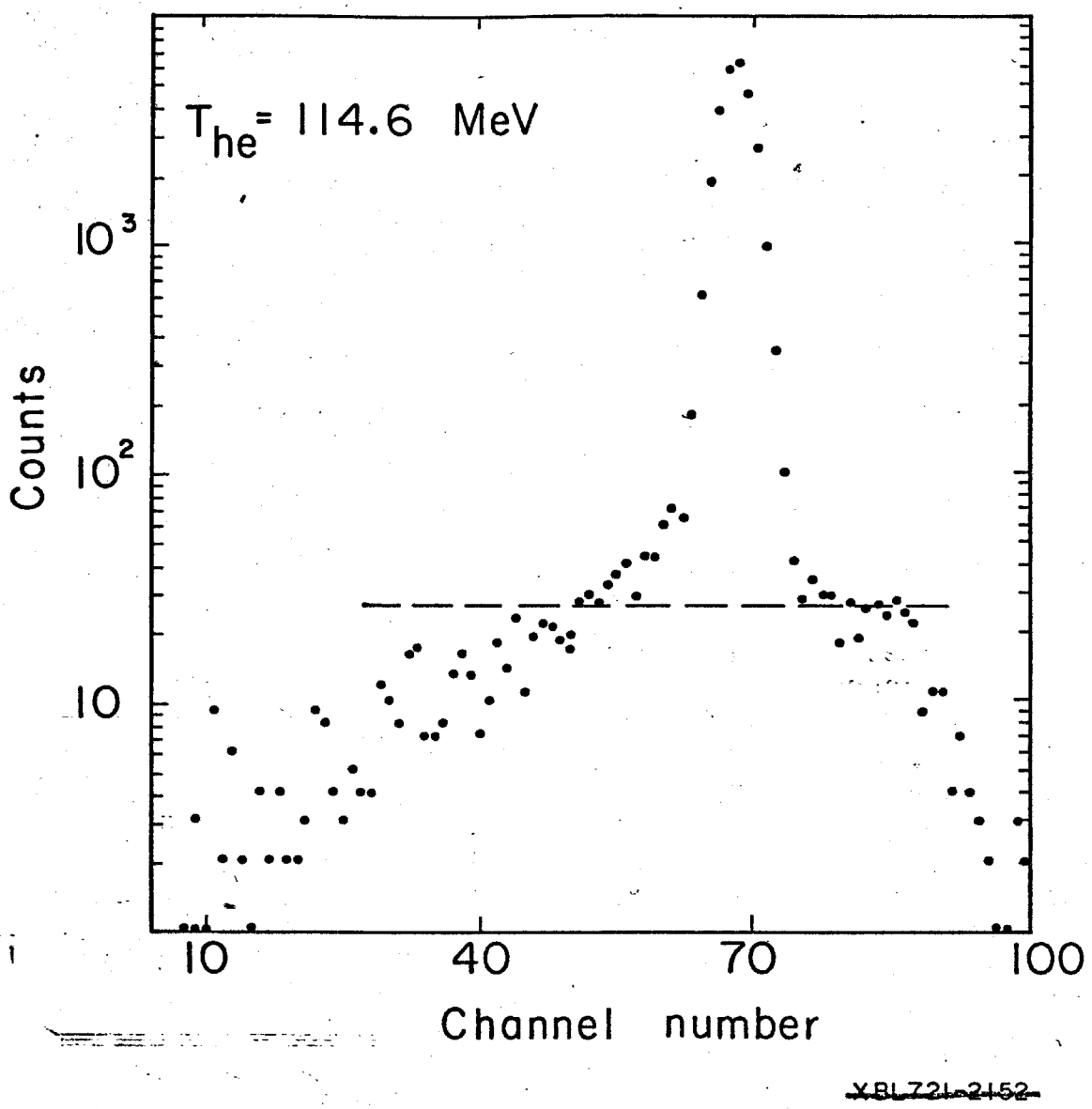

Figure 6.31 Typical He^3 Spectrum - 114.6 MeV Heliums - Log Scale

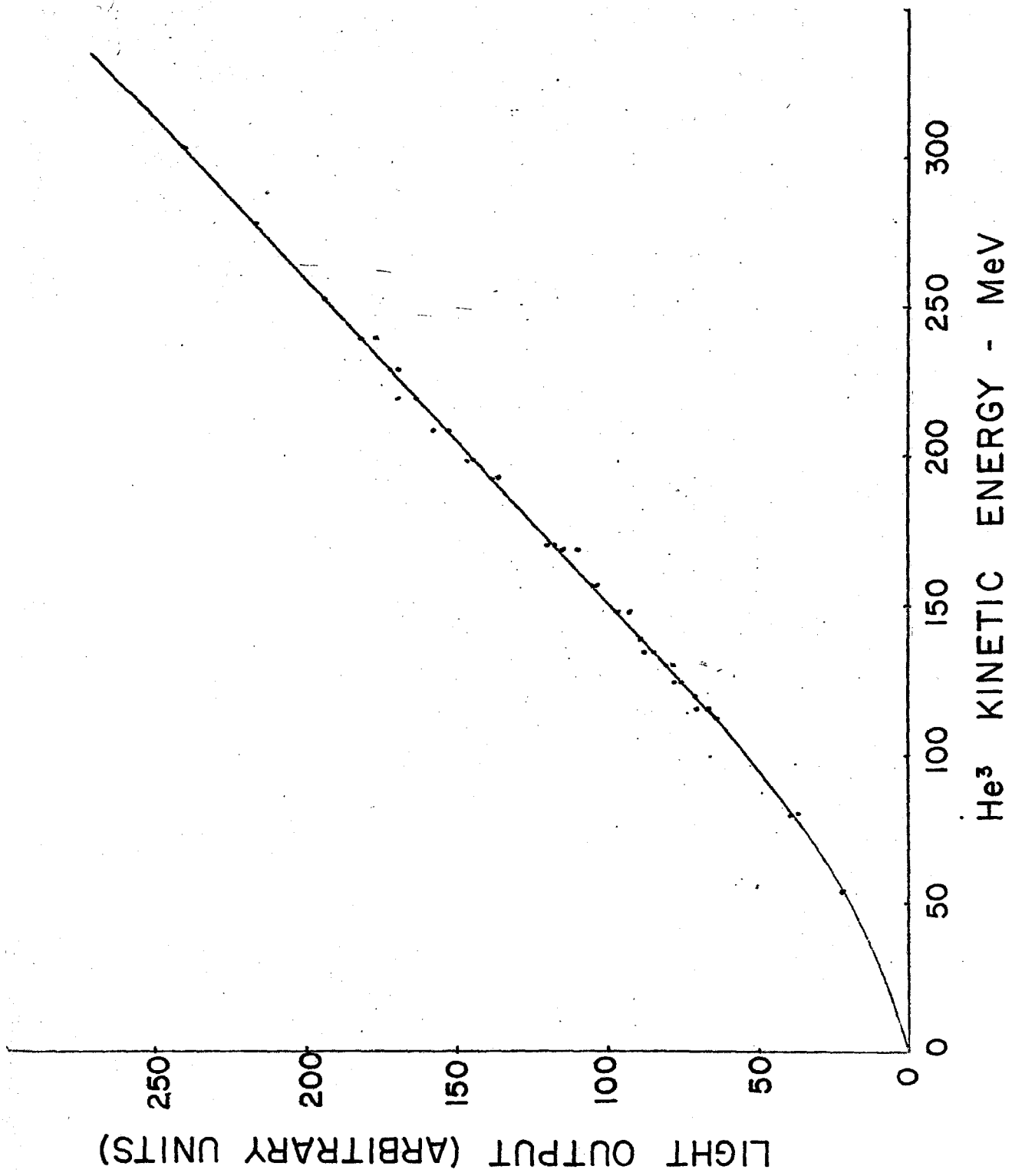

Figure 6.32 Light output versus kinetic energy.

6. He^3 Break-up

Some of the He^3's break up in the material preceding the detector, either as $He^3 \rightarrow p+d$, or as $He^3 \rightarrow p+p+n$. In either case, these would be vetoed in general by the differential pulse height counter in those runs where it was used. In runs where it was not, the break up would not in general produce a sufficient pulse height to simulate a He^3. Thus these particles are not detected, and some account must be made for the magnitude of the loss.

A fit was made to the He^3 detector inefficiency versus range in CH over the He^3 kinetic energy region 60-260 MeV. Using this fit, the data could be extrapolated to the amount of material the He^3 encountered enroute to the detector.

With the differential pulse height counter in place, the amount of material is equivalent to 8.21 MeV of CH. Without the counter, the figure is 4.4 mm of CH. This corresponds to break up losses of $(2.9 \pm 8)\%$ and $(1.6 \pm .5)\%$ respectively.

Some argument can be made for these losses being independent of the kinetic energy of the He^3, in the energy region of interest. This was taken to be the case for this experiment.

G. Helium Chamber Local Coordinates

The following summarizes briefly the procedure for construction of local coordinates, i.e., relative to the chamber frame of reference, in the helium chambers. Each of the two sets of helium chambers (see Fig. 2.1).

Assumptions (refer to Fig. 6.33):

A. A Z-axis perpendicular to the plane of the chamber is assumed.

B. Each plane is defined by a set of coordinates, one on the finish wire, one on the start wire, and a line connecting these two points is perpendicular to the wires composing the plane.

C. Scalar counts are supplied from the start wire to the finish wire, and from the start wire to the sparked wire, F and D respectively.

D. All planes have effectively the same Z.

F is the fiducial count. The equaption of the sparked wire is derived as follows (see Fig. 6.33):

$$X_I = X_S + D/F\ (X_F - X_S)$$

$$Y_I = Y_S + D/F\ (Y_F - Y_S).$$

The equation of the sparked wire is:

$$(Y - Y_I)/(X - X_I) = (X_F - X_S)/(Y_F - Y_S)$$

Inserting X_I, Y_I, this can be put into the form $A_i X + B_i Y + C_i$.

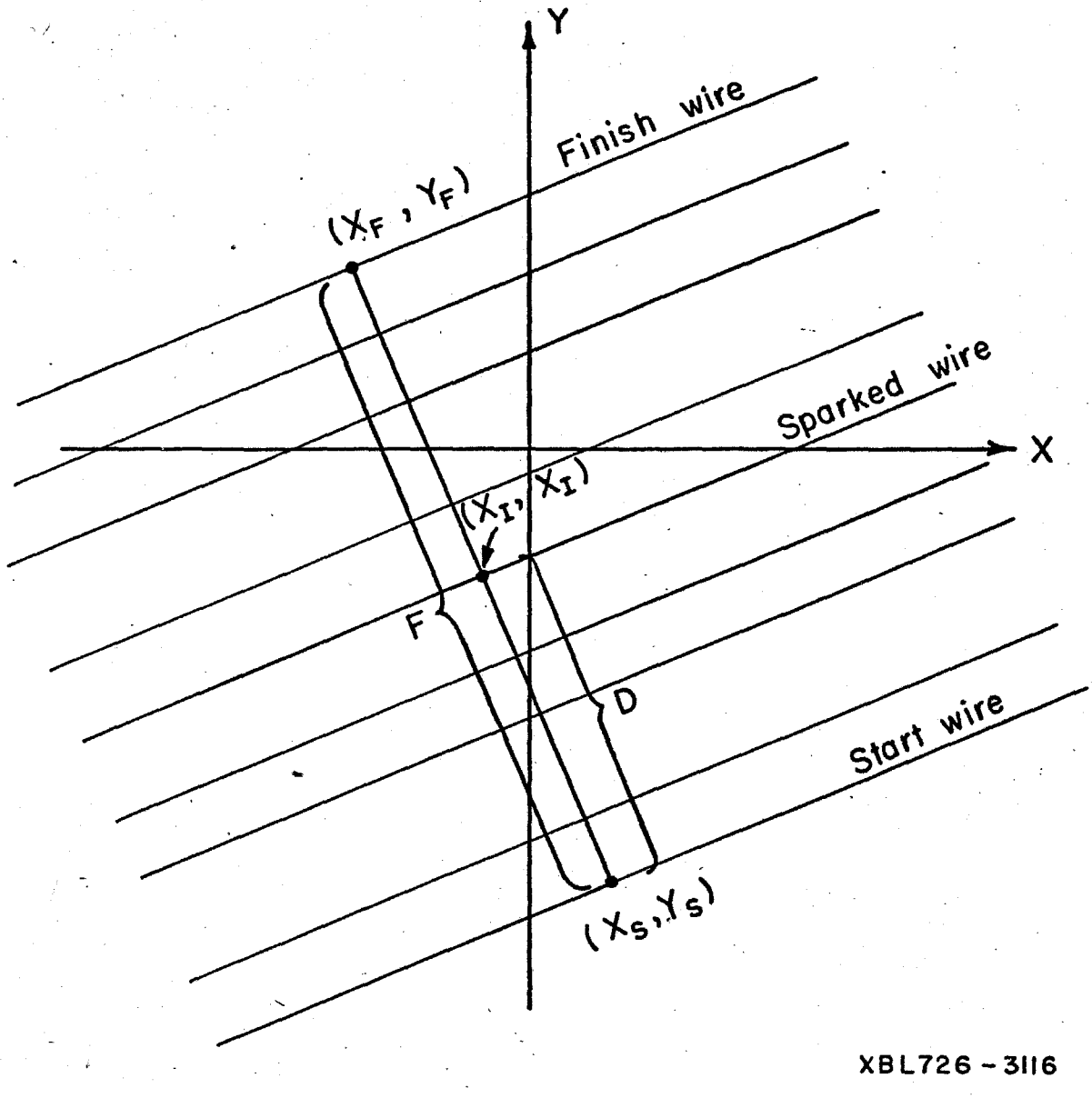

Figure 6.33 Definition of Wire Spark Chamber Coordinates

In the experiment, four planes were used for each chamber. The planes of wires were at angles of 0°, 60°, 90°, and 120°. We demand that at least three of the four planes have a sparked wire, and solve for the intersection of the sparked wires in a least-squares sense. This is defined as a local coordinate.

For the case of four sparked wires, we have a matrix equation of the form

$$M \vec{v} = \vec{c}$$

or

$$\begin{vmatrix} A_1 & B_1 \\ A_2 & B_2 \\ A_3 & B_3 \\ A_4 & B_4 \end{vmatrix} \begin{vmatrix} X \\ Y \end{vmatrix} = \begin{vmatrix} C_1 \\ C_2 \\ C_3 \\ C_4 \end{vmatrix}$$

This overconstrained system of equations is solved to give a best fit to X and Y, of the form $\vec{v} = M^{I} \vec{c}$. At the same time, the matrix $RSID = (MM^{I} - I)$ is computed, and used to compute the distances from a sparked wire to the coordinate via

$$\vec{r} = RSID \cdot \vec{c}$$

The largest component of $\vec{r}$ is reported as measure of the goodness of the coordinate determination.

Input data for this procedure includes a cutoff parameter. If the distance, $\vec{r}$, from any spark to a fitted coordinate is greater than the

fit parameter, that coordinate is eliminated from further consideration. One can also specify a parameter to resolve ambiguities should a common set of wires be involved in the formation of two or more different coordinates. The procedure searches for the best fit, defined as the coordinate with all wires being closer to the fitted coordinate than to any other coordinate.

Once a coordinate is found, the wires contributing to that coordinate are eliminated from further consideration. After all permissible fits have been found involving four wires, fits are sought containing three wires only. Finally, if no three or four wire fits are found, intersections of two wires will be used.

H. GEOKIN

The second stage of the analysis, GEOKIN (Geometry-Kinematics), performed two major functions:

1. Lab coordinates were constructed using chamber centered coordinates, survey information, and systematic properties of the beam. Calibrations involving positional dependence, and functions to transform pulse heights to energies were used to construct initial and final state particle energies.
2. With the energies and angles constructed as above, a kinematic least squares fitting routine was used to fit a set of energies and angles to an event hypothesis.

A schematic of the geometric configuration, indicating the construction of the angles used, is shown in Fig. 6.34 . Details of the various device calibrations can be found in the appendices.

The program flow of GEOKIN is shown in Fig.6.35. Data, output from the data summary program,were fetched from chip store. The program naturally divided into three segments:

1. Initialization.
2. Event processing.
3. Run summarizing.

Initialization consisted of fetching constants from the data cell, and from these constructing other constants useful for the event processing stage.

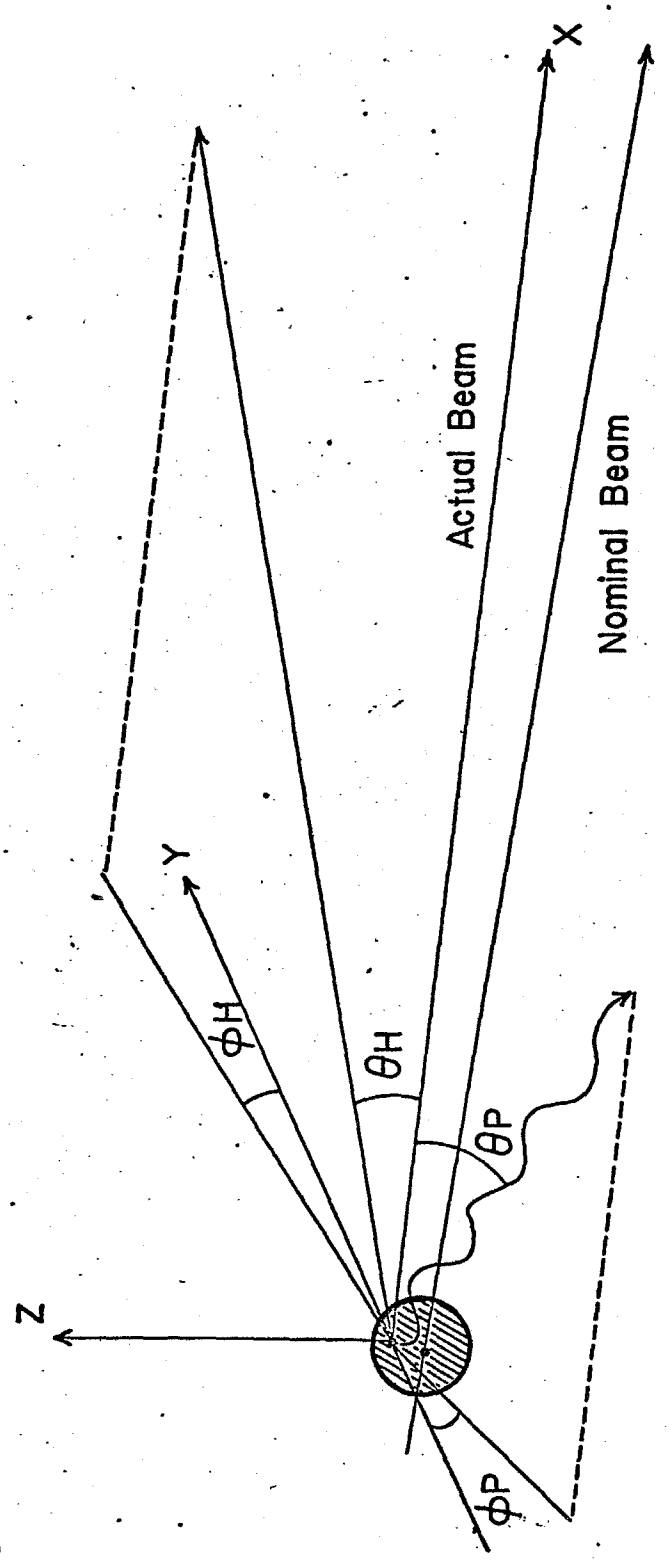

Figure 6.34 Definition of θ and ϕ Angles

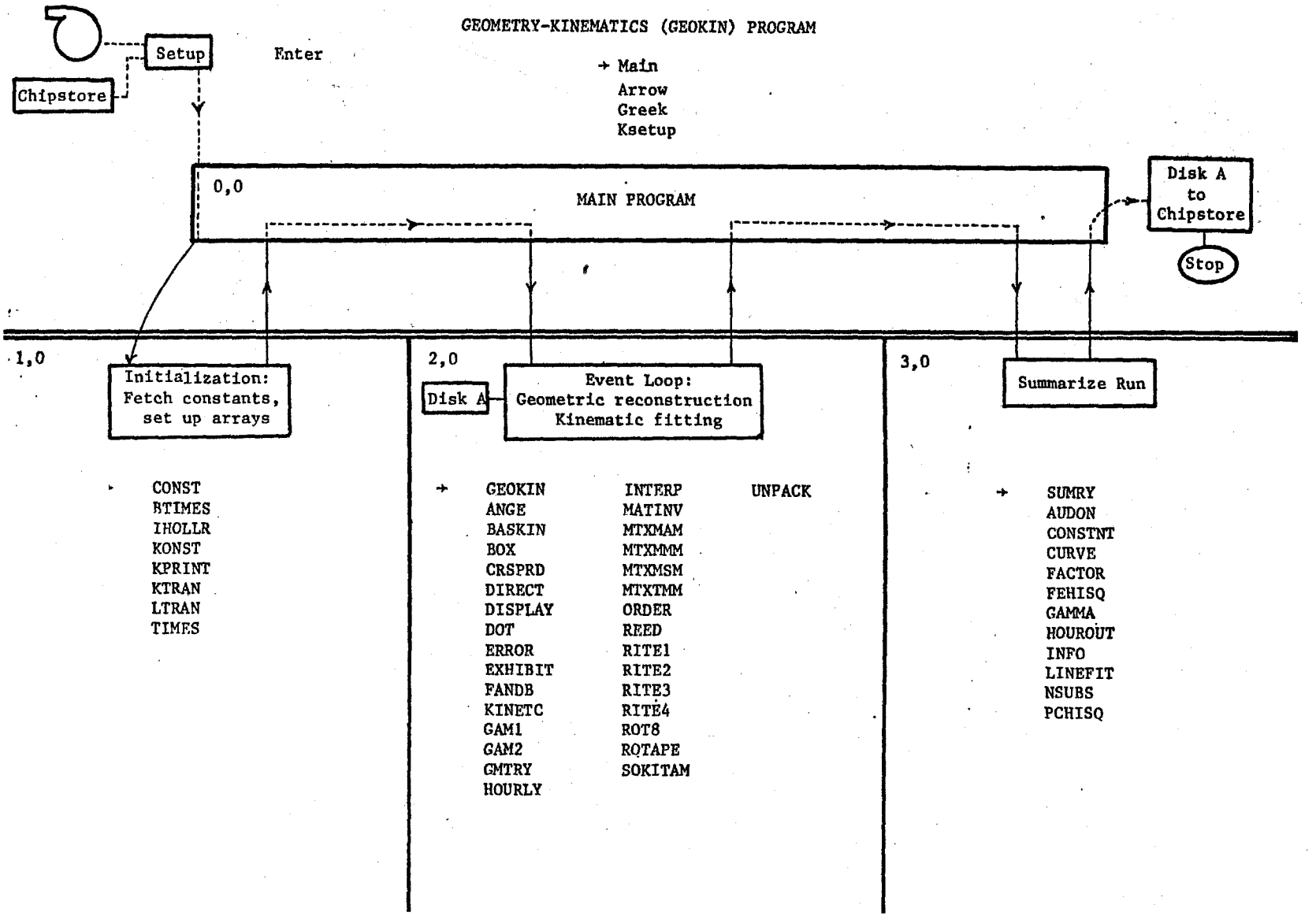

Figure 6.35 Logical Structure of the Program GEOKIN

For event processing the concept of a sub-event was introduced. In general, each chamber could have more than one coordinate. Thus each combination of coordinates had to be investigated separately as a possible event type. Prior to actually fitting the sub-event to an event hypothesis, various cuts could be imposed. Cuts might be placed on the:

1. differential pulse height counter output;
2. position of the event origin with respect to the target;
3. coplanarity;
4. position of the reconstructed helium angle relative to the reconstructed energy.

If a sub-event survived these cuts, the fitting procedure was applied, and information pertinent to the sub-event stored.

At the conclusion of a run, various statistics about the run were tabulated. Included were such things as the number of events not surviving the cuts, the number which could not be fit to the fitting hypothesis, the number of sub-events per trigger.

Finally, the resulting data was stored on chip store for subsequent processing by the cross section programs.

I. Data Summary Program Structure

Figure 6.36 is a highly schematic representation of the logical structure of the first phase of the analysis program. The program was constructed in this fashion in order to make use of the overlay capabilities of the computer used during the analysis, whereby a large program is broken into functional groups. Only the executive program and one of the function groups are stored in the computer at any time.

The executive program coordinated the execution of the functional groups, and in addition, initialized quantities needed for processing a run.

Event by event processing was done in functional group-A. The following sequence was performed for each event:

1. Read an event, and unpack its contents.
2. Form normalized wand scalar values, update fiducial values if necessary.
3. Form local coordinates in the helium counter chambers, vertices in the photon counter chambers (see separate appendices).
4. See whether this event can be used as a probe event for calculating spark chamber wand efficiencies.
5. Tabulate statistical quantities.
6. Pack the output, write on output medium.
7. If no more events are to be processed, return control to the executive program.
8. If no error limits have been exceeded, go to step 1, otherwise return control to the executive routine.

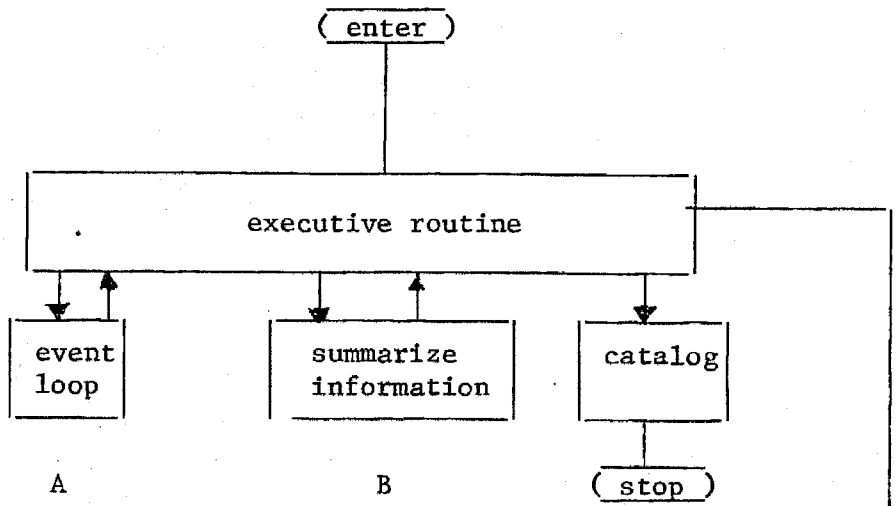

names of routines used	AEVENT	ASUMRE	CATALOG	ACQUIRE
	CHAMBR	BIN		ARROW
	DISPLA	CONSTNT		BUFEND
	DISPLAY	CURVE		DOT
	ELIMIN	FACTOR		GINV2
	FIDDLE	FETCH		HISTS
	FIT2	FCHISQ		HOURLY
	FIT34	GAMMA		SINV
	PACKIT	HISTOC		SET,AT
	PROBE	HOUROUT		
	READ1	INFO		
	SHOWER	LINEFIT		
		PCHISA		

Figure 6.36 Logical Structure of the Data Summary Program

Next the executive program turns control over to functional group-B. This group is composed primarily of binning and plotting routines for display of the statistical information accumulated during event by event processing. Finally, the executive program turns control over to functional group-C, which summarizes the outcome of the processing. It then directs the data processed to the appropriate medium, either magnetic tape or the photo-digital storage system.

J. Efficiency Program.

A program to generate two body events was written to perform three functions:

1. to compute the geometric acceptance of the apparatus;
2. to aid in performing the background subtraction;
3. to provide samples of events of various types.

Figure 6.37 illustrates the basic flow of the program. Input to the program includes counters sizes and distances from a pivot point, target size, coordinate and energy resolutions, particle masses, incident beam energy.

Two event types were available. The first was simple two body. The second assumed that one of the final state particles immediately decays into two photons, and that the photons are subsequently detected. The relative numbers of the two kinds of processes could be specified, and was used to investigate the problems involved in separating $pd \rightarrow He^3\gamma$ from $pd \rightarrow He^3\pi^o$, $\pi^o \rightarrow \gamma\gamma$.

Effects such as multiple scattering, conversion efficiencies of the photons in the converter material, energy loss of the He^3's were all included, as well as any known systematic effects.

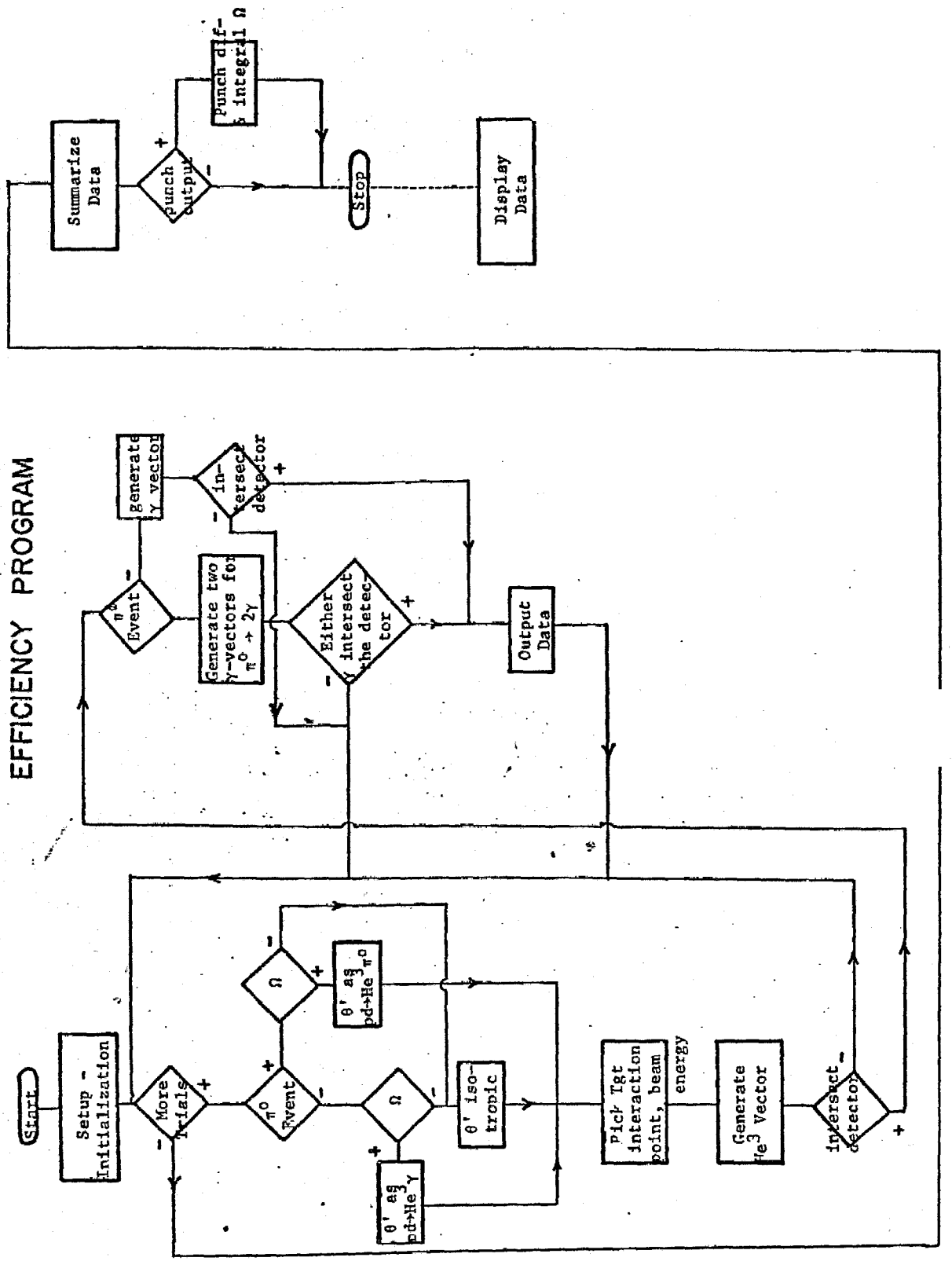

Figure 6.37 Logical Structure of the Efficiency Program

K. Chi-Square Fitting

The method of fitting used was that of least-square-fitting-with-constraints. Application of the technique as employed in this analysis had its genesis in bubble chamber work. Following is an outline of the method. For more details, several excellent references exist.[17,18,19]

The following definitions will be useful in the discussion that follows:

m = measured variable vector

G = inverse square error matrix form

$$G(i,j)^{-1} = \overline{\delta_{m(i)} \delta_{m(j)}}$$

x = fitted values of variables vector

f = constraint vector

B = constraint derivative matrix

$$B(i,j) = df_j / dx_i$$

α = vector of La Grange multipliers

A subscript 1 on a quantity implies the beam particle, 3 implies the particle went into the helium detector, 4 the photon detector. In the analysis m is a vector of dimension eight. The measured variables are the polar and azimuthal angles (see Fig.6.38), θ and ϕ, for the incident beam particle (proton), the helium particle, and the photon. The other two measured variables are beam energy and the helium energy. For this analysis the matrix G is assumed to be diagonal.

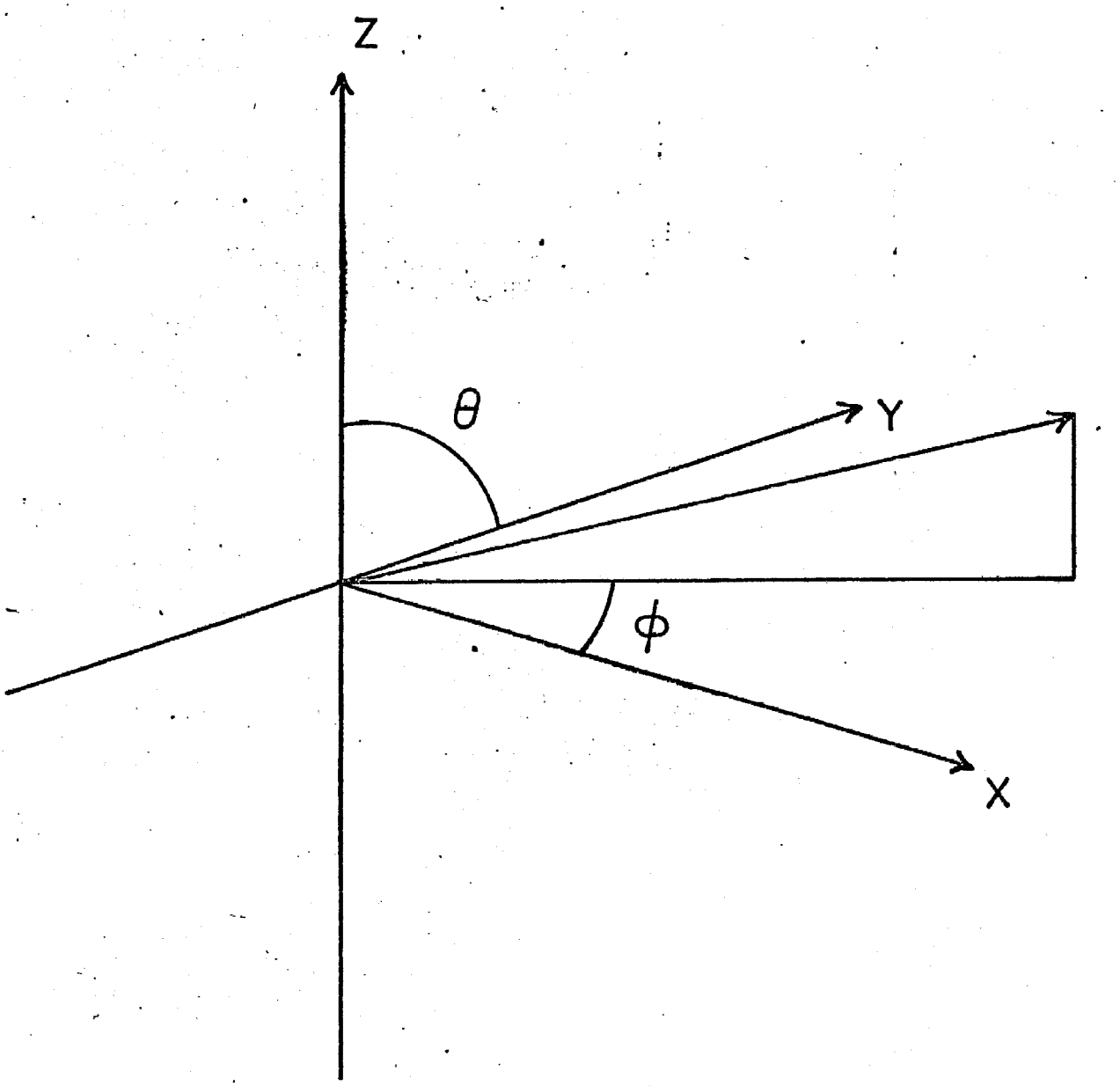

Figure 6.38 Definition of the Variables θ, ϕ

The constraint equations are those of momentum and energy. Each event is fit subject to the constraint that it satisfy energy and momentum conservation. Using the azimuthal and polar angles as defined above, the constraint equations are:

Momentum:

1) (x - component) $P_1 \sin\theta_1 \cos\Phi_1 - P_3 \sin\theta_3 \cos\Phi_3 - P_4 \sin\theta_4 \cos\Phi_4 = 0$

2) (y - component) $P_1 \sin\theta_1 \sin\Phi_1 + P_3 \sin\theta_3 \sin\Phi_3 + P_4 \sin\theta_4 \sin\Phi_4 = 0$

3) (z - component) $P_1 \cos\theta_1 + P_3 \cos\theta_3 + P_4 \cos\theta_4 = 0$

Energy:

4) $E_1 + M_2 = E_3 + E_4$

Equations 1, 3, and 4 were used as constraints, giving what is in bubble chamber parlance a 3-C fit. The remaining equation, 2, is used to determine the photon energy for the event.

The method of obtaining a fit and the associated measure of fit, chi-square, begins by defining the quantity

$\chi^2 = (\vec{x} - \vec{m})\, G\widetilde{(\vec{x} - \vec{m})}$, where $\widetilde{(\vec{x} - \vec{m})}$ means transpose.

This quantity is minimized, subject to the condition $\vec{F}(x) = 0$.

Introducing a LaGrange multiplier, $\vec{\alpha}$, define a quantity M given by:

$$M = 2\,\vec{f}\cdot\vec{\alpha} + \chi^2$$

The procedure now is to minimize the quantity M with respect to α and $\vec{x}$. We have, then,

5) $$\frac{dM}{d\alpha} = 2\,\vec{f} = 0$$

$$6)\quad \frac{dM}{dx} = B\vec{\alpha} + G\vec{x} = 0$$

The constraint equations, 5, are in general nonlinear, and the solution of equations 5 and 6 is in the general case quite difficult. The problem can be simplified somewhat if the constraints are sufficiently linear that an expansion of the constraints can be made. Consider a trial solution $\bar{x}$. To first order, the constraints become:

$$7)\quad f_i(x) = f_i(\bar{x}) + \frac{df_i}{dx_j}\,(\bar{x}_i - x_j) = 0 \qquad \text{or}$$

$$8)\quad f(x) = f(\bar{x}) + \tilde{B}(\bar{x} - x) = 0$$

The method is now to use an iterative procedure to find $\vec{x}$ and $\vec{\alpha}$. Using 6,

$$\vec{x} = -G^{-1}B\vec{\alpha}$$

Using 8:

$$\vec{f}(\bar{x}) = \tilde{B}(\bar{x} + G^{-1}B\vec{\alpha})$$

or

$$\vec{\alpha} = Q^{-1}[f(\bar{x}) - \tilde{B}\bar{x}], \text{ where } Q^{-1} = \tilde{B}G^{-1}B, \qquad \text{and}$$

$$\vec{x} = -G^{-1}B\vec{\alpha}$$

Using these values of $\vec{x}$, the next step is to see whether: $\vec{f} = 0$. In practice, one specifies a tolerance within which one says the constraints have been satisfied. If the constraint is satisfied, stop. If not, one uses the value of x as the new $\bar{x}$, and reiterates.

The actual routines for carrying out the method outlined above are embodied in the routines FANDB, and SOKIT2M. For reference, listings of these routines are given on the following pages.

```
      SUBROUTINE FANDB(F,B,X,NCON)
C-----------------------------------------------------------------------
C                    WRITTEN BY RVK          MAY 18, 1972
C-----------------------------------------------------------------------
      REAL M1, M2, M3, M4
      COMMON/MASS/ M1, M2, M3, M4
      DIMENSION F(3), B(8,3), X(8)
      COMMON/MASSQ/ S1, S2, S3, S4
      COMMON/EOBS/E3OBS,E4OBS
C-----------------------------------------------------------------------
C         SET UP QUANTITIES USEFUL FOR DERIVATIVE CALCULATIONS
C              ST = SINE OF A THETA ANGLE
C              SP = SINE OF A PHI ANGLE
C              1  = PROTON
C              3  = HELIUM
C              4  = PHOTON
C-----------------------------------------------------------------------
      ST3=SIN(X(1))
      CT3=COS(X(1))
      ST4=SIN(X(3))
      CT4=COS(X(3))
      ST1=SIN(X(5))
      CT1=COS(X(5))
      SP3=SIN(X(2))
      CP3=COS(X(2))
      SP4=SIN(X(4))
      CP4=COS(X(4))
      SP1=SIN(X(6))
      CP1=COS(X(6))
      P3=X(7)
      P1=X(8)
      E3=SQRT(P3**2+S3)
      E1=SQRT(P1**2+S1)
      Y=P1*ST1*CP1-P3*ST3*CP3
      Z=ST4*CP4
      P4=Y/Z
      E4=SQRT(P4**2+S4)
      E3OBS=E3 $ E4OBS=E4
      P4T1=P1*CT1*CP1/Z
      P4P1=-P1*ST1*SP1/Z
      P4T3=-P3*CT3*CP3/Z
      P4P3=P3*ST3*SP3/Z
      P4T4=-Y*CT4*CP4/Z/Z
      P4P4=Y*ST4*SP4/Z/Z
      P4PP3=-ST3*CP3/Z
      P4PP1=ST1*CP1/Z
C-----------------------------------------------------------------------
C                  CALCULATE THE COMPONENTS OF THE CONSTRAINT VECTOR F.
C-----------------------------------------------------------------------
      F(1)=P1*CT1+P3*CT3+P4*CT4
      F(2)=P1*ST1*SP1+P3*ST3*SP3+P4*ST4*SP4
      F(3)=E1+M2-E3-E4
C-----------------------------------------------------------------------
C         CALCULATE THE COMPONENTS OF THE DERIVATIVE MATRIX, B
C-----------------------------------------------------------------------
      B(1,1)=-P3*ST3+CT4*P4T3
      B(2,1)=CT4*P4P3
      B(3,1)=-P4*ST4+CT4*P4T4
      B(4,1)=CT4*P4P4
      B(5,1)=-P1*ST1+CT4*P4T1
      B(6,1)=CT4*P4P1
```

```
      B(7,1)=CT3+CT4*P4PP3
      B(8,1)=CT1+CT4*P4PP1
C-----------------------------------------------------------------------
      B(1,2)=P3*CT3*SP3   +   ST4*SP4*P4T3
      B(2,2)=P3*ST3*CP3   +   ST4*SP4*P4P3
      B(3,2)=P4*CT4*SP4   +   ST4*SP4*P4T4
      B(4,2)=P4*ST4*CP4   +   ST4*SP4*P4P4
      B(5,2)=P1*CT1*SP1   +   ST4*SP4*P4T1
      B(6,2)=P1*ST1*CP1   +   ST4*SP4*P4P1
      B(7,2)=ST3*SP3      +   ST4*SP4*P4PP3
      B(8,2)=ST1*SP1+ST4*SP4*P4PP1
C-----------------------------------------------------------------------
      PE4=P4/E4
      B(1,3)=-PE4*P4T3
      B(2,3)=-PE4*P4P3
      B(3,3)=-PE4*P4T4
      B(4,3)=-PE4*P4P4
      B(5,3)=-PE4*P4T1
      B(6,3)=-PE4*P4P1
      B(7,3)=-PE4*P4PP3-P3/E3
      B(8,3)=-PE4*P4PP1+P1/E1
C-----------------------------------------------------------------------
      RETURN
      END
      SUBROUTINE KINETC(ENOM)
      REAL M1, M2, M3, M4
      COMMON/KNC/A, D, P, E3C, P3C, E4C, P4C, P1, EINCM2, C
      COMMON/MASS/ M1, M2, M3, M4
      E1=ENOM+M1
      S=SQRT(M1*M1+M2*M2+2.*M2*E1)
      W=E1+M2
      P1=SQRT(E1*E1-M1*M1)
      GAM=W/S
      BETA=P1/W
      E3=(S*S+M3*M3-M4*M4)/S/2.
      E4=S-E3
      P=SQRT(E3*E3-M3*M3)
      A=GAM*P
      C=BETA*GAM*E3
      D=BETA*GAM*E4
      P3C=SQRT(E3*E3-M3*M3)
      P4C=SQRT(E4*E4-M4*M4)
      E3C=GAM*E3
      E4C=GAM*E4
      P3C=BETA*GAM*P3C
      P4C=GAM*BETA*P4C
      EINCM2=ENOM+M1+M2
      RETURN
      END
```

```
      SUBROUTINE SOKIT2M
C
C
C-----------------------------------------------------------------------
C     KINEMATIC LEAST SQUARES FITTING ROUTINE WRITTEN BY BRYCE SCHROCK,
C     OCTOBER, 1971 AT LRL, BERKELEY.  THE ROUTINE MINIMIZES CHI-SQUARED
C     SUBJECT TO THE NON-LINEAR CONSTRAINTS OF MOMENTUM-ENERGY CONSERVATION.
C
C
C          NVAR       = NUMBER OF MEASURED VARIABLES
C          NCON       = NUMBER OF CONSTRAINING EQUATIONS
C          VM(I)      = VECTOR OF MEASURED VARIABLES(INPUT)
C          VX(I)      = VECTOR OF FITTED VARIABLES(OUTPUT)
C          G(I,I)     = DIAGONAL WEIGHT MATRIX( G(I,I) = 1/SIGMA(I,I)**2)
C          GI(I,I)    = DIAGONAL ERROR MATRIX ( GI(I,I) = SIGMA(I,I)**2 )
C-----------------------------------------------------------------------
C
C
C-----------------------------------------------------------------------
      COMMON/FITBAG/   CHI2,IFRJCT,NVAR,NCON,VM(8),VX(8),GI(8,8)
      DIMENSION G(8,8),VXBAR(8),VC(8),SIGTST(8),VCBAR(8),VCDIF(8),F(3),
     .B(8,3),BDUM(8,8),VR(3),H(3,3),HI(3,3),VALF(3)
      DATA EPS1,EPS2  /.01,.01/
      DATA ISTPMX, ICUTSEC, ICUTOT/ 50, 25, 25 /
C-----------------------------------------------------------------------
C
C-----------------------------------------------------------------------
C     INITIALIZE PARAMETERS
C-----------------------------------------------------------------------
      IFRJCT = 0
      ISTP = 0    $ ICUTS = 0    $ ICUTO = 0
      OMEGA = 1.E6    $ CHISQA = 0.    $ CHISQB = 0.
      CHISQBO = 0.    $ CHI2 = 1.E6
C-----------------------------------------------------------------------
C     SET VXBAR,VCBAR FOR FIRST STEP AND CALCULATE THE WEIGHT MATRIX G
C     ALSO CALCULATE THE CONSTRAINTS AND DERIVATIVES FOR THE FIRST STEP.
C     THE SIGTST(I) ARE THE CONVERGENCE CRITERIA FOR THE DIFFERENCE VECTOR.
C-----------------------------------------------------------------------
      DO 200  I = 1,NVAR
      VXBAR(I) = VM(I)
      VCBAR(I) = 0.
      SIGTST(I) = EPS1*SQRT(GI(I,I))
  200 G(I,I) = 1./GI(I,I)
      CALL FANDB(F,B,VXBAR,NCON)
      GO TO 710
C-----------------------------------------------------------------------
C     FOR FIRST ITERATION, GO IMMEDIATELY TO 710 AND TAKE A STEP.
C     FOR SUBSEQUENT ITERATIONS, CALCULATE CONSTRAINTS AND DERIVATIVES
C     USING VX FROM THE LAST STEP.  IF NO STEP HAD BEEN TAKEN BEFORE LAST
C     STEP, CALCULATE THE ABSOLUTE VALUE OF THE CONSTRAINTS AND GO TAKE
C     STEP.  IF A PREVIOUS STEP HAD BEEN TAKEN, CALCULATE THE ABSOLUTE VALUE
C     OF THE CONSTRAINTS FOR THE LAST STEP AND CHECK IF THE CONSTRAINTS ARE
C     SATISFIED.  (A) IF THEY ARE, CHECK THE CHANGE IN THE DIFFERENCE VE
C     IF IT HAS STOPPED CHANGING, THE FITTING IS ALL DONE(GO TO 4000).
C     IF IT IS STILL CHANGING, TAKE ANOTHER STEP.  (B) IF THE CONSTRAINT
C     ARE NOT YET SATISFIED, COMPARE THE ABSOLUTE VALUE FROM THE LAST STEP
C     THAT FROM THE PREVIOUS STEP.  IF IT HAS IMPROVED, GO REDEFINE VXBAR
C     AND VCBAR AND TAKE ANOTHER STEP.  IF IT HAS NOT IMPROVED, CUT THE
C     SIZE AND TRY AGAIN.
```

```
C-----------------------------------------------------------------
  300 CALL FANDB(F,B,VX,NCON)
      OMEGOLD = OMEGA
      OMEGA = 0.
      DO 600  I = 1,NCON
  600 OMEGA = OMEGA + ABS(F(I))
      IF(ISTP.LT.2)  GO TO 700
C-----------------------------------------------------------------
  640 IF(OMEGA.GT.FPS2)  GO TO 660
      DO 650  I = 1,NVAR
      VCDIF(I) = ABS(VC(I)-VCBAR(I))
      IF(VCDIF(I).GT.SIGTST(I))  GO TO 700
  650 CONTINUE
      GO TO 4000
C-----------------------------------------------------------------
  660 IF(OMEGA.LT.OMEGOLD)  GO TO 700
      IF(ICUTS.GT.ICUTSEC)  GO TO 2500
      IF(ICUTO.GT.ICUTOT)  GO TO 2700
      ICUTS = ICUTS + 1    $ ICUTO = ICUTO + 1
      DO 670  I = 1,NVAR
      VC(I) = (VC(I)+VCBAR(I))/2.
  670 VX(I) = VC(I) + VM(I)
      CHISQA = (CHISQA+2.*PSI+3.*CHISQAO)/4.
      PSI = (PSI+CHISQAO)/2.
      GO TO 300
C-----------------------------------------------------------------
  700 DO 705  I = 1,NVAR
      VXBAR(I) = VX(I)
  705 VCBAR(I) = VC(I)
      CHISQAO = CHISQA
C-----------------------------------------------------------------
  710 IF(ISTP.GT.ISTPMX)  GO TO 2000
      ICUTS = 0
C-----------------------------------------------------------------
C     CALCULATE  R = BT*CBAR - F
C-----------------------------------------------------------------
      CALL MTX TMM(NVAR,NCON,1,B,VCBAR,BDUM)
      CALL MTX MSM(NCON,1,BDUM,F,VR)
C-----------------------------------------------------------------
C     CALCULATE H AND THEN H INVERSE.
C-----------------------------------------------------------------
      CALL MTX MMM(NVAR,NVAR,NCON,GI,B,BDUM)
      CALL MTX TMM(NVAR,NCON,NCON,B,BDUM,H)
      DO 1 I=1, NCON
      DO 2 J=1, NCON
      HI(I,J)=H(I,J)
    2 CONTINUE
    1 CONTINUE
      CALL MATINV(HI, NCON, AAAA)
C-----------------------------------------------------------------
C     CALCULATE ALPHA.
C-----------------------------------------------------------------
      DO 730  I = 1,NCON
      VALF(I) = 0.
      DO 725  J = 1,NCON
  725 VALF(I) = VALF(I) - HI(I,J)*VR(J)
  730 CONTINUE
C-----------------------------------------------------------------
C     CALCULATE C AND X.
C-----------------------------------------------------------------
      CALL MTX MMM(NVAR,NVAR,NCON,GI,B,BDUM)
      CALL MTX MMM(NVAR,NCON,1,BDUM,VALF,VC)
```

```
      DO 740  I = 1,NVAR
  740 VC(I) = - VC(I)
      CALL MTX MAM(NVAR,1,VC,VM,VX)
C-----------------------------------------------------------------------
C     CALCULATE CHI-SQUARED AND CHECK FOR ROUND-OFF ERRORS.
C-----------------------------------------------------------------------
      CHISQA = 0.
      DO 750  I = 1,NCON
  750 CHISQA = CHISQA - VALF(I)*VR(I)
      CHISQB = 0.
      DO 760  I = 1,NVAR
  760 CHISQB = CHISQB + VC(I)*G(I,I)*VC(I)
C-----------------------------------------------------------------------
C     CALCULATE PSI, TO BE USED WHEN CUTTING STEP.
C-----------------------------------------------------------------------
      PSI = 0.
      DO 780  I = 1,NVAR
  780 PSI = PSI + VC(I)*G(I,I)*VCBAR(I)
C
C-----------------------------------------------------------------------
      ISTP = ISTP + 1
      GO TO 300
C-----------------------------------------------------------------------
C
C-----------------------------------------------------------------------
C     REJECTED EVENTS COME HERE.  KEEP TRACK OF THEM.
C        IFRJCT = 1   NO CONVERGENCE WITHIN THE ALLOWED NUMBER OF STEPS
C        IFRJCT = 2   STEP SIZE CUT THE MAXIMUM NUMBER OF TIMES WITH
C                     NO IMPROVEMENT NOTED.
C
C-----------------------------------------------------------------------
C
 2000 IFRJCT = 1    $ GO TO 5000
 2500 IFRJCT = 2    $ GO TO 5000
 2700 IFRJCT=2 $ GO TO 5000
C-----------------------------------------------------------------------
C     IF GET TO 4000, A SUCCESSFUL FIT HAS BEEN OBTAINED.
C-----------------------------------------------------------------------
 4000 CHI2 = CHISQA
      RETURN
 5000 CONTINUE
      RETURN    $ END
```

L. PI-Zero Analysis

Kinematically similar, data for the reaction

$$pd \rightarrow He^3\pi^o \qquad (1)$$

was perforce collected simultaneously with the reaction of primary interest,

$$pd \rightarrow He^3\gamma. \qquad (2)$$

Reaction 1, owing to the strong, rather than electromagnetic, origin is produced about 30 times more copiously than reaction 2, and constituted the dominant background process. The following considerations motivated the analysis of the data for reaction 1:

1. The angular distribution for this process was needed in order to perform a background subtraction for reaction 2.
2. Other data existed for scattered angles and energies for reaction 1,[32,33,34] however, until now no complete angular distribution was available.
3. Previous investigators[34] established the normalization of reaction 1 relative to that for pp elastic scattering by measuring both reactions in the same experiment. This enabled us to check the normalization of our data.

The threshold energy for multiple pion production is calculated using:

$$T_p = [(M_{He^3} + nM_{\pi^o})^2 - (M_p + M_d)^2] / 2M_d,$$

where T_p is the incident proton kinetic energy, n the number of pions. The threshold energy for single pion production if 198.7 MeV, 415.4 MeV for two pions, and 641.0 MeV for three pions. Three pion production lies outside of the kinematic range of interest for this

experiment. A separate analysis was performed to see whether $2\pi^o$ contamination of reactions 1 or 2 would be significant. The conclusion is that it contributes at a negligible level, for at least four reasons:

1. The production cross section is lower for $2\pi^o$ because of the smaller phase space.
2. The phase space for the resultant photons from the process $\pi^o \rightarrow \gamma\gamma$ is large. For our apparatus the geometric detection efficiency for these photons is small.
3. The maximum helium lab angle is about 7^o. This is less than the helium angle for reaction 1 in the kinematic region of interest.
4. The missing mass for two pion production allows for immediate rejection.

We will not consider two pion contamination further.

The analysis of reaction 1 was similar to that for reaction 2, differing substantially only in the following respects:

1. The photons produced by $\pi^o \rightarrow \gamma\gamma$ were used only in the trigger requirements, but not in the subsequent analysis.
2. A 1-c kinematic fit was made to the data using a $pd \rightarrow He^3\ \pi^o$ hypothesis.
3. The helium center of mass angle used to bin the data was computed using properties of the helium rather than the photon, as with reaction 1.
4. The helium detector determined the geometric acceptance of the apparatus, rather than the photon detector.

The data was analyzed using only the properties of the target, the proton beam, and the helium. Modifications were implemented in the least-squares-fitting programs to permit use of a one constraint fit (1-c). Overall energy balance provided the constraint. A χ^2 for the fit was produced and used to make cuts in the subsequent analysis.

Prior to the kinematic fitting phase of the analysis, cuts were imposed on the data. A cut was placed on the output of the differential pulse height counter, and on the event origin, as determined by extrapolating the helium trajector to the target midplane. Typical distributions, with the positions of conservatively placed cuts indicated, are shown in Figures 6.39 and 6.40. The first cut was very powerful, immediately yielding a reasonably uncontaminated sample of $pd \rightarrow He^3\pi^o$ events. The second cut substantially reduced the amount of analysis by eliminating early event combinations due to spurious spark chamber signals.

The helium center of mass angle was needed to facilitate cross section calculations. This was obtained in two ways, one using the helium angle, one the helium energy. Using the lab energy, the center mass angle of the helium particle is computed using:

$$\cos\theta'_{He} = (E_{He}/\gamma - E'_{He})/\beta p'_{He}$$

where primed quantities refer to center of mass quantities. Using the helium lab angle, the calculation of the center of mass angle is performed using:

$$\cos\theta'_{He} = \{AC \pm [A^2C^2 - (A^2+B^2)(C^2-B^2)]^{\frac{1}{2}}\}/(A^2+B^2)$$

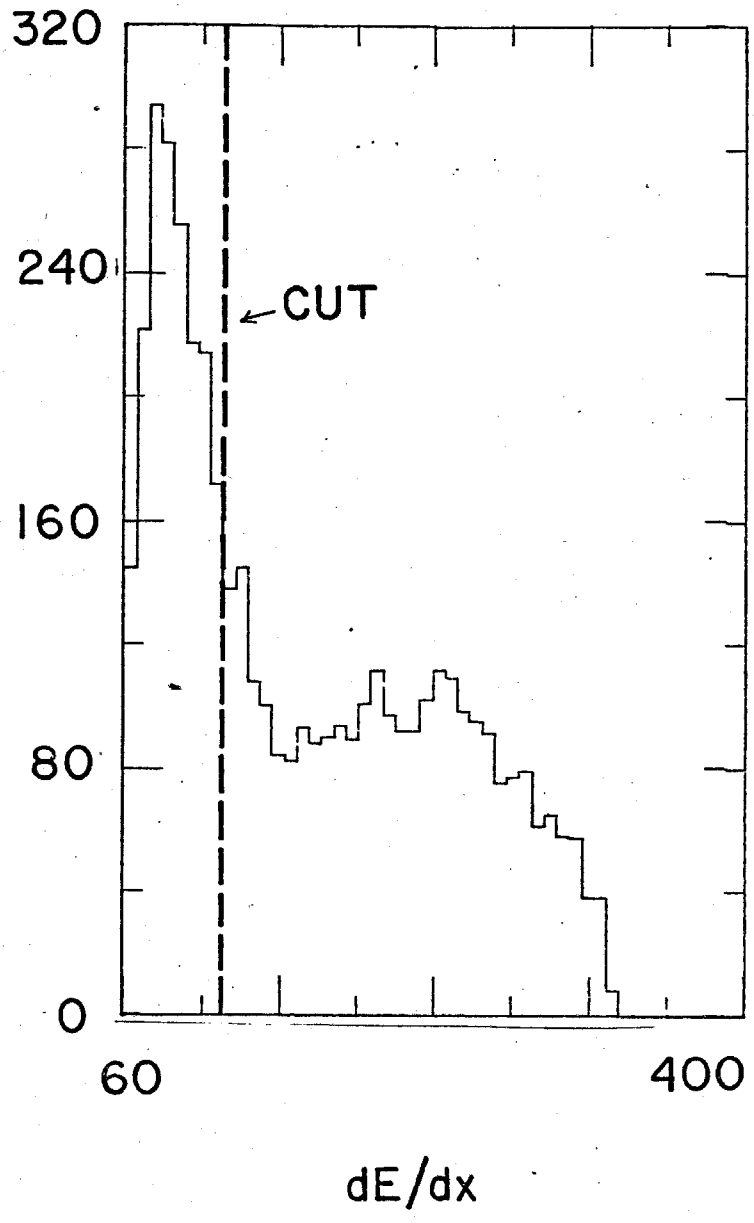

Figure 6.39 Differential Pulse Height Counter Spectrum

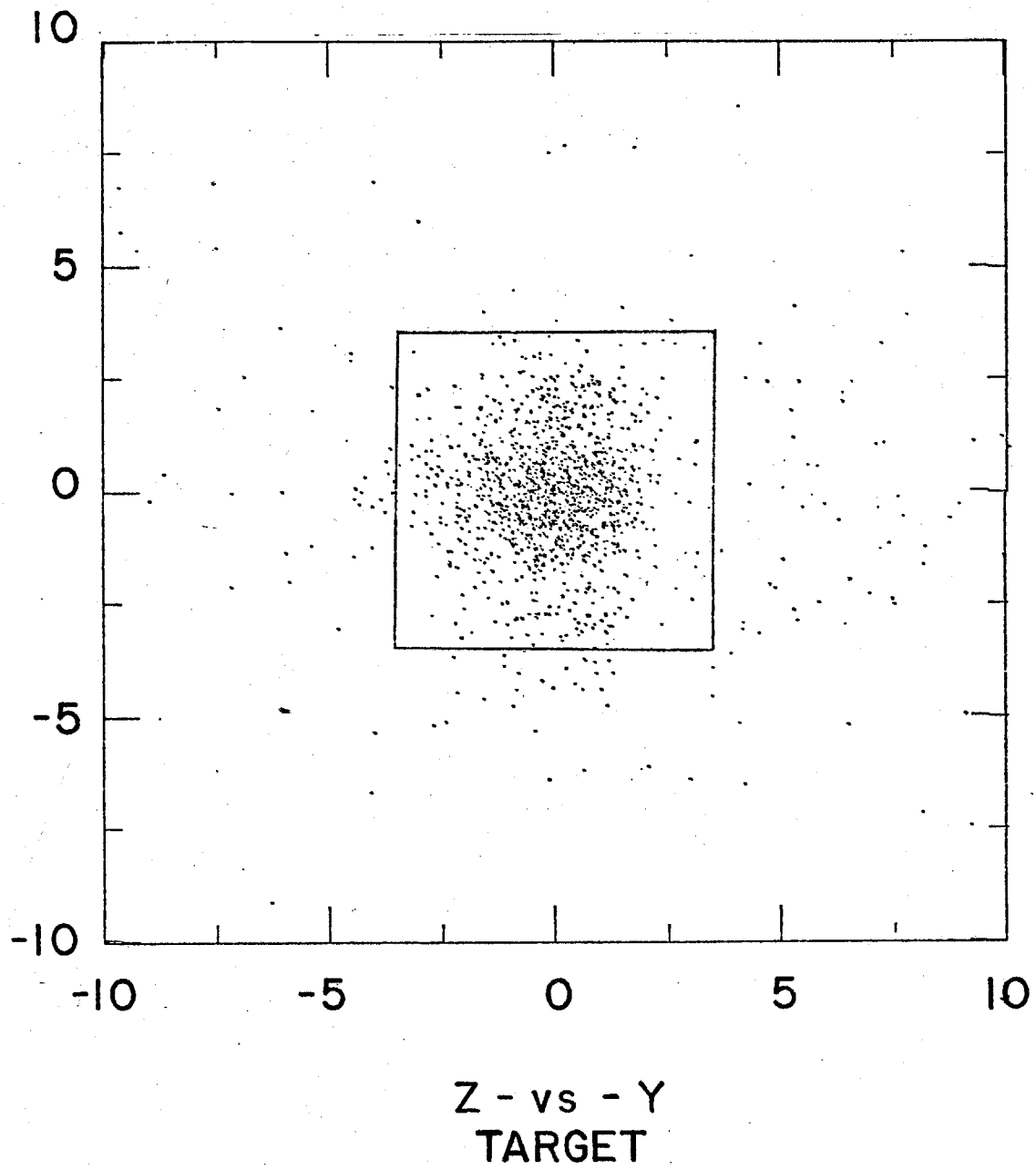

Figure 6.40 Reconstructed Event Origins

where

$$A = P'_{He} (1 + \beta^2 \gamma^2)$$

$$B = \gamma P'_{He} / \tan(\theta_{He\,L})$$

$$C \theta \beta\gamma^2 E'_{He}$$

The choice between the two roots is made by demanding that the lab helium energy calculated using the derived center of mass angle lie closest to the observed lab energy. The method yielding the best resolution was used, and depended on the particular lab angle or energy involved. Near the Jacobian peak of the lab angle versus center-of-mass angle plot the helium energy was used. Here the large value of $d\theta^*/d\theta$ made use of the angle unfeasible.

The geometric acceptance of the apparatus was computed using Monte-Carlo techniques (cf. section 4 and Appendix J). Independent checks of these calculations agreed on the percent level.

The remainder of the analysis proceeded as described in section 4 for reaction 1. Each photon detector setting encompassed a center of mass angle range of about 60°. Three counter settings were analyzed to yield a complete angular distribution for an incident proton energy of 462 MeV. In addition, more limited angular distributions were produced for incident proton energies of 377, 576 MeV. Figures 6.41 and 6.42 display the resulting angular distributions. Note in particular the agreement with Crewe, et al., suggesting that our overall normalization is consistent with pp elastic scattering data.

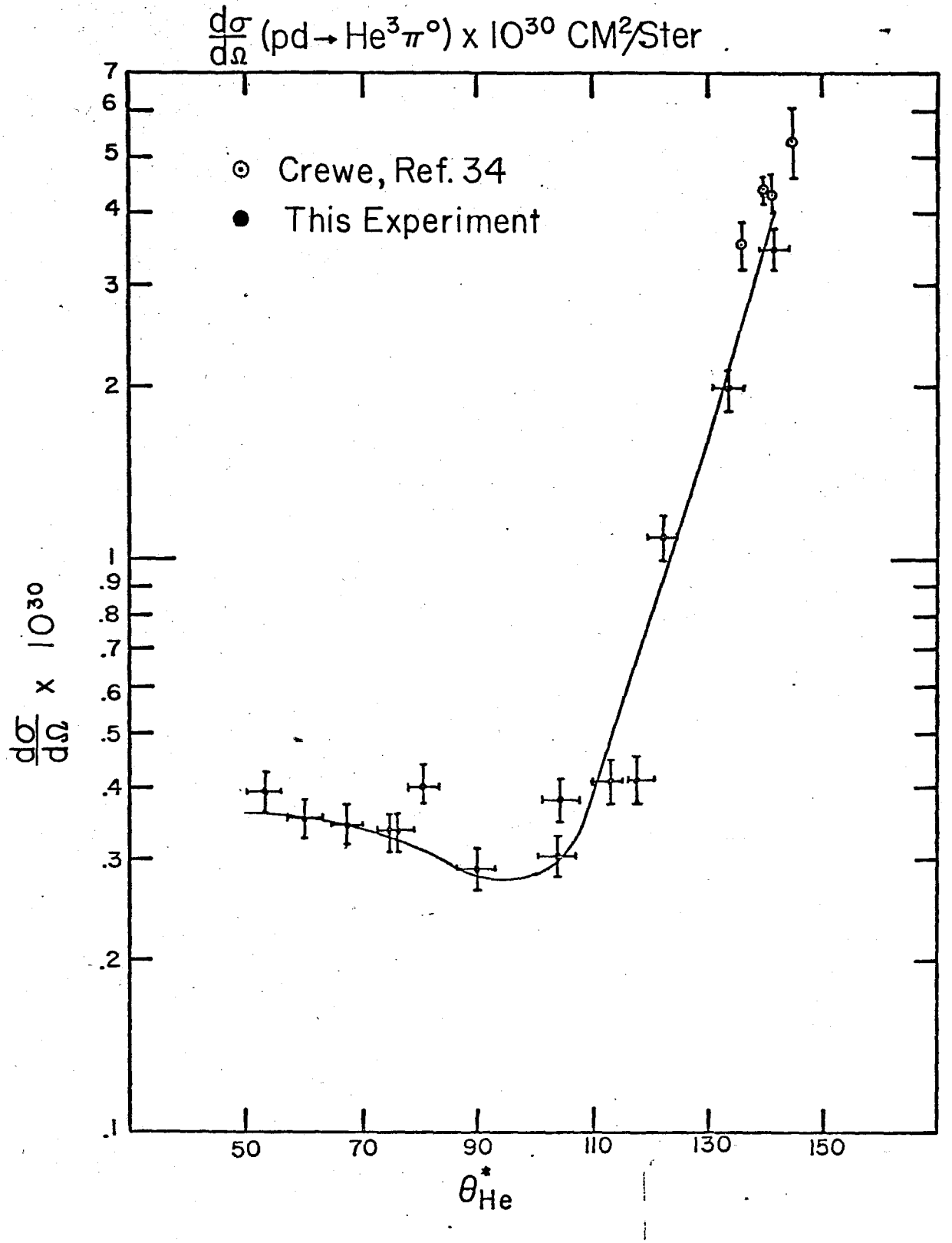

Figure 6.41 Differential Cross Section for pd → $He^3\pi^\circ$ at 462 MeV.

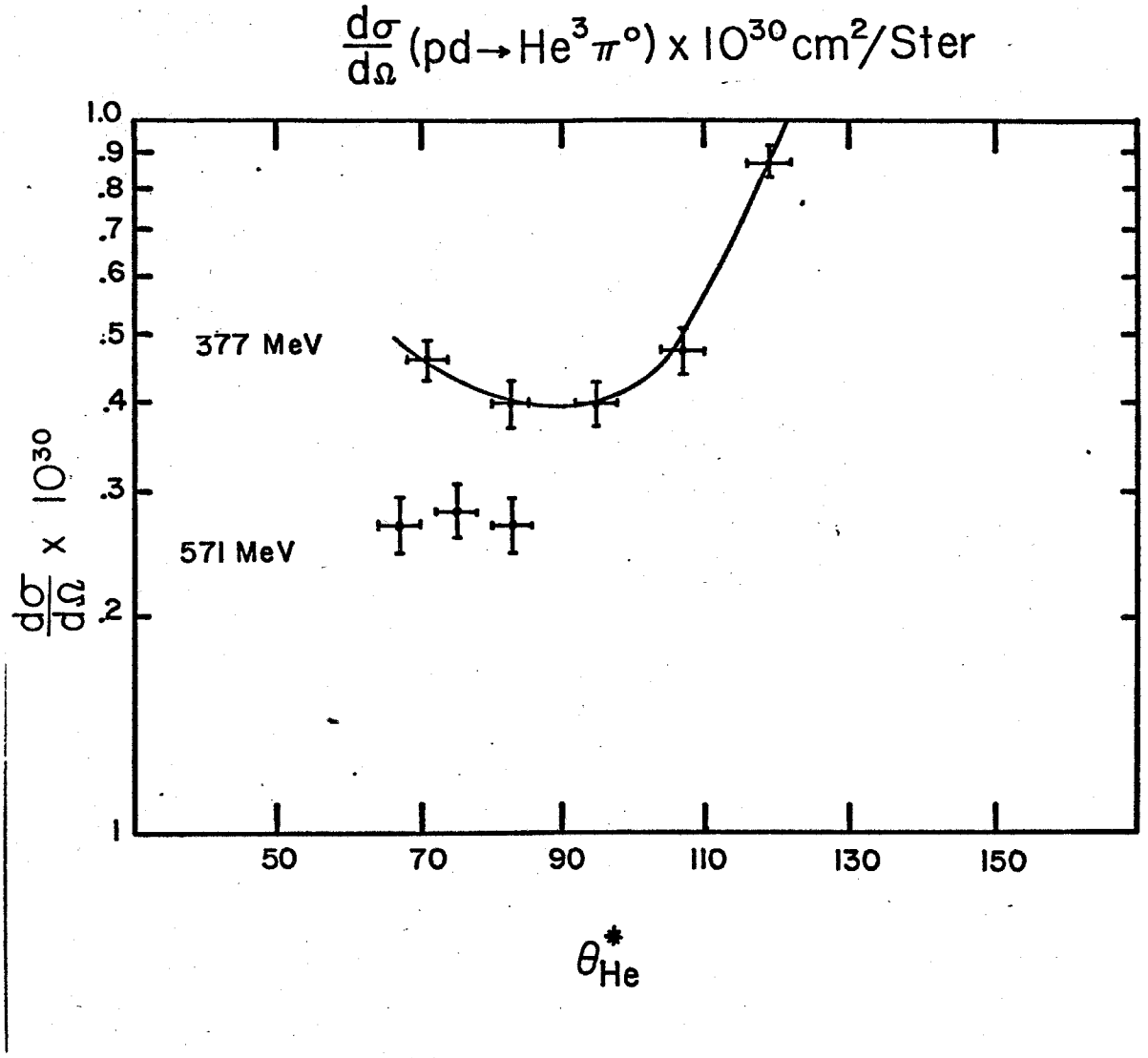

Figure 6.42 Differential Cross Section for pd $\rightarrow He^3\pi^o$ at 377 and 571 MeV.

BEAM ENERGY MEV	HELIUM CM ANGLE	dσ/dΩ
462	30.0	35.0 ± 2.8
462	40.0	35.0 ± 2.8
462	53.5	39.1 ± 3.2
462	60.5	35.1 ± 4.4
462	67.5	34.2 ± 2.5
462	74.5	33.3 ± 2.7
462	76.0	34.5 ± 1.9
462	80.0	32.0 ± 2.5
462	90.0	28.6 ± 2.9
462	104.5	30.5 ± 3.2
462	105.0	38.0 ± 3.8
462	113.5	40.5 ± 3.6
462	122.5	111.2 ± 7.8
462	131.5	197.5 ± 13.3
462	140.5	344.1 ± 27.0
377	80.0	41.0 ± 3.0
576	80.0	27.5 ± 2.7

TABLE 6.6 Angular distribution for pd → $He^3\pi^o$

The resulting angular distributions for the process $pd \rightarrow He^3\pi^o$ were used to perform a background subtraction. In order to do this a fit was made to the $pd \rightarrow He^3\pi^o$ angular distribution of the form

$$\frac{d\sigma}{d\Omega} = \sum_{i=1}^{6} a_i \theta'^{,i-1}$$

where θ' is the He^3 center-of-mass angle in radians. The coefficients obtained are:

$$a_1 = -58.30 \pm .83$$

$$a_2 = 497.09 \pm .62$$

$$a_3 = -1024.91 \pm .40$$

$$a_4 = 1029.36 \pm .23$$

$$a_5 = -501.00 \pm .13$$

$$a_6 = 93.67 \pm .07$$

M. Targets

Two thin liquid deuterium gas buffered targets were employed in this experiment. The nominal thicknesses were:

Thick target = .5000 ± .0005 inches

Thin target = .1710 ± .0002 inches

The thin target was employed for settings where the helium kinetic energy was low, and effects due to multiple scattering and ionization energy loss a potential problem.

Figure 6.43 illustrates schematically the target construction. The pressure inside the gas buffer and the liquid deuterium were the same, minimizing any tendency of the target to bow. The deuterium was condensed using liquid hydrogen. The 20 mil mylar window was required as a safety precaution should the flask break. The active area of the target was about three inches square.

The liquid level was monitored with a set of range telescopes positioned to measure pd elastic scattering (cf. Appendix B). The monitor rates for the thick target varied no more than 1% or so during the course of the experiment. Measurements made of the thickness using liquid nitrogen at the same pressure as encountered in actual running conditions indicated that bowing was negligible. The elasticity of mylar is small at room temperature, and indications are that it is not a strong function of temperature (checks were made of this). Thus making the bowing measurement at liquid nitrogen temperatures seems sufficient.

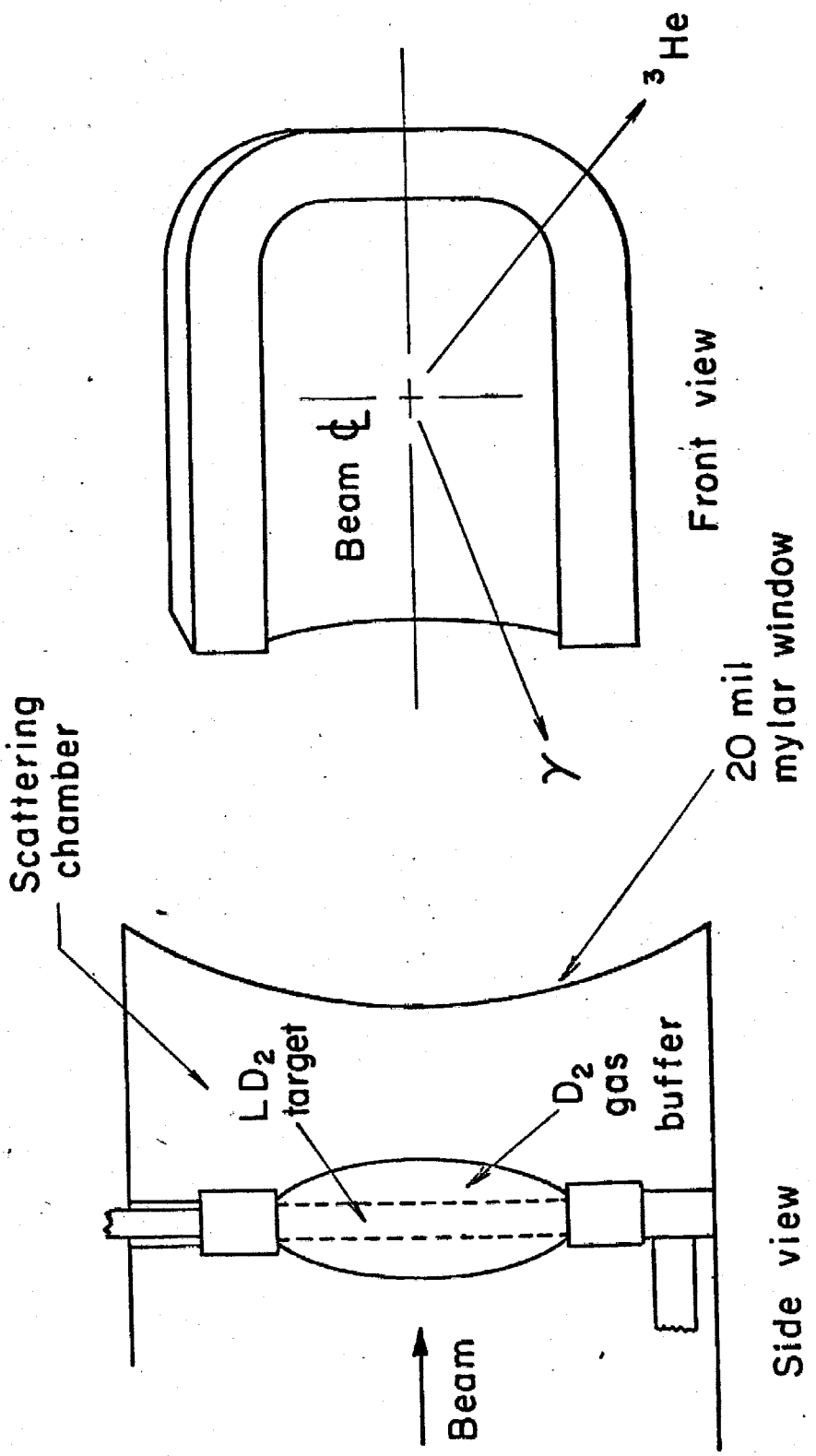

XBL737-3280

Figure 6.43 Target Construction Details

The monitors indicated as much as 25 - 30% variations for the thin target. The source of these variations is imperfectly known. The following points were checked or measured:

1. The thickness of the target was measured at liquid nitrogen temperatures. A bowing of about 25% was observed.
2. Scatterplots of the position of the event origin showed no indication of low liquid levels.
3. The target was watched at various times for indications of bubbling. Bubbling was observed for a period after the deuterium was condensed, after which it subsided.

The interpretation that has been made is that the thickness of the target increased about 25 - 30% due to bowing. Though we cannot prove that this is the direction of the change, the data obtained for those settings which overlap with the same setting using the thick target are consistent when this interpretation is made.

The pressure of the liquid deuterium was recorded as a possible additional monitor of the liquid density. The typical flask pressure was about 12 in. Hg, with a typical variation of ±1 in. Hg, although variations of 20% were observed. However, no correlations of this pressure variation with monitor rate was observed. Data[40] shows that the liquid density is not a strong function of pressure. We take the liquid density to be .16770 ± .00050 gm/cm^3.

N. Beam Integrators

Three helium filled ion chambers, each with its own integrator, were used to measure the beam intensity. The integrators were periodically calibrated using a current source (Keithly 201). The results of the three ion chambers were consistent to better than 1% over the entire duration of the experiment.

A set of direct beam counters, each 1/8" thick and 12" in diameter, were used in conjunction with the proton telescopes (cf. Appendix B) in order to determine the absolute ion chamber calibration. Briefly, the technique was to run the beam at a low intensity to establish a relationship between the beam intensity, as measured by the direct beam counters, and the coincidence rate for the proton telescopes for pp elastic scattering from a CH_2 target, using a 558 MeV proton beam. Removing the direct beam counters, the intensity of the beam was increased until the leakage current of the ion chambers was negligible compared to the beam current. Comparing this beam current to the coincidence rate for the proton telescopes yields the absolute calibration.

A low beam intensity of about 10^6 protons per second, instantaneous, was used with the direct beam counters. At this rate reliable corrections could be made for counting losses. The high beam intensity was about 2×10^8 protons per second.

The 558 MeV energy was chosen because the pp elastic scattering cross section is quite flat in this energy region. This made the measurement quite insensitive to any small changes in beam steering. The target for

pp elastic scattering consisted of a 4 inch block of CH_2, located downstream of the ion chamber being calibrated.

The largest correction to the measurement was for accidental coincidences in the proton telescopes. The rate due to accidental coincidences was typically 2%.

Per unit of integrator output, the value of the integrator constant obtained finally is $(2.84 \pm .05) \times 10^7$ protons.

0. Current Experimental Status of Symmetries

Here we briefly review the present experimental status of the symmetries C (charge conjugation), P (parity), T (time reversal), CP, and CPT in the weak and electromagnetic interactions. The symmetries C, T[26,40,41], P, and CPT[49] are all known to be invariant in the strong interactions (SI) with a precision of .3% or better, and will not be considered further as a possible area in which to look for symmetry violations. In particular, CPT is tested by measuring the mass of K°, $\bar{K}^\circ$[49], where $| \bar{K}^\circ > = CPT | K^\circ >$.

The equality of

$$< K^\circ | H_{SI} + H_{EMI} + H_{WI} | K^\circ > = < \bar{K}^\circ | H_{SI}+H_{EMI}+H_{WI} | \bar{K}^\circ>,$$

which calculates the mass of K°, $\bar{K}^\circ$ has been established to a precision of $\Delta_{m/m} \sim 10^{-14}$, where $\Delta_m = | m_{K^\circ} - m_{\bar{K}^\circ} |$, $m \sim m_{K^\circ}$.

In the electromagnetic interactions (EMI) an upper limit on CPT violations of about one part in 10^{12} can be established if one assumes that the contribution to any violation in the SI due to EMI has a strength on the order α[49]. Studies of EMI via interactions of leptons[59] places an upper limit on parity violations of one part in 10^8. Bernstein, Feinberg, and Lee[26] reviewed the experimental status of C and T conservation in the EMI, and found the evidence to be consistent with a rather large violation. Recent measurements, using the method of detailed balance, of the reactions $np \leftrightarrow \gamma d$ and $\pi^- p \leftrightarrow n\gamma$ claim results consistent with no violation . These experiments are very difficult, however, all suffering to varying degrees from

normalization difficulties. Thus, although one rules out a gross violation of the order of 30%, one cannot as yet rule out 5% violations. Tests of C-invariance using decays of B=0 particles and looking at the energy distributions of the charged final states are inconclusive at this time.

In the weak interactions (WI) it is well known that P is violated. In 1964[23] it was observed that the product CP is not conserved in weak decays of the kaon. Specifically, the KL, thought to be a CP eigerstate with eigenvalue - 1, was observed to decay into two pions (CP=1). Present values for the magnitude of the violation for the charged and neutral decay modes are 1.98×10^{-3} and 2.09×10^{-3} (ref. 60).

It is this CP violation, thus far observed only in the weak decays of kuons, which has motivated the search for a corresponding T violation.

Where should one look for the T-violation? One suggestion stems from the suggestive value of 2×10^{-3}, which is approximately α/π. If the decay of K_L into two pions were due to an electromagnetic correction to the weak decay Hamiltonian, then perhaps there might be a large T-violation in the electromagnetic interaction of hadrons. It is these notions which have lead to measurements of the processes $\pi^- p \leftrightarrow \gamma n$, $np \leftrightarrow \gamma n$, and finally to this experiment which measures $pd \leftrightarrow \gamma He^3$.

24. T. A. Lasinski, et al., RMP 45 ,part II (1973).

25. W. Pauli, Niels Bohr and the Development of Physics (McGraw-Hill Book Co., New York, 1955).

26. J. Bernstein et al., PR 139, B1650 (1965).

27. N. Christ and T. D. Lee, PR 143, 1310 (1965).

28. T. G. Inis, Constant-Amplitude Light-Flash Generator for Gain Stabilization of Photosensitive Systems, UCRL-10895, 1965 (Unpublished).

29. J. M. Hammersley and D. C. Handscomb, Monte Carlo Methods (Methner & Co. LTD, London, 1967).

30. G. D. Badhman, et al., NIM 57, 116 (1957).

31. R. L. Grawn and D. L. Smith, NIM 80, 239 (1970).

32. D. Harting, et al., PR 119, 1716 (1960).

33. N. L. Booth, PR 132, 2305 (1963).

34. A. V. Crewe, et al., PR 118, 1091 (1960).

35. J. McL. Emmerson, Symmetry Principles in Particle Physics (Oxford University Press, London, 1972).

36. P. Argan, et al., in: Few Particle Problems, I. Slaus, ed. (North Holland Press, 1972).

37. C. A. Heusch, et al., A Measurement of the Reaction $pd \rightarrow He^3\pi^o$ in the Resonance Region, submitted to the International Conference in Elementary Particles, Aix-en-Provence, Sept., 1973. UCSC Preprint 73/008 (1973), to be published.

38. G. C. Wick, Ann. Rev. Nuclear Science 8, 1 (1958).

39. C. E. Friedberg, Ph.D. thesis, Princeton, 1969 (Unpublished).

40. W. Von Witsch, et al., PL 22, 631 (1966).

58. The checks were made by comparing the results of a Monte Carlo program written by R. V. Kline with results from one written by Gary Olsen, a visiting summer student to LBL (1973) from UCLA. The latter program will appear as a UCRL report.

59. R. Trower, et al., High-Energy Particle Data, UCRL-2426, p121 (1965 Rev.).

60. S. S. Wilson, et al., NP B33, 253 (1971).

61. M. H. MacGregor, et al., PR 169, 1128 (1968); 173, 1272 (1965).

62. F. Boehm, et al., PRL 14, 312 (1965).

63. Ibid. Ref. 24.

64. D. H. Fredrickson, Ph.D. thesis, UC Berkeley, 1974 (Unpublished).

65. D. Bodansky, et al., PRL 17, 589 (1966).

66. S. Rock, Ph.D. thesis, UCRL-2004, 1971 (Unpublished).

67. O. C. Kistner, PRL 19, 872 (1967).

68. P. A. Bulgakov, et al., Yad. Fiz. 18, 12 (1973).

69. O. E. Overseth and R. F. Roth, PRL 19, 391 (1967).

70. B. A. Jacobson and E. M. Henley, PR 113, 234 (1959).

71. We note that the electromagnetic vertex γNN can yield an effect of the type discussed with respect to $\gamma N\Delta$ as long as the two nucleons are not on the mass shell, or equally far removed from the mass shell.

39. $n + p \rightarrow d + \gamma$: A Test of Time Reversal Invariance, Ph.D. Thesis, Princeton, 1969.

40. PL 22, 631 (1966).

41. PR 165, 1233 (1968).

42. L. Grodzins and F. Genovese, PR 121, 228 (1961).

43. D. Alburger, et al, Phil. Mag. 6, 171 (1961).

44. B. Aubert, et al, PL 10, 215 (1964).

45. S. Barshay, PRL 17, 49 (1966).

46. E. Whalin, et al, PR 101, 377 (1956).

47. J.C. Keck and A.V. Tollestrup, PR 101, 360 (1956).

48. D. Bartlett, et al, PRL 23, 893 (1969).

49. B. Schrock, et al, in High Energy Physics and Nuclear Structure, edited by S. Devons (Plenum Press, New York, 1970).

50. M. Schrock, et al, PRL 26, 1659 (1971).

51. D. Bartlett, et al, PRL 27, 881 (1971).

52. C. Richard-Serre, et al, Nuc. Phys. B20 (1970) 413-440.

53. P. Berardo, et al, PRL 26, 201 (1971).

54. C. Joseph, et al, Measurement of the π^- Radiative Capture Reaction in the First Resonance Region, Paper #22, Contributed to Bonn Conference, Aug. 1973.

55. W. Frazer, PR 150, 1244 (1966).

56. C.A. Heusch, et al, A Measure of the Reaction $\gamma He^3 \rightarrow pd$ in the Resonance Region, UCSC 73/004, Submitted to International Symposium on Electron and Photon Interactions at High Energies, Bonn, Aug., 1973.

57. See ref. 36, page 519 for some current (1972) results. The

experimental situation is reviewed by K.H. Bray, et al, PR C3, 1771 (1970).

58. The checks were made by comparing the results of a Monte Carlo program written by R.V. Kline with results from one written by Gary Olsen, a visiting summer student to LBL (1973) from G. Igo's group at UCLA. The latter program will appear as a UCRL report.

59. Trower, et al, High Energy Particle Data, UCRL-2426, Vol.I (1965 Rev.), page 121.

60. S.S. Wilson, et. al., Nuc. Phys. B33, p.253 (1971).

61. MacGregor, et al, PR 169, 1128 (1968); 173, 1272 (1965).

62. Boehm, et al, PRL 14, 312 (1965).

63. Rev. Mod.Phys., Vol. 45, No. 2, Part II, April, 1973.

64. D.H. Fredrickson, Ph.D. thesis, UC, Berkeley, 1973.

65. D. Bodansky, et. al., PRL, 17, 589(1966).

66. S. Rock, Ph.D. thesis, UCRL - 20041.

67. O.C. Kistner, PRL, 19, 872(1967).

68. Bulgakov, et. al., Yad. Fiz. 18, 12(1973).

69. Overseth, et. al., PRL, 19, 391(1967).

70. Calaprice, et. al., Phys. Rev. 184, 1117(1969).

71. Stein, et. al., PRL, 19, 741(1967).